Kinetics of Polymer Interfacial Reactions

Shuo Zhang

Submitted in partial fulfillment of the

requirements for the degree of

Doctor of Philosophy

in the Graduate School of Arts and Sciences

COLUMBIA UNIVERSITY

2013

ABSTRACT

Kinetics of Polymer Interfacial Reactions

Shuo Zhang

The reaction of a functional polymer at an interface has very broad applications in industry. Surface-bound polymers have been employed to control surface properties ranging from wettability and adhesion to friction and biocompatibility. More recently, the applications of functional polymer films in microelectronics, optical, nanocomposites, DNA microarrays, and enzyme immobilizations have drawn a lot of attention. There are a wide range of influencing factors associated with the kinetics of polymer interfacial reaction, and these challenges are especially prominent in the field of surface modification. In this thesis, different challenges were addressed to explore click reaction kinetics of end functional reactants (small molecules and polymers) reacting to self-assembled monolayers (SAMs) on solid substrates: first of all, functional surfaces modified with azide SAMs are presented in Chapter 3. Secondly, a precise control of the areal density of surface 'click' functionality is proposed in Chapter 4. Thirdly, a kinetic investigation of reaction between functional polymers and functionalized interface is described in Chapter 5.

In Chapter 3, the reactive surface of a Germanium substrate is prepared by a high-quality azide-functional SAM. These azide-functional substrates enable interfacial 'click' reactions with complementary alkyne-functional molecules to be studied *in situ* by attenuated total reflectance infrared spectroscopy (ATR-IR). To demonstrate their potential utility for kinetic studies, we show that, in the presence of copper (I) catalyst,

the azide-modified surfaces react rapidly and quantitatively with 5-chloro-pentyne to form triazoles via a 1,3-dipolar cycloaddition reaction. Time-resolved ATR-IR measurements indicate that the interfacial click reaction is initially first order in azide concentration, and then transitions to apparent second order dependence, when the surface azide and triazole concentrations become similar. The reaction achieves an ultimate conversion of 50% consistent with the limit expected due to steric hindrance of the 5-chloro-pentyne reactant at the surface.

In Chapter 4, two approaches are developed to control the 'click' functionality on the surface: a common approach by mixed monolayers constituting a fraction of the functional alkyne silanes and a fraction of chemically similar nonfunctional alkane silanes, and a new kinetic approach by tailoring surface azides through quenching S_N2 azide substitution reaction at a specific time

In Chapter 5, the ATR-IR technique is further manipulated to directly measure the kinetic trends of the reaction between azide functional monolayers modified on Germanium crystal surface and alkyne end-functional poly (n-butyl acrylate) (PnBA) and polystyrene (PS), via a copper-catalyzed 1,3-dipolar cycloaddition reaction. Time-resolved ATR-IR measurements distinguish four regimes rather than the two predicted by theory in the absence of segmental physisorption. The first two regimes correspond well to the theory. In the first regime, the rate is rapid and controlled by Brownian diffusion of polymer through the solvent, scaling with the square root of time. In the second regime, the rate slows considerately because of the energy barrier when the polymer chains have to penetrate a covalently bound polymer brush to reach the surface, and the rate is proportional to logarithm of time. There appear another two transition regimes before the

ultimate saturation, where the reaction rate reduces and then accelerates briefly. A possible explanation for this behavior is that the tethered polymer layer contracts lateral during the transition from “mushroom” to “brush” and thereby provides additional space for a few incoming polymer chains. A number of factors that influence the kinetics of the polymer interfacial reactions are examined including polymer nature, molecular weight and surface tension. Some general observations are summarized to show consistent kinetic behavior for different polymers with a wide range of molecular weights.

Table of Content

List of Figures and Schemes

Chapter 1

Chapter 2

Chapter 3

Chapter 4

Chapter 5

List of Tables

Chapter 1

Chapter 3

Chapter 4

Chapter 5

Acknowledgements

First I would like to thank my advisor, Prof. Jeffrey T. Koberstein. Thanks for his support and guidance through the years. I am grateful for his "hands-off" approach coupled with timely and insightful interventions that allowed me the creative freedom to find and develop my own way in research while keeping me on track. He has taught me many skills that will stand me in good stead for the future. I would also like to thank the members of committee Prof. Edward F. Leonard, Prof. Christopher James Durning, Prof. V. Faye McNeill and Prof. Ah-Hyung Alissa Park for serving on my Defense Committee.

I would like to thank everyone who helped out over the past 4.5 years. In particular, I would like to thank Dr. Liang Cao and Dr. Kai Luo to synthesize polymers for my work. I would also like to thank Yanir Maidenberg for very successful and dedicated collaboration. I would also like to thank Dr. Benjamin Dach for his help regarding MRSEC-related equipment. In additions, thanks to other members of my research groups including Dr. Nicholas Carbone, Dr. Hernan R. Rengifo and Dr. Sanjoy Samanta, and members of Prof. Nicholas Turro's group including Gabriella Sanguineti, Dr. Michael Kortrey, Dr. Ellane Park, Dr. Jeffrey Lancaster, Dr. Yi Rao, and Dr. Steffen Jockusch. I apologize if I missed any names.

Finally, I must mention the love of my family, especially the support of my mother Jiankun Hou, my farther Fuhai Zhang, my husband Shi Cheng, my mother-in-law Shuang Fan, my brother Yi Zhang and my sister-in-law Dan Liu.

Preface

The interfacial kinetic behaviors of functional polymers at surfaces and interfaces are extremely crucial to design smart polymer surfaces in a wide range of applications. In the following chapters, time-resolved ATR-IR measurements are used to monitor the quantitative kinetics of end-functional compounds reacting to SAMs at a solid substrate. In this preface, a summary of the results obtained from this work and some possible future directions are described.

This thesis is divided into 6 chapters. Chapter 1 concerns some fundamentals, presenting background information for this thesis. Chapter 2 discusses the techniques to characterize the polymer surfaces. In Chapter 3, a method to provide surface azide functionality is described. The method is based on exposing a UV-ozone-treated germanium ATR-IR plates to a solution of 11-bromoundecyltrichlorosilane at low temperature, followed by nucleophilic substitution of the terminal bromine by the addition of sodium azide. The resulting monolayer films are characterized by atomic force microscopy (AFM), contact angle analysis, X-ray photoelectron spectroscopy (XPS), attenuated total reflectance infrared spectroscopy (ATR-IR) and ellipsometry. XPS and ellipsometric thickness data correspond well to the results of molecular model calculations confirming the formation of a densely-packed azide-functional monolayer. These azide-functional substrates are used to react with complementary alkyne-functional molecules, and the reaction is studied *in situ* by ATR-IR. In the presence of copper (I) catalyst, the azide-modified surfaces react quickly and quantitatively with 5-chloro-pentyne to form triazoles via a 1,3-dipolar cycloaddition reaction. Time-resolved ATR-IR

measurements indicate a kinetic behavior: initially a first order dependence in azide concentration as expected from the reaction mechanism, with a rate constant of 0.034 min^{-1}, and then a second order dependence, with a rate constant of 0.017 $min^{-1}/(chains/nm^2)$, when the surface azide and triazole concentrations become similar, as predicted by Oyama *et al*. The ultimate conversion of the reaction (50%) is found to depend strongly on the absorbance area of the 5-chloro-pentyne reactant at the surface.

In Chapter 4, the surface 'click' functionality is controlled through two types of approaches. Firstly, a most traditional methodology is employed to expose a clean and activated solid surface to a solution comprising a portion of alkyne functional silane and a portion of alkane nonfunctional silane. The homogeneity of mixed SAMs is characterized by fluorescence microscopy by tethering an azide fluorescent dye to mixed SAMs. In addition, a new analytical tool, ATR-IR techniques, is described to detect preferential surface absorption. The IR method is based on the use of ATR-IR to monitor the click reactions between azide compounds with infrared "labels" and alkyne-functional SAMs deposited on germanium ATR plates. Secondly, a new kinetic methodology is developed by studying the kinetics of S_N2 azide substitution reaction of terminal bromine on Ge surface. The kinetics shows an initially high conversion at the beginning 2 minutes and transitions to a first order dependence on bromine concentration on the surfaces up to an ultimate conversion of almost 100%, with a rate constant of 0.0226 ± 0.0004 min^{-1}. Therefore, the surface composition can be tailored by terminating the reaction at a desired time. Also, the successful implementation of this approach is illustrated by homogeneity of mixed SAMs of azide groups and bromine groups measured by similar fluorescence techniques described in Chapter 4.1.

In Chapter 5, the ATR-IR technique is further demonstrated to be a direct and easy way to monitor the kinetics of reactions between mixed azide functional monolayers modified on Germanium crystal surface and alkyne end-functional polymers, via a copper-catalyzed 1,3-dipolar cycloaddition reaction. Time-resolved ATR-IR measurements reveal four-regimes of kinetic behavior. In the first regime, the reaction is controlled by Brownian diffusion of polymer through the solvent to the bare surface, and the reaction rate is rapid and proportional to the square root of time, as predicted from theory. In the second regime, the rate slows down considerately due to an energy barrier when the polymer chains have to penetrate a covalently bound polymer brush to arrive at the surface, and the rate scales with the logarithm of time. Another two interesting regimes appear before the saturation, where the reaction rate decreases slightly compared with that of the second regime, and then it accelerates briefly. Such behavior is not fully understood and can be ascribed to a transition from mushroom to saturated brush morphology that is accompanied by a reduction in the lateral chain dimensions. Some general comparisons are made between PnBA and PS with a variety of molecular weights, and they have shown uniform four-regimes of kinetic behavior. A number of factors that influence the kinetics of the polymer interfacial reaction are investigated including polymer nature, polymer surface tension and molecular weight. The ellipsometric results provide further evidence to justify the kinetic behavior. Atomic force microscopy (AFM) reveals that the topography of "mushroom" layers is rougher than that of "brush" layer.

To My Family

Chapter 1. Background

1.1 Self- assembled Monolayers (SAMs)

Functional self-assembled monolayers (SAMs) have become the material of choice to provide reactive functionality on inorganic surfaces and modify chemical and physical properties of metal, semiconductor, and insulator surfaces. The surface modification leads itself to a variety of applications such as microtribological lubrication,[1,2] metal corrosion barrier,[3-5] biosensor[6,7] and lithographical mask.[8-10] The molecules which comprise functional SAMs are short heterobifunctional molecules with a sticky foot on one end, selected to bond to the inorganic substrate, and a reactive functional group of interest on the other end. The two functional groups are joined by a spacer, typically a short chain hydrocarbon, to impart important interactions that drive the self-assembly process. SAMs are ordered molecular assemblies formed by the adsorption of an active surfactant on a solid surface (Figure 1.1). This simple process makes SAMs inherently manufacturable and thus technologically attractive for building super lattices and for surface engineering. The order in these two-dimensional systems is produced by a spontaneous chemical synthesis at the interface, as the system approaches equilibrium.

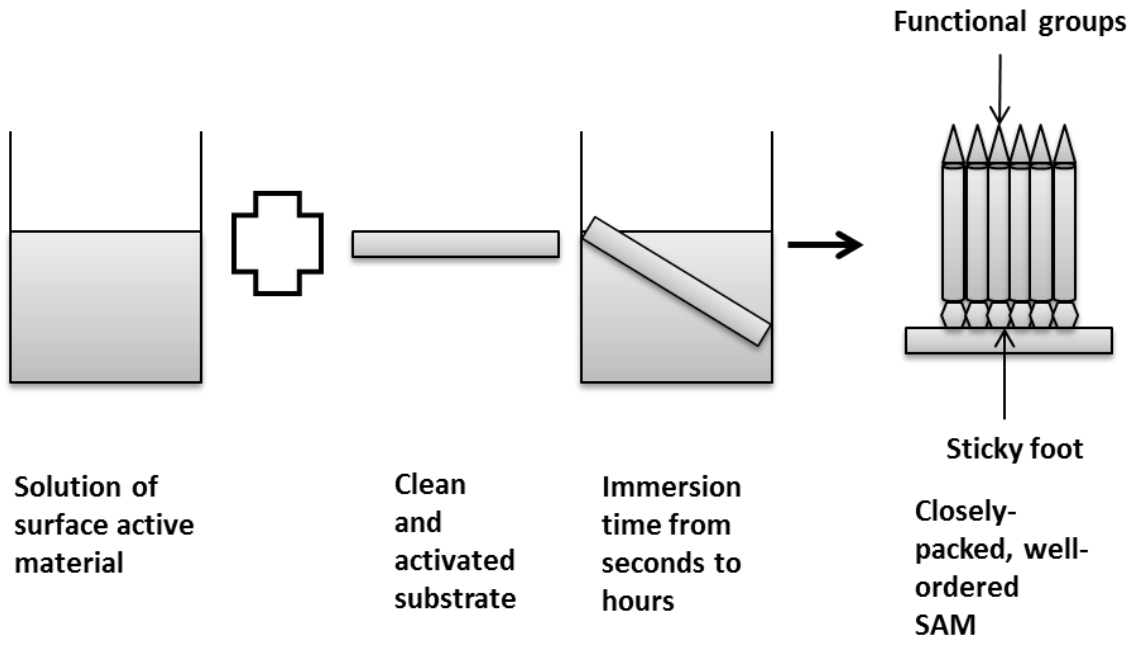

Figure 1.1. Self-assembled monolayers are formed by simply immersing a substrate into a solution of the surface-active material.

SAMs of silanes are commonly used in surface modification and have been successfully prepared on inorganic surfaces including silicon oxide,[11-15] aluminum oxide,[16,17] quartz,[18-20] glass,[11] mica,[21-23] zinc selenide,[11,16] germanium,[11] and gold.[24-26] This SAM requires hydroxylated surfaces and the driving force is the *in situ* formation of polysiloxane, which is connected to surface silanol groups (-SiOH) via Si-O-Si bonds. A number of factors that include the types of solvent, water content and temperature can influence to form high-quality SAMs of trichlorosilane, triethoxysilane and trimethoxysilane derivatives. They are not easily prepared, because of the need to carefully control the amount of water in solution and reaction temperature. For trichlorosilanes, it is suggested that a mixture of co-solvent should be used and one of which should be an n-alkane. This is done to adjust the chain length of the solvent to the

n-alkyl chain of the trichlorosilane. The other solvent of the co-solvent is carbon tetrachloride (anhydrous, <0.01% water), used to help in solubilizing the polar -$SiCl_3$ head groups and in avoiding the formation of micelles, which presumably are unable to react with the substrate.[27] While incomplete monolayers are formed in the absence of water,[12,15] excess water results in facile polymerization in solution and polysiloxane deposition of the surface.[18] Recently, McGovern *et al*. have suggested a moisture quantity of 0.15 mg/100 mL of solvent as the optimum condition for the formation of closely-packed monolayers.[28] Temperature has been found to play a vital role in monolayer formation. The transition temperature T_c below which an ordered monolayer is formed was found. This temperature T_c is an intrinsic property of the silane molecules: it depends on their chain length but is independent of the nature of the solvents used for the grafting reaction as shown in Figure 1.2.[27] As temperature decreases, the preference of physisorption of trichlorosilane to surface increases. In addition, as temperature decreases, reaction kinetics decrease as well, resulting in the diminution of thermal disorder in the forming monolayer, the formation of an ordered assembly, and the gain of van der Waals (VDW) energy.

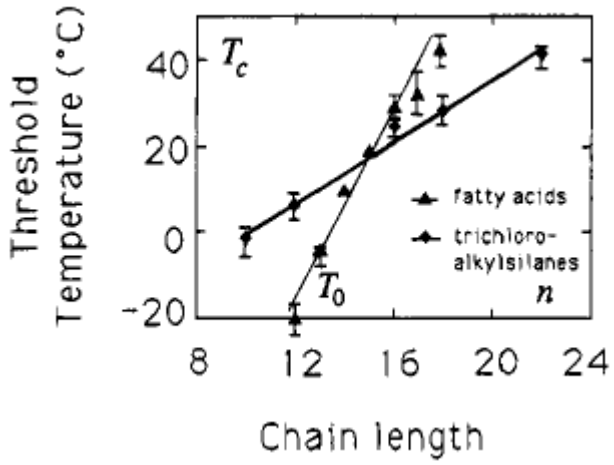

Figure 1.2. Dependence of the threshold temperature T, v.s. the chain length n for the n-alkyltrichlorosilanes deposited on oxidized silicon wafers. Silanization reactions performed below T_c, yield compact monolayers of low wettability. A linear variation of T_c is observed with a slope of -3.5 ℃ per additional methylene group.[27]

For the trimethoxysilane and triethoxysilane, anhydrous toluene is the typical solvent for the silanization and the reaction temperature should be above the boiling point of methanol (65 ℃) and ethanol (78 ℃) in order to push the reaction forwards to the side of the products.

The ability to control the precise placement and areal density of selected functional groups on an ordered substrate-bound molecular assembly makes mixed SAMs valuable.

1.2 Click Reaction

The concept of “click chemistry” was invented by Sharpless and co-workers in 2001,[29] which classifies a particular set of nearly perfect reactions including several well-

known reactions such as hetero-Diels-Alder reaction,[30] the thiol-ene coupling,[31] the Staudinger ligation,[32-34] native chemical ligation,[35,36] the amidation reaction between thio acids and sulfonyl azides (sulfo-click)[37-42] and currently the most popular copper(I)-catalyzed alkyne-azide cycloaddition (CuAAC).[43,44] There are very specific criteria in order for a reaction to be classified as click; that is, the reaction must be "modular, wide in scope, give very high yields, generate only inoffensive byproducts that can be removed by nonchromatographic methods, and be stereospecific." The process must also "include simple reaction conditions, readily available starting materials…no solvent or a solvent that is benign or easily removed, and simple product isolation."[29]

By means of the "click reaction" concept, large macromolecules can be synthesized by coupling small building blocks via heteroatom-containing linkages. Among all these types of "click chemistry", the 1,3-dipolar cycloaddition reaction has emerged as the method of choice to achieve the requirements of ligating two molecules in a general, fast, and efficient process, which includes purely thermal click reactions and reactions accelerated by the addition of various metal species (Ru, Ni, Pt, Pd), but mostly by Cu(I) species, within the reaction system (seen in Scheme 1.1). And all types of the catalyst and solvent are listed in Table 1.1.

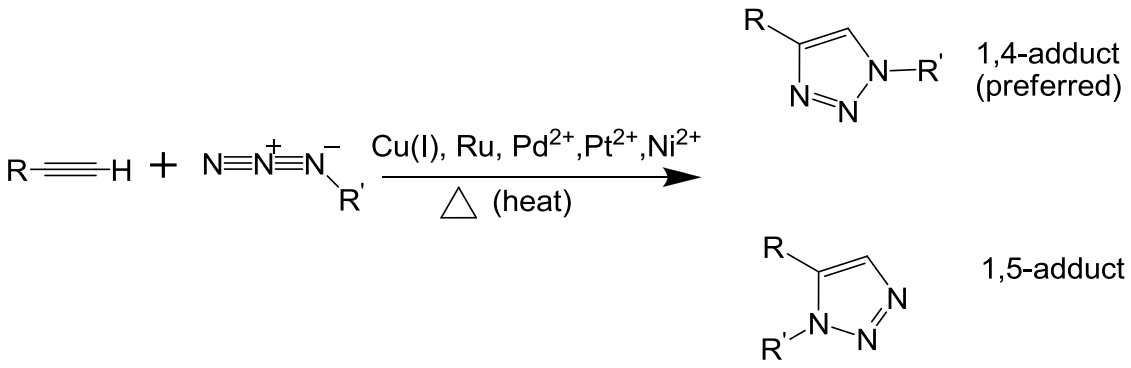

Scheme 1.1. 1,3-dipolar cycloaddition.

Table 1.1. Typical catalysts and solvents for 1,3-dipolar cycloaddition.

Catalysts	Solvents
$Cu(II)SO_4.5H_2O$/sodium ascorbate	Hexane
$Cu(II)SO_4.5H_2O$/copper mental	Toluene/toluene, water
$Cu(OAc)_2$/sodium ascorbate	Butanol/water, alcoholic solvents
$Cu(I)(MeCN)_4PF_6$	Halogenated solvents(CH_2Cl_2,$CHCl_3$)
Cu(I)X X=Br,I	DMF,DMSO
$CuI(I)OTf.C_6H_6$	THF,diethylether
$Cu(I)(PPh_3)_3Br$	
Copper mental/Net_3	
$Cu(II)SO_4$/microwave	
Copper cluster	
Ru-cp* complexes	
Ni^{2+},Pt^{2+}, Pd^{2+}	

The CuAAC reaction is widely used for the modification of surfaces with small molecules or macromolecules, whose advantages include a) often quantitative yields (usually above 95%); b) a high tolerance of all other functional groups present in biological macromolecules such as proteins, polysaccharides, and DNA/RNA; c) an insensitivity of the reaction to solvents, irrespective of their protic/aprotic or polar/non-

polar character; and d) reactions at various types of interfaces, such as solid/liquid, liquid/liquid, or even solid/solid interfaces; e) orthogonality to most other chemical reactions, which means azides and alkynes react primarily with each other, thus pesky side reactions rarely, if ever, occur.

The mechanism of CuAAC reaction is not completely understood, but several proposed mechanism have been published up to date. A thorough investigation into the mechanism of this reaction has been done more recently. Based upon kinetic studies, DFT calculations, and the results from experiments involving a known multinuclear Cu-acetylide compound, a catalytic cycle was proposed (Figure 1.3).[45] What is interesting about this mechanistic investigation is that it suggests not only the involvement of a multinuclear Cu-complex, but also the complexion of a completely formed triazole ring with a Cu-acetylide. Studies involving reaction of multi-azido functionalized compounds imply that this proposal is quite plausible.

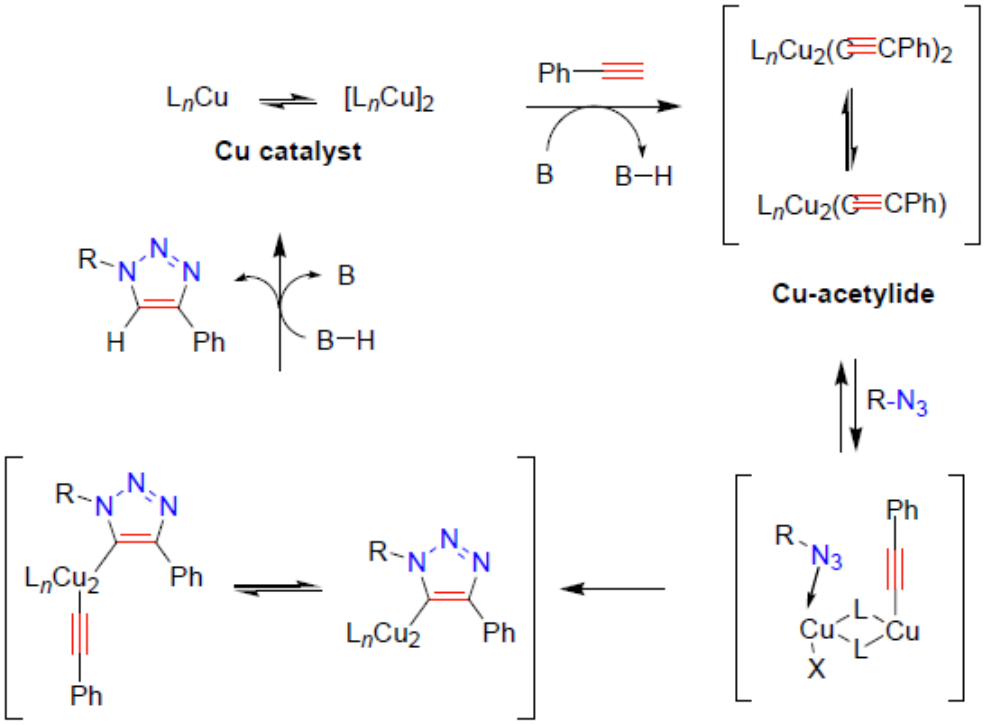

Figure 1.3. Proposed catalytic cycle for the ligand-free CuAAC reaction involving a multinuclear Cu-acetylide complex.[45]

One of the very important applications of CuAAC reaction is its high reactivity in heterogeneous reaction systems, which leads itself to a high efficiency for the derivatization of surfaces. In order to run the reaction, the initial key reaction involves an efficient and simple reaction to allow derivatization of a surface functionalized with azido or terminal acetylenes. This heterogeneous reaction involves a) planar surfaces such as self-assembled monolayers (SAMs); b) a solvent system; c) small molecules or macromolecules with functional alkyne or azide groups.

The reactions of alkynes with azides have been known for several decades and can be induced thermally or catalyzed by transition metal catalysts. The kinetics of the copper-catalyzed and non-catalyzed azide/alkyne cycloaddition reactions have been

studied. Huisgen carried out extensive studies of solvent effects, activation parameters, substituent effects, and orientation effects on the general class of intermolecular uncatalyzed 1,3-dipolar reactions.[46] The kinetics of the ligand-free Cu-catalyzed reaction have been studied, and it is known that the reaction rate is independent of alkyne and second order in metal at catalytic Cu(I) concentrations.[45] When excess amounts of Cu(I) were added to the reaction, the rate law for the reaction was found to be zero order in metal, first order in azide, and second order in alkyne.[47]

Collmann *et al*. were the first to describe the application of mixed SAMs of a mixture of 11-azidoundecanethiol and decanethiol on gold surfaces and use CuAAC to attach ferrocenes onto gold surface, as shown in Figure 1.4. Functionalization was characterized by grazing-angle infrared spectroscopy and x-ray photoelectron spectroscopy. Moreover, time-resolved electrochemical measurements of a ferrocene derivative at a low electrode coverage gave a reaction constant of the click reaction as $k=10^3\ M^{-1}\ s^{-1}$, revealing an extremely high reaction rate.[48]

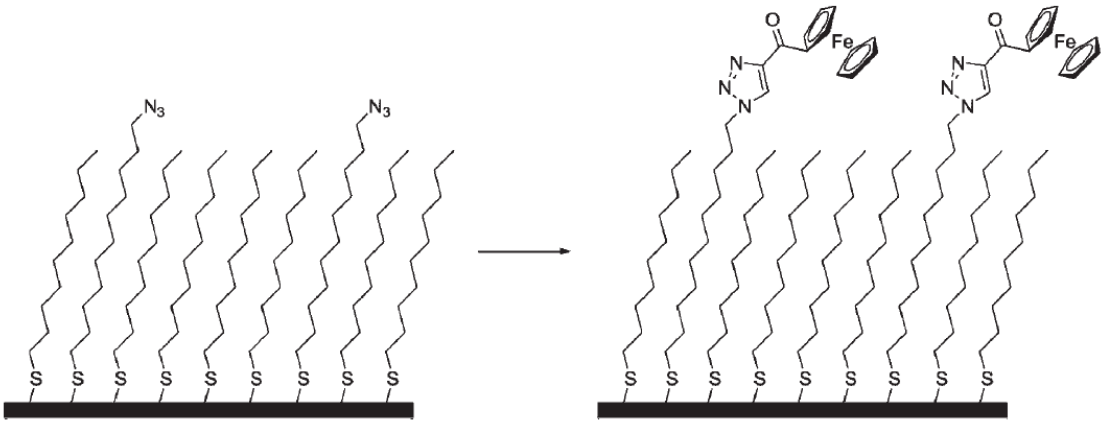

Figure 1.4. Click reaction modified on gold surface.[48]

Christopher *et al*. used uncatalyzed 1,3-dipolar cycloaddition to incorporate chemical functionality onto the surfaces of Au nanoparticles (Scheme 1.2). Fourier transform infrared spectroscopy was manipulated to measure the general kinetic trends and investigate the factors that govern azide/alkyne reactivity at particle surface. They discovered a pseudo-first-order kinetics of a reaction constant of 6×10^{-5} M^{-1} s^{-1}, in good agreement with the solution phase reaction of 9.5×10^{-6} M^{-1} s^{-1}. The roles of ligand length, electronic substitution of the alkyne species, and solvent were also examined. The conversion of azide to triazole is found to depend more strongly on the relative surface coverage of azide terminated alkanethiol than on the ligand length and solvent.[49]

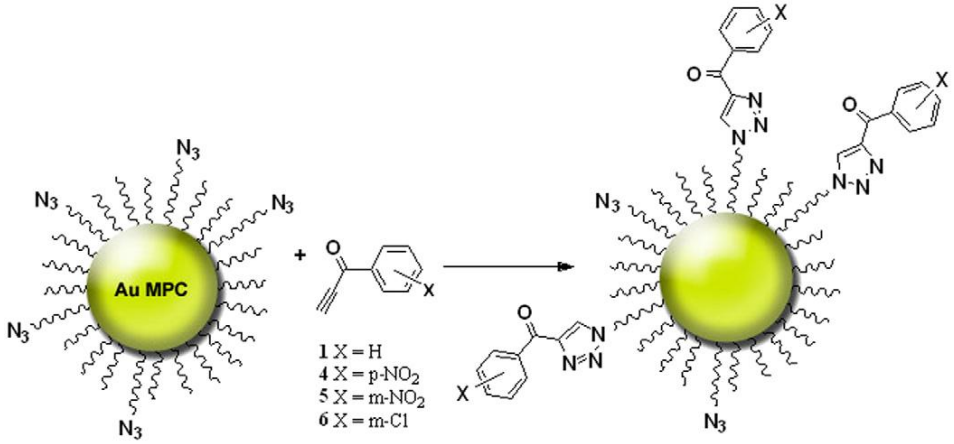

Scheme 1.2.. General scheme of triazole formation on Au MPCs.[49]

1.3 Polymer Brushes

Polymers at interfaces are a field which has fascinated physicists and chemists now for nearly half a century, with respect to both basic and applied research. Polymer brushes are formed by tethering an ensemble of polymer chains to a surface such that each chain has one end absorbed or covalent bound to the surface.[50] There are two types

of interactions that can govern polymer brush formation on a surface: physisorption and chemisorption. Physisorption is a physical attraction between the polymer chains and the surface, whereas, chemisorption requires the formation of a covalent bond between the surface and the polymer brushes.

The end-grafting of polymers onto substrates has emerged as an important means for modifying the surface properties of a wide variety of materials as well as a rich venue for fundamental studies of polymer behavior. In polymer surface modification, synthetic end-function polymers tethered to surfaces can serve to control surface properties including friction and wear, adhesion, wettability and biocompatibility.[51-53] Also surface tethered polymers can be used to stabilize colloidal particles and to minimize protein adsorption.[54,55] Furthermore exciting biological applications such as targeted magnetic hyperthermia,[56] targeted drug delivery,[57] genotyping,[58] and the emerging field of glycomics (i.e., carbohydrate microarrays)[59] all involve immobilizing some biological macromolecule of interest (such as DNA, carbohydrates and proteins) onto the surface of substrates such as silicon wafers, nanoparticles and even micelles.

Tethering polymer brushes to surfaces involves two types of approaches: coupling a preexisting functional polymer to a substrate, a process called "grafting to", or polymerizing the polymer directly from a substrate incorporating a surface bound initiator, a process called "grafting from" or surface initiated polymerization (Figure 1.5).[51] The grafting-from approach is used to produce polymer brushes with high density. However the disadvantage associated with most grafting-from approach is imprecise control of the molecular weight of the brush and uncontrolled polydispersity. The other approach, the grafting-to, offers precise control of polymer molecular weight and

dispersity because chains with desired characteristics can be synthesized and purified in advance. Mixed brushes containing different types of chains in controlled ratios also can be constructed by means of the grafting-to approach.[60] Finally, the grafting-to approach can be conducted under ambient conditions, whereas many versions of the grafting-from approach require demanding moisture-free or oxygen-free conditions.

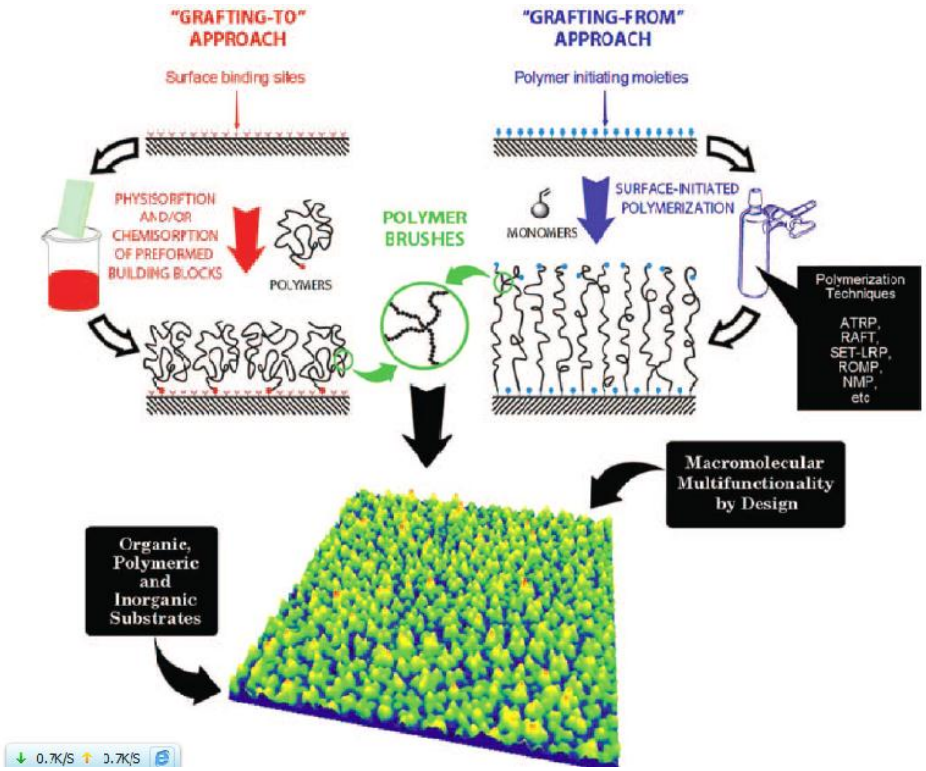

Figure 1.5. Conceptual illustration of the chemical strategies (grafting-to and grafting-from approaches) used to tether functional polymer brushes on a wide variety of substrates.[51]

Homopolymer brushes have been widely studied using theory, which attempts to utilize scaling theory to understand and qualitatively describe the main features and trends exhibited by polymers at interface. Homopolymer absorption from solution was first suggested by Alexander[61] and further studied by de Gennes[62,63] and by Cantor.[64] The

internal structure of polymer brushes was illustrated by numerical and analytical self-consistent field (SCF) calculations, and by computer simulations.

The Alexander model considers a flat, nonadsorbing surface to which monodisperse polymer chains are tethered. The polymer chains consist of N statistical segments of diameter a, the average distance between the tethering point is d, which is much smaller than the radius of gyration of a free, undeformed chain. The Alexander model is based on two assumptions: a) the concentration profile of the layer is step like. That is, the monomer volume fraction within the layer is constant; b) the chains are uniformly stretched. Deformation of densely tethered polymer chains reflects a balance between interaction energy per chains and elastic free energy. Stretching lowers the interaction energy per chain, at the expense of a high elastic free energy. The interplay of these two terms determines the equilibrium thickness of the layer L, in which the chains are stretched perpendicular to the surface. The relationship between the number of statistical segments N and the dimension of tethered and free polymer chains (L and R_g, respectively) under various conditions is summarized in the Table 1.2.

Table 1.2. The relationship between the dimensions of polymer chains and N under various conditions.

	Tethered polymer chain	Free polymer chain
Good solvent	$L/a \approx N(a/d)^{2/3}$	$R_g \sim N^{3/5}$
Theta solvent	$L/a \approx N(a/d)$	$R_g \sim N^{1/2}$
Bulk state	$L \sim N^{2/3}$	$R_g \sim N^{1/2}$

The Alexander approach is a simple free energy balance argument. It does not attempt to examine the details of the conformations of polymer chains or the density profile of chain units at a distance from the grafting surface, which was further well studied by de Gennes.

The de Gennes model describes a set of linear chains that are attached to a wall and immersed in a liquid (pure good solvent or a solution of the same polymer). Compared with Alexander's model, a concentration profile close to the wall is added. For the case that the polymer brush is exposed to good solvent, there are two configurations of polymer chains depending on the grafting density σ. In the first case, the distance z between the anchored polymers is greater than the radius of gyration R_g of the unperturbed chain and the grafting density is so dilute so that the segments of distinct polymer chains do not interact with each other and the resulting polymer configuration is called a mushroom, where $\sigma < N^{-6/5}$ and the thickness of polymer chains L scale with σ^0. When the polymer chains are attached to the surface at a high grafting density, they avoid each other and stretch away from the surface to minimize segment-segment interaction and a polymer brush is formed, where L is proportional to $Na\sigma^{1/3}$. Stretching of polymer

chains decreases the number of possible polymer configuration and hence minimizes the configurational entropy of the polymer chains (Configuration of polymers attached to an interface).

The degree of chain overlap can be compared for chains of different molecular weight using a reduced surface density, Σ, which is independent of molecular weight and type of solvent used and defined as

$$\Sigma \sim \sigma \pi R_g^2 \tag{1.1}$$

The physical meaning of Σ can be understood as how many tethered chains are in the area πR^2 covered by a chain in an unperturbed conformation in the same solvent.[65] For the mushroom regime, Σ ranges from 0 to 3.7/ 3.8 (Figure 1.6). When the tethered chains begin to overlap and enter the cross-over regime, the "single-chain mean-field theory" can be used to describe the interactions.[66] For the strongly stretched polymer brush, a lot of theoretical study and simulation modeling is applied including the numerical, self-consistent-field theory,[67] Monte Carlo[68-70] and scaling methods.[61,63] These approaches yield the same scaling dependence on σ and N such that the thickness of the polymer chains L varies as $L \sim N\sigma^{1/3}$ in good solvent. However, the location of the boundaries between each of these two regimes is not very clear. Even for Σ~12, it has shown the strongly stretched regime was not reached.

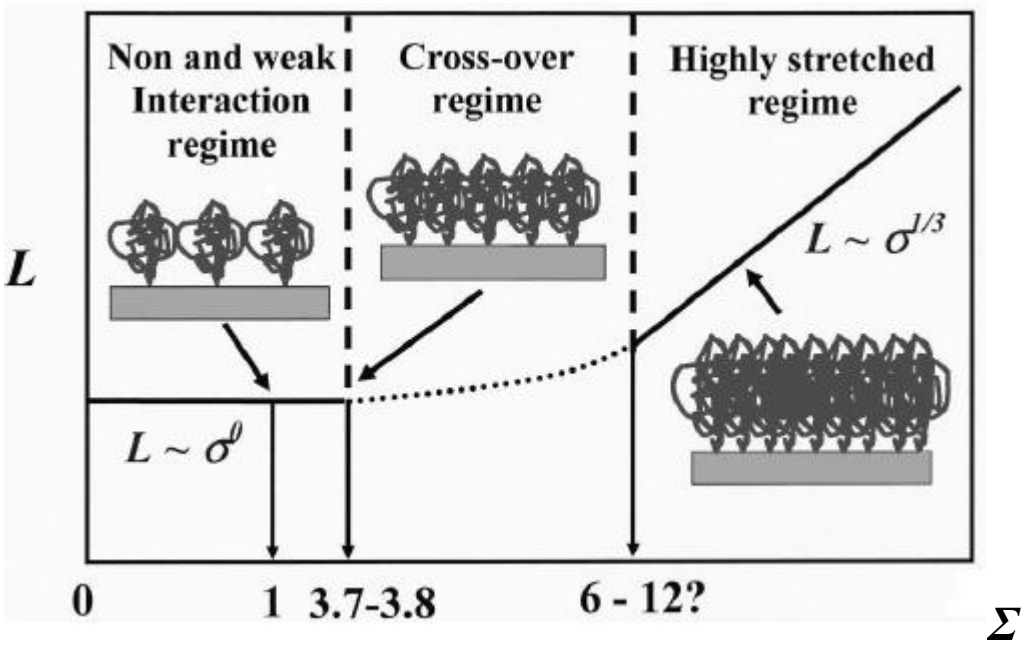

Figure 1.6. Schematic representation of the thickness of tethered chains on a substrate in solution v.s. Σ.[65]

1.4 Kinetics of Polymer Interfacial Reaction

Reaction between a functional polymer and a functionalized interface is far more complex than reactions involving small molecules because of the wide range of factors that can influence the molecular structure and behavior of polymers at interfaces. Kinetics of reactions between small molecules in solution are governed by simple mass action laws. While in the presence of a surface, the actual reaction mechanism may change as a result of interactions between the molecule and the surface. The reaction is very complex because functional groups on polymer chains react more slowly than the same groups on small molecule analogs due to a kinetic excluded volume effect. In addition the reaction rate was a function of the position of the functional group on the

polymer chain.[71] Also the ability of functional polymers reacting to the interface is dependent on such factors as interfacial thermodynamics, solvent quality, polymer molecular weight, polymer architecture, polymer nature, and location of the reactive functional groups. For example, for a reaction of a functional polymer solution reacting with a reactive solid substrate, the thermodynamic conditions dictate that if the solvent prefers the interface, the polymer will not adsorb onto the substrate, hence the indirect contact between the functional group on the polymer and the reactive substrate leads to the fact that the reaction rate is very low. On the other hand, the reaction rate can be orders of magnitude higher.[72] The kinetics of reaction between a functional polymer and a reactive substrate has been studied both by theory and experiments. Brush formation in solution generally leads to lower coupling density due to excluded volume effects.

A theoretical study of the thermodynamics and kinetics of grafting end-functionalized polymer to a reactive interface was carried out by Milner *et al.*[67] and Christian *et al.*[73] They both predicted the existence of two successive regimes in the kinetics of absorption: the first initial one (short time) is governed by the Brownian diffusion of the chains in the solution through the solvent and the reaction rate is very fast, this regime stops rather quickly when chains in a grafted layer start to overlap strongly and to form a barrier towards further adsorption of other chains; the second region slows down because of the increasing energy barrier to penetration when chains must penetrate a relatively dense brush layer as more chains are tethered and the reaction rate declines with the natural logarithm of time. Eventually, the energy gain by forming a chemical bond is offset by the entropic cost of crowding another chain into the interphase and the reaction ceases, a condition referred to as saturation. The equilibrium surface coverage

and thickness of the grafted layer are predicted as a function of molecular parameters such as the molecular weight of the chains, the solution concentration and the energy gained by adsorbing the terminal group.

In the first regime where the kinetics of grafting is controlled by chain diffusion in solution, the time t_1 required to build a mushroom in which the chains just start to overlap is usually very short when the grafting density of polymer chains $\sigma=\sigma^{*}\approx N^{-1}$. Indeed, below σ^{*}, there is essentially no activation barrier and σ (t) is indicated in the following equation:

$$\sigma(t)\sim\left(\frac{Dt}{a^2}\right)^{\frac{1}{2}}\left(\frac{\phi_0}{N}\right) \tag{1.2}$$

where D is the chain diffusion coefficient, a is the Kuhn statistical length, φ_0 is the monomer volume fraction of polymer in the solution, N is the degree of polymerization. The overlapping brush is obtained after the cross-over time t_1:

$$t_1=\frac{a^2}{D\phi_0^2} \tag{1.3}$$

Hence, the reaction rate in the first regime should be proportional to the square root of time. When $\sigma>\sigma^{'}$, the second regime begins. For $\sigma^{*}<\sigma<\sigma^{'}$, there is an intermediate regime.

In the second regime (exponential relaxation regime),

$$\sigma=\sigma_{eq}\left[1-\exp\left(-\frac{t}{t_{eq}}\right)\right] \tag{1.4}$$

where σ_{eq} is the grafting density of polymer chains at equilibrium or saturation, t_{eq} is the time required for the absorption to reach equilibrium. The reaction rate scales with the logarithm of time in the second regime.

Experimental measurements of reaction kinetics for grafting amine-functionalized polystyrene to epoxy functionalized silica substrates, using an indirect GPC-based analysis of the depletion of reactants from the solution, detected three-regimes of kinetic behavior rather than the two predicted by theory for interfacial reactions in the absence of segmental physisorption, as shown in Figure 1.7.[74] The first two regimes agreed with theory, but were followed by a third regime, referred to as "layer assisted tethering". The third regime is not yet fully understood, but has been ascribed to a transition from mushroom to saturated brush morphology that is accompanied by a reduction in the lateral chain dimensions. Atomic force microscopy and Monte Carlo simulations supported this explanation.

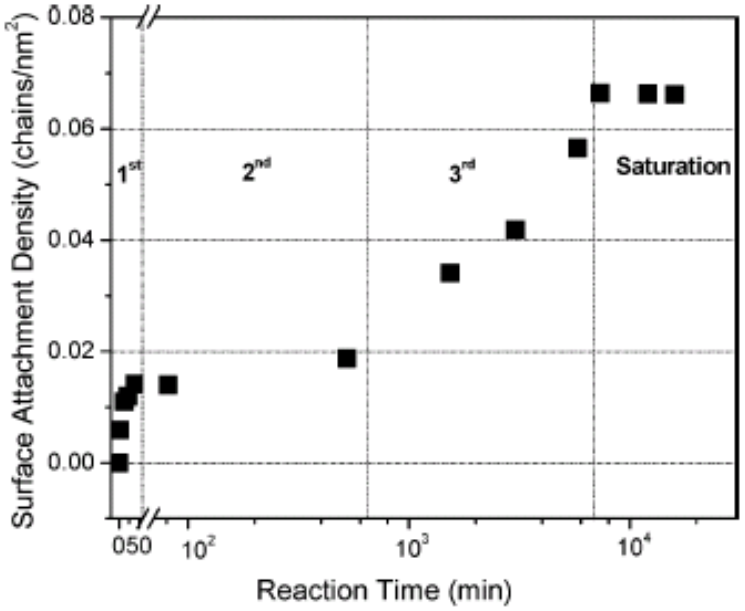

Figure 1.7. Surface attachment density v.s. time for tethering of PS-NH_2-4K. Scatter among replicate measurements is less than the size of the symbol. The horizontal axis changes from linear to log (time) at 50 min. Thin vertical lines separate the three regimes.[74]

The grafting is a self-limiting process, with saturation occurring when the free energy gained by reaction with the surface is balanced with the entropy lost by the brush layer as they adopt stretched configuration away from the interface. The saturation limit for chains grafted from good solvent is low due to excluded volume effect, but can be increased by going to the theta solvent.[72] When the reaction is exposed to a theta solvent, the rate of reaction increased markedly when physisorption occurred, and the equilibrium grafting density was also higher. Furthermore, in the presence of physisorption, the kinetics did not show the characteristic three regimes of behavior, but were more consistent with the kinetics of polymer adsorption.

Penn and Quirk also demonstrated how molecular weight of polymer, temperature, concentration of the polymer solution, position of the functional group on the polymer affect the kinetics of interfacial reactions and the surface density of tethered layers. And they found the surface grafting density declined as the molecular weight increased and there was a negative linear relationship between logarithm of molecular weight and logarithm of surface grafting density.[74] In addition, the grafting density of polymer chains increases and approaches a maximum in response to increase in solution concentration. The solution concentration, above which there is no additional increase in tethered polymer chains, is inversely related to the molecular weight of the dissolved polymer chains.[75] Moreover elevation of the temperature, with solvent held constant, results in an increase in amount tethered.[74] An interesting effect of the nature of the functional group was also reported. When steric hindrance was purposely introduced into the amine group, the initial rates were identical in the diffusion controlled regime, but deviated in the intermediate regime due to the effect of hindrance on the intrinsic functional group reaction rate. The equilibrium brush density, however, was identical for both the amine and hindered amine functional polymers.[76]

The kinetics of sequential brush formation from two different polymers revealed that the second chain added also exhibited the three kinetic regimes of behavior observed for homogeneous brush formation. Heterogeneous brushes from two different polymers have also been prepared by sequentially grafting end-functional polymers onto preexisting polymer brushes with complementary side chain functionality.[60]

The kinetics of attaching polymer brushes to surfaces from a melt of end-functional polymers in contact with a functional substrate has also been studied in the

melt state,[77] wherein it produces a higher grafting density than solution grafting methods, because there are more chains in the proximity of the substrate that can attach without having to penetrate through the forming brush layer, and because the potential barrier for penetration is lower when excluded volume interactions are screened in the melt. Those chains within the first monolayer must only have sufficient mobility to rearrange at the surface in order for the functional end group to bond to the substrate. Luzinov *et al*. studied the reaction of grafting polymer layers from the melt onto a silicon wafer modified with a macromolecular anchoring layer rich in epoxy functional groups.[78] They showed that the equilibrium grafting density of brushes formed from the melt could be increased by the use of a macromolecular anchoring layer, due to the high mobility of the epoxy reactive groups and formation of an interpenetrating zone at the polymer/macromolecular layer. That is, the use of an adsorbed multifunctional macromolecular anchoring layer increased the interfacial volume in which functional groups were located. No changes in the grafting density were observed, however, when the molecular weight or thickness of the anchoring layer were increased. When formed from the melt, the grafting density scaled roughly as N^{δ} with δ in the range of -0.4 to -0.6. The density of grafted chains was also found to decrease linearly with molecular weight (M_w) and above a critical M_w a significant reduction in the rate of interfacial reaction was observed due to the decrease in diffusion rate caused by polymer chain entanglement.

References

(1) Bhushan, B.; Kulkarni, A. V.; Koinkar, V. N.; Boehm, M.; Odoni, L.; Martelet, C.; Belin, M. *Langmuir* **1995**, *11*, 3189.

(2) Maboudian, R. *Surf. Sci. Rep.* **1998**, *30*, 209.

(3) Haneda, R.; Nishihara, H.; Aramaki, K. *J. Electrochem. Soc.* **1997**, *144*, 1215.

(4) Laibinis, P. E.; Whitesides, G. M. *J. Am. Chem. Soc.* **1992**, *114*, 9022.

(5) Zamborini, F. P.; Crooks, R. M. *Langmuir* **1998**, *14*, 3279.

(6) Rehak, M.; Snejdarkova, M.; Otto, M. *Biosens. Bioelectron.* **1994**, *9*, 337.

(7) Rickert, J.; Weiss, T.; Kraas, W.; Jung, G.; Gopel, W. *Biosens. Bioelectron.* **1996**, *11*, 591.

(8) Bard, A.; Berggren, K. K.; Wilbur, J. L.; Gillaspy, J. D.; Rolston, S. L.; McClelland, J. J.; Phillips, W. D.; Prentiss, M.; Whitesides, G. M. *J. Vac. Sci. Technol. B* **1997**, *15*, 1805.

(9) Lercel, M. J.; Craighead, H. G.; Parikh, A. N.; Seshadri, K.; Allara, D. L. *Appl. Phys. Lett.* **1996**, *68*, 1504.

(10) Pan, M.; Yun, M.; Kozicki, M. N.; Whidden, T. K. *Superlattices Microstruct.* **1996**, *20*, 369.

(11) Gun, J.; Sagiv, J. *J. Colloid Interface Sci.* **1986**, *112*, 457.

(12) Legrange, J. D.; Markham, J. L.; Kurkjian, C. R. *Langmuir* **1993**, *9*, 1749.

(13) Maoz, R.; Sagiv, J. *J. Colloid Interface Sci.* **1984**, *100*, 465.

(14) Silberzan, P.; Leger, L.; Ausserre, D.; Benattar, J. J. *Langmuir* **1991**, *7*, 1647.

(15) Wasserman, S. R.; Tao, Y. T.; Whitesides, G. M. *Langmuir* **1989**, *5*, 1074.

(16) Gun, J.; Iscovici, R.; Sagiv, J. *J. Colloid Interface Sci.* **1984**, *101*, 201.

(17) Tillman, N.; Ulman, A.; Schildkraut, J. S.; Penner, T. L. *J. Am. Chem. Soc.* **1988**, *110*, 6136.

(18) Brandriss, S.; Margel, S. *Langmuir* **1993**, *9*, 1232.

(19) Mathauer, K.; Frank, C. W. *Langmuir* **1993**, *9*, 3002.

(20) Mathauer, K.; Frank, C. W. *Langmuir* **1993**, *9*, 3446.

(21) Carson, G.; Granick, S. *J. Appl. Polym. Sci.* **1989**, *37*, 2767.

(22) Kessel, C. R.; Granick, S. *Langmuir* **1991**, *7*, 532.

(23) Schwartz, D. K.; Steinberg, S.; Israelachvili, J.; Zasadzinski, J. A. N. *Phys. Rev. Lett.* **1992**, *69*, 3354.

(24) Finklea, H. O.; Robinson, L. R.; Blackburn, A.; Richter, B.; Allara, D.; Bright, T. *Langmuir* **1986**, *2*, 239.

(25) Rubinstein, I.; Sabatani, E.; Maoz, R.; Sagiv, J. *J. Electrochem. Soc.* **1986**, *133*, C130.

(26) Sabatani, E.; Rubinstein, I.; Maoz, R.; Sagiv, J. *J. Electroanal. Chem.* **1987**, *219*, 365.

(27) Brzoska, J. B.; Benazouz, I.; Rondelez, F. *Langmuir* **1994**, *10*, 4367.

(28) McGovern, M. E.; Kallury, K. M. R.; Thompson, M. *Langmuir* **1994**, *10*, 3607.

(29) Kolb, H. C.; Finn, M. G.; Sharpless, K. B. *Angew. Chem.-Int. Edit.* **2001**, *40*, 2004.

(30) Gacal, B.; Durmaz, H.; Tasdelen, M. A.; Hizal, G.; Tunca, U.; Yagci, Y.; Demirel, A. L. *Macromolecules* **2006**, *39*, 5330.

(31) Posner, T. *Berichte Der Deutschen Chemischen Gesellschaft* **1905**, *38*, 646.

(32) Nilsson, B. L.; Kiessling, L. L.; Raines, R. T. *Org. Lett.* **2000**, *2*, 1939.

(33) Saxon, E.; Armstrong, J. I.; Bertozzi, C. R. *Org. Lett.* **2000**, *2*, 2141.

(34) Saxon, E.; Bertozzi, C. R. *Science* **2000**, *287*, 2007.

(35) Ruttekolk, I. R.; Duchardt, F.; Fischer, R.; Wiesmuller, K. H.; Rademann, J.; Brock, R. *Bioconjugate Chem.* **2008**, *19*, 2081.

(36) Xiao, J. P.; Hamilton, B. S.; Tolbert, T. J. *Bioconjugate Chem.* **2010**, *21*, 1943.

(37) Barlett, K. N.; Kolakowski, R. V.; Katukojvala, S.; Williams, L. J. *Org. Lett.* **2006**, *8*, 823.

(38) Kolakowski, R. V.; Shangguan, N.; Sauers, R. R.; Williams, L. J. *J. Am. Chem. Soc.* **2006**, *128*, 5695.

(39) Merkx, R.; Brouwer, A. J.; Rijkers, D. T. S.; Liskamp, R. M. J. *Org. Lett.* **2005**, *7*, 1125.

(40) Merkx, R.; van Haren, M. J.; Rijkers, D. T. S.; Liskamp, R. M. J. *J. Org. Chem.* **2007**, *72*, 4574.

(41) Shangguan, N.; Katukojvala, S.; Greenburg, R.; Williams, L. J. *J. Am. Chem. Soc.* **2003**, *125*, 7754.

(42) Zhang, X. H.; Li, F. P.; Lu, X. W.; Liu, C. F. *Bioconjugate Chem.* **2009**, *20*, 197.

(43) Rostovtsev, V. V.; Green, L. G.; Fokin, V. V.; Sharpless, K. B. *Angew. Chem.-Int. Edit.* **2002**, *41*, 2596.

(44) Tornoe, C. W.; Christensen, C.; Meldal, M. *J. Org. Chem.* **2002**, *67*, 3057.

(45) Rodionov, V. O.; Fokin, V. V.; Finn, M. G. *Angew. Chem.-Int. Edit.* **2005**, *44*, 2210.

(46) Sustmann, R.; Sicking, W.; Huisgen, R. *Eur. J. Org. Chem.* **2005**, 1505.

(47) Lewis, W. G.; Magallon, F. G.; Fokin, V. V.; Finn, M. G. *J. Am. Chem. Soc.* **2004**, *126*, 9152.

(48) Collman, J. P.; Devaraj, N. K.; Chidsey, C. E. D. *Langmuir* **2004**, *20*, 1051.

(49) Thode, C. J.; Williams, M. E. *J. Colloid Interface Sci.* **2008**, *320*, 346.

(50) Rigoberto C.; Advincula, W. J. B.; Kenneth C.; Caster, J. R. *Polymer Brushes: Synthesis, Characterization, Applications*; VCH Wiley: Weinheim, 2004.

(51) Advicula, R. C. B. W.; Caster, K.; Ruhe, J., Eds. *Polymer Brushes*; Wiley: New Jersey, 2004.

(52) Luzinov, I.; Minko, S.; Tsukruk, V. V. *Prog. Polym. Sci.* **2004**, *29*, 635.

(53) Wainwright, S. A.; Vosburgh, F.; Hebrank, J. H. *Science* **1978**, *202*, 747.

(54) Alberts, B. B., D.; Lewis, J.; Raff, M.; Roberts, K.; Watson, J. D. *Molecular Biology of Cell*; Garland Publishing, Inc., New York & London, 1994.

(55) Ridgway, S. H.; Carder, D. A. *IEEE Eng. Med. Biol. Mag.* **1993**, *12*, 83.

(56) Hergt, R.; Hiergeist, R.; Hilger, I.; Kaiser, W. A.; Lapatnikov, Y.; Margel, S.; Richter, U. *J. Magn. Magn. Mater.* **2004**, *270*, 345.

(57) Horton, J. M.; Bao, C. H.; Bai, Z. F.; Lodge, T. P.; Zhao, B. *Langmuir* **2011**, *27*, 13324.

(58) Wang, D. G.; Fan, J. B.; Siao, C. J.; Berno, A.; Young, P.; Sapolsky, R.; Ghandour, G.; Perkins, N.; Winchester, E.; Spencer, J.; Kruglyak, L.; Stein, L.; Hsie, L.; Topaloglou, T.; Hubbell, E.; Robinson, E.; Mittmann, M.; Morris, M. S.; Shen, N. P.; Kilburn, D.; Rioux, J.; Nusbaum, C.; Rozen, S.; Hudson, T. J.; Lipshutz, R.; Chee, M.; Lander, E. S. *Science* **1998**, *280*, 1077.

(59) Wang, D. N.; Liu, S. Y.; Trummer, B. J.; Deng, C.; Wang, A. L. *Nat. Biotechnol.* **2002**, *20*, 275.

(60) Huang, H.; Penn, L. S.; Quirk, R. P.; Cheong, T. H. *Macromolecules* **2004**, *37*, 5807.

(61) SJ., A. *J. Phys. (Paris)* **1977**, *38*, 977.

(62) Degennes, P. G. *Journal De Physique* **1976**, *37*, 1445.

(63) Degennes, P. G. *Macromolecules* **1980**, *13*, 1069.

(64) Cantor, R. *Macromolecules* **1981**, *14*, 1186.

(65) Kent, M. S. *Macromol. Rapid Commun.* **2000**, *21*, 243.

(66) Carignano, M. A.; Szleifer, I. *Macromolecules* **1995**, *28*, 3197.

(67) Milner, S. T.; Witten, T. A.; Cates, M. E. *Macromolecules* **1988**, *21*, 2610.

(68) Grest, G. S.; Murat, M. *Macromolecules* **1993**, *26*, 3108.

(69) Lai, P. Y.; Binder, K. *J. Chem. Phys.* **1991**, *95*, 9288.

(70) Murat, M.; Grest, G. S. *Macromolecules* **1989**, *22*, 4054.

(71) Morawetz, H. *Accounts Chem. Res.* **1970**, *3*, 354.

(72) Huang, H.; Penn, L. S.; Quirk, R. P.; Cheong, T. H. *Macromolecules* **2004**, *37*, 516.

(73) Ligoure, C.; Leibler, L. *Journal De Physique* **1990**, *51*, 1313.

(74) Penn, L. S.; Huang, H.; Sindkhedkar, M. D.; Rankin, S. E.; Chittenden, K.; Quirk, R. P.; Mathers, R. T.; Lee, Y. *Macromolecules* **2002**, *35*, 7054.

(75) Huang, H. Q.; Penn, L. S. *Macromolecules* **2005**, *38*, 4837.

(76) Penn, L. S.; Hunter, T. F.; Lee, Y.; Quirk, R. P. *Macromolecules* **2000**, *33*, 1105.

(77) Jeon, H. K.; Macosko, C. W.; Moon, B.; Hoye, T. R.; Yin, Z. H. *Macromolecules* **2004**, *37*, 2563.

(78) Iyer, K. S.; Zdyrko, B.; Malz, H.; Pionteck, J.; Luzinov, I. *Macromolecules* **2003**, *36*, 6519.

Chapter 2. Experimental Techniques

Contact Angle, Atomic Force Microscopy (AFM), X-ray Photoelectron Spectroscopy (XPS), ellipsometry, and Attenuated Total Reflectance Infrared Spectroscopy (ATR-IR) are the main analytical techniques used in the current study. In this chapter, a brief introduction to these techniques is given.

2.1 Contact Angle

The contact angle is the angle, conventionally measured through the liquid, at which a liquid/vapor interface meets a solid surface in thermodynamic equilibrium. It quantifies the wettability of a solid surface by a liquid: if the contact angle is small, a drop of the liquid will spread on the solid; if the contact angle is large, the drop of liquid will bead up. The contact angle is specific for any given system and is determined by the interactions across the three interfaces. The concept is illustrated with a small liquid droplet resting on a flat horizontal solid surface as shown in Figure 2.1. The shape of the droplet is determined by the Young equation as following:

$$\gamma_{SV} = \gamma_{SL} + \gamma_{LV} cos\theta_C \tag{2.1}$$

where γ_{SV} is the surface tension between the saturate vapor and the solid, γ_{SL} is the interfacial tension between the solid and the liquid, γ_{LV} is the surface tension between the liquid and the saturate vapor, and θ_C is the equilibrium contact angle. Young's equation assumes a perfectly flat surface, and on a surface that is rough or contaminated, Young's equation is still locally valid, but the equilibrium contact angle may vary from

place to place on the surface, where the highest observed contact angle is the advancing angle θ_A, and the lowest observed contact angle is the receding angle θ_R.

The contact angle is measured using a contact angle goniometer. If the surface is hydrophilic (such as clean Ge suface), the water droplet will spread out across the solid surface and the contact angle will be smaller than 5 °. If the surface is hydrophobic (such as silanized Ge surface), the water droplet will bead up on the solid surface and the contact angle will be larger than 80 °. On highly hydrophobic surface, the water contact angle will as high as 120 °and even higher.

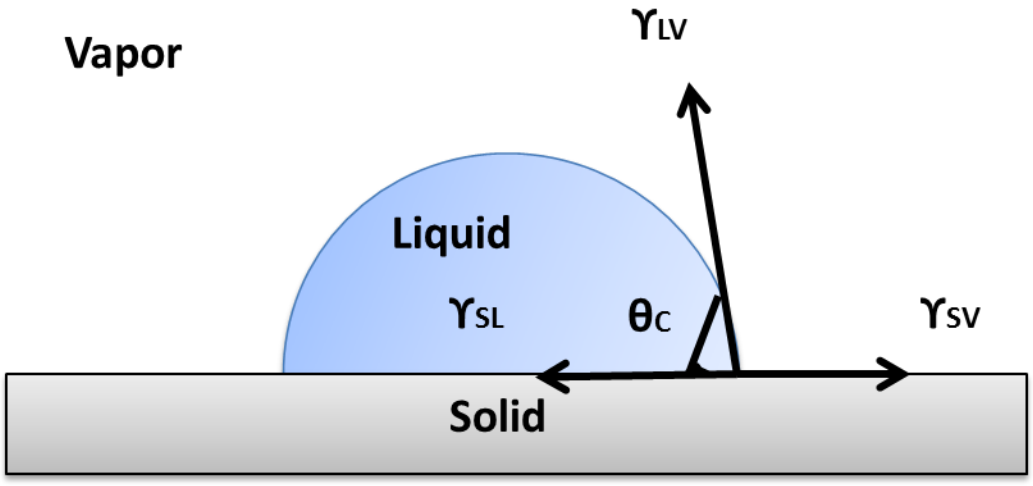

Figure 2.1. Contact angle in thermodynamic equilibrium.

2.2 Atomic Force Microscopy (AFM)

Atomic force microscopy (AFM) or scanning force microscopy (SFM) is a very high-resolution type of scanning probe microscopy, with demonstrated resolution on the order of fractions of a nanometer, to image the topography of a surface. It has different modes including contact, tapping and non-contact (NC) modes, and NC mode is mostly

used for analyzing soft film (SAMs or polymers) samples. AFM consists of a microscale cantilever with a sharp tip (probe) at its end, which is used to scan the specimen surfaces as shown in Figure 2.2. Typically the cantilever is silicon or silicon nitride.

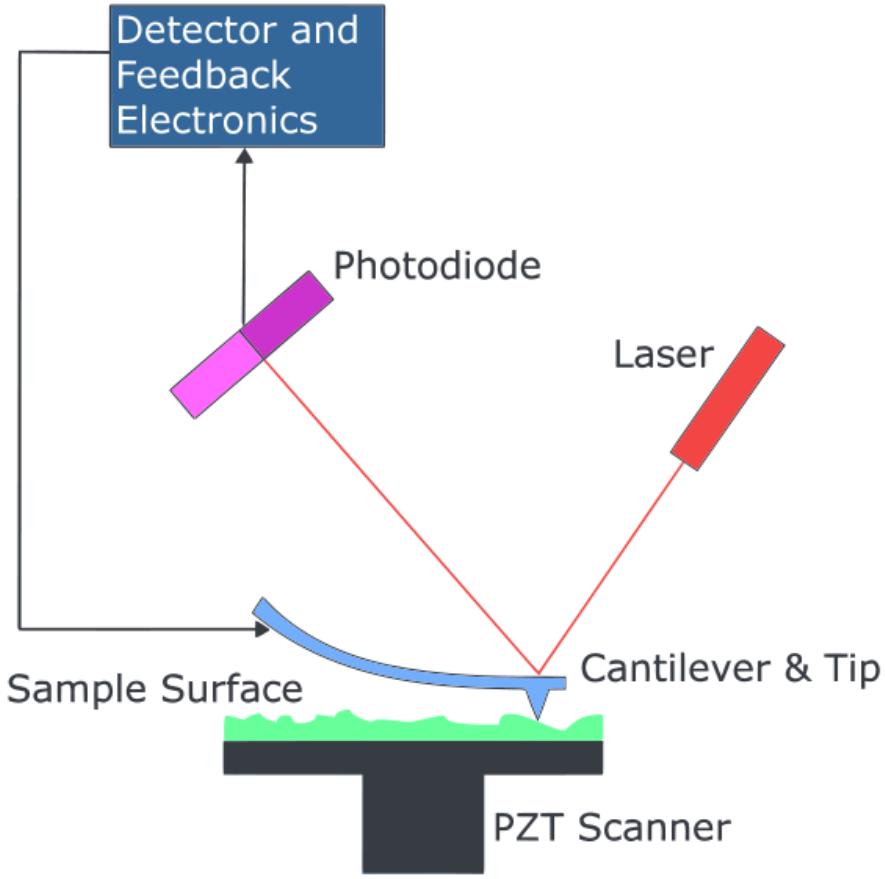

Figure 2.2. Diagram of Atomic Force Microscopy.

The probe is placed on the end of a cantilever (which one can think of as a spring). When the probe approaches a sample surface, the amount of force between the probe and sample is dependent on the spring constant (stiffness) of the cantilever and the distance between the probe and the sample surface. This force can be described using Hooke's Law:

$$F = -kx \tag{2.2}$$

where F is the force exerted by the material, k is the spring constant and x is the distance that the spring has been compressed or stretched away from equilibrium. For the NC mode, the forced measured in AFM is attractive which is largely as a result of long range of van der Waals attraction.

For the NC mode, the probe does not contact the sample surface, but oscillates above the sample on the surface during scanning, where the amplitude of oscillation is typically a few nanometers. The cantilever is held a few Angstroms above the sample surface and the force exerted on the sample is 10^{-12} N so that it would not be distorted or even damaged by contact with the tip. Each cantilever has its own characteristic resonant frequency depending on the fabricated material and its dimension. The operator has to set the driving frequency to match the cantilever's resonant frequency. AFM system detects the change in resonant frequency and the feedback loop system maintains a constant oscillation amplitude or frequency by adjusting the average tip-to-sample distance. Measuring the tip-to-sample distance at each (x, y) data point allows the scanning software to construct a topographic image of the sample surface. The resulting frequency ω of the cantilever can be expressed as follows:

$$\omega = \sqrt{\frac{k_{eff}}{m}} \tag{2.3}$$

where k_{eff} is the effective spring constant. The spring constant of the cantilever changes when the cantilever moves close to the sample surface and the interatomic forces change. The displacement of the cantilever is measured by reflecting a laser beam from the cantilever to a quadrant photodiode. The driving frequency of the cantilever is close

to the characteristic free-space frequency so that the vibration amplitude is sensitive to the distance between the cantilever and the sample surfaces.

2.3 X-ray Photoelectron Spectroscopy (XPS)

X-ray Photoelectron Spectroscopy (XPS) is generally regarded as an important and key technique for surface characterization. This technique, also called ESCA (Electron Spectroscopy for Chemical Analysis), provides a total elemental analysis, except for hydrogen and helium, of the top 10-200 Å (depending on the sample and instrumental conditions) of any solid surface (including films, foils, and conventional solid samples), which is vacuum stable or can be made vacuum stable by cooling. Chemical bond information is also provided. Of all the presently available instrumental techniques for surface analysis, XPS is generally regarded as being the most quantitative, the most interpretable, and the most informative with regard to chemical information. A typical XPS instrument consists of an X-ray source, sample mounting assembly, an analyzer, a detector, data processing and display as shown in Figure 2.3. The sample is mounted in a sample holder and placed in the high-vacuum condition, and the X-ray source is directed toward the sample, emitting monochromatic X-ray photons from magnesium or aluminum Kα. As the photon energy is greater than the binding energy of the electron in the atom of the sample, the electron is rejected from the atom with a kinetic energy approximately equal to the difference between the photon energy and binding energy. The resulting photoelectrons are collected, and their kinetic energy and number are analyzed by a cylindrical analyzer.

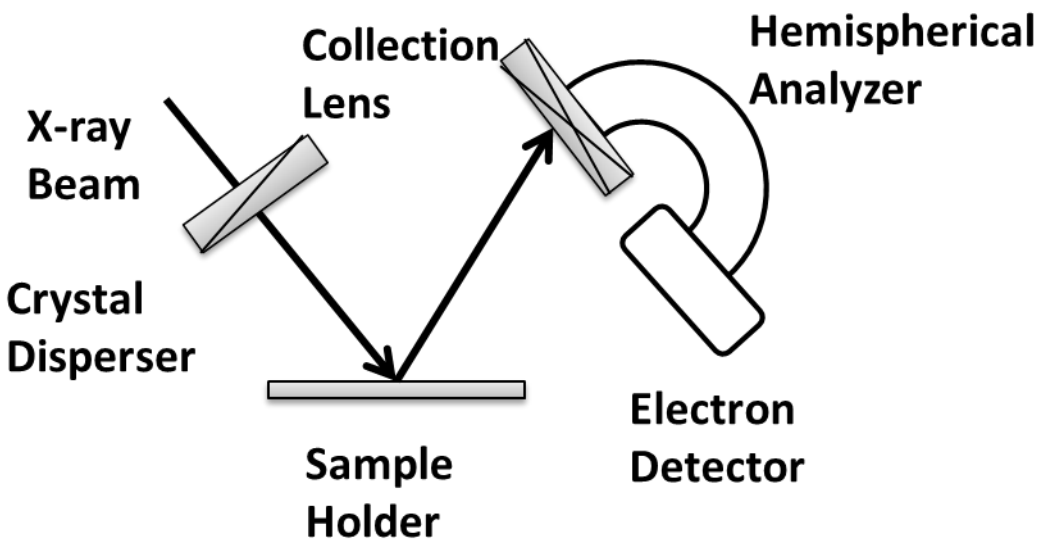

Figure 2.3. Schematic picture of X-ray Photoelectron Spectroscopy.

The basic principle of XPS is the photoelectric effect, the phenomenon for which Einstein received his Noble prize. The basic equation for XPS is

$$E_b \approx h\upsilon - E_k \tag{2.4}$$

where E_b is the electron binding energy, E_k is the electron kinetic energy, measured by the instrument, and hυ is the photo energy (h is Planck's constant and υ is the X-ray frequency). All energies are usually expressed in electron volts (eV). Measuring the kinetic energy allows one to calculate the binding energy. Knowing the binding energy, we can identify the atom.

Two spectra can be obtained from XPS: low resolution survey and high resolution scans. A wide scan (0 to 1000 eV) spectrum is usually used for qualitative identifying the elemental species on the surface, while high resolution spectrum can be applied for quantitative surface analysis. Each element produces a characteristic set of XPS peaks that corresponds to a configuration of the electrons within the atoms. The number of

detected electrons in each of the characteristic peaks is directly related to the amount of the element within the area irradiated. To generate atomic percentage values, each raw XPS signal must first be corrected by dividing its signal intensity by a "relative sensitivity factor" (RSF) and then normalized over all of the elements detected.

The basis for the surface sensitivity of XPS is the fact that electrons do not travel very large distances in matter, due to elastic scattering processes with the matrix or solid medium. The XPS sampling depth d is equal to $t/\sin\theta$ or $3\lambda\sin\theta$, where t is the thickness of the sample, θ is the take-off angle (the angle between the collected photoelectrons and the surface) and λ is the mean free path, when 63% of the electrons have lost energy. As shown in Figure 2.4, it is clear that at low θ, a smaller depth is sampled than at high θ. Therefore there is enhanced surface sensitivity at low θ and greater bulk sensitivity at high θ.

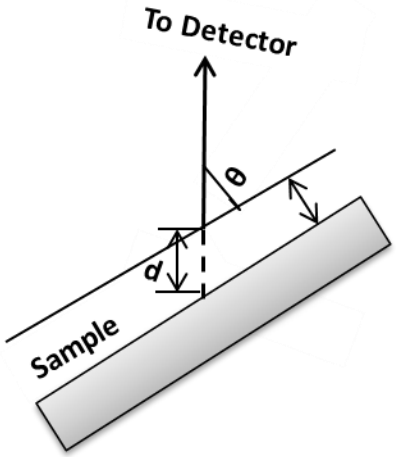

Figure 2.4. The variable angle XPS method, showing that θ decreases, the effective electron travel distance in the sample increases, thus maximizing the surface sensitivity.

If N electrons have traversed a sample of thickness t,

$$N \propto \lambda(1 - e^{-\frac{t}{\lambda}}) \tag{2.5}$$

Hence, the XPS signal for a particular spectral peak is related to the integral of the composition depth profile of the associated atom weighted by the probability of escape for the corresponding ejected photoelectron:[1]

$$I_i(\theta) = \kappa \int_0^{\infty} N_i(x) \exp\left(\frac{-x}{\lambda \sin(\theta)}\right) dx = \kappa \sum_1^N N_i(x_i) \exp\left(\frac{-x_i}{\lambda \sin(\theta)}\right) \tag{2.6}$$

where $I_i(\theta)$ is the density of atom i, θ is the photoelectron takeoff angle, κ is an instrument factor, λ is the photoelectron mean free path, and $N_i(x)$ is the concentration of type i atoms at a depth x. The right hand side of the equation shows the discrete form of the equation where x_i is the position of each type i atom in the sample.

2.4 Ellipsometry

Ellipsometry is an optical technique for the investigation of the dielectric properties (complex refractive index or dielectric function) of thin films. It is a very sensitive measurement technique and provides unequalled capabilities for thin film metrology. As an optical technique, spectroscopic ellipsometry is non-destructive and contactless. Upon the analysis of the change of polarization of light, which is reflected off a sample, ellipsometry can yield information about layers that are thinner than the wavelength of the probing light itself, even down to a single atomic layer. Ellipsometry can probe the complex refractive index or dielectric function tensor, which gives access to fundamental physical parameters and is related to a variety of sample properties, including morphology, crystal quality, chemical composition, or electrical conductivity. It is commonly used to characterize film thickness for single layers or complex multilayer

stacks ranging from a few angstroms or tenths of a nanometer to several micrometers with an excellent accuracy.

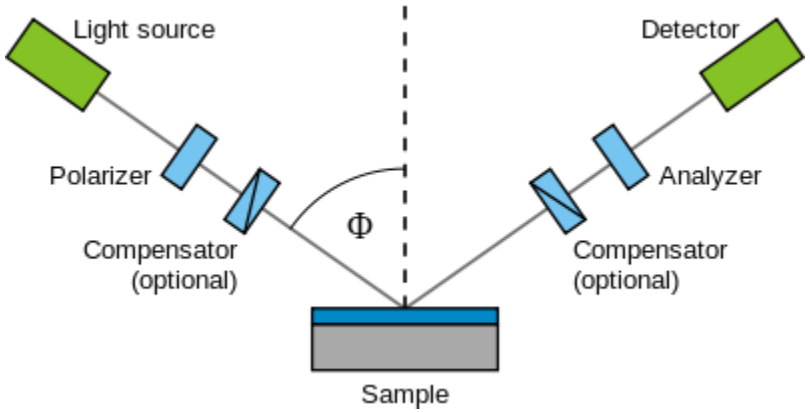

Figure 2.5. Scheme of an ellipsometry.

As shown in Figure 2.5, electromagnetic radiation is emitted by a light source and linearly polarized by a polarizer. It can pass through an optional compensator (retarder, quarter wave plate) and falls onto the sample. After reflection the radiation passes a compensator (optional) and a second polarizer, which is called an analyzer, and falls into the detector.

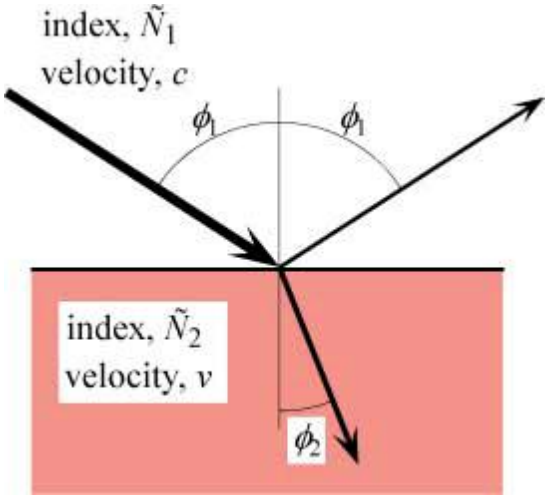

Figure 2.6. The reflection and transmission of light at an interface.

When light enters a non-transparent surface as shown in Figure 2.6, some of the light is reflected back and some light is absorbed by the interface. By the law of reflection, the angle of reflection is equal to the angle of incidence φ_1. According to Snell's law, the refractive angle, φ_2:

$$\frac{sin\phi_1}{sin\phi_2} = \frac{\tilde{N}_2}{\tilde{N}_1} \tag{2.7}$$

where $\tilde{N}_1$ and $\tilde{N}_2$ are the complex indices of refraction for material 1 and 2.

Ellipsometry is a specular optical technique (the angle of incidence equals the angle of reflection). The incident and the reflected beam span the plane of incidence. Light which is polarized parallel to this plane is named p-polarized (p-polarized). A polarization direction perpendicular is called s-polarized (s-polarized), accordingly. When linearly polarized light is reflected from a surface, there is a shift in the phase both p and s components. In certain situation, the phase shift is not the same, resulting in elliptically polarized light after reflection.

The change in the phase difference that occurs up reflection is defined as the parameter Delta, Δ:

$$\Delta = \delta_1 - \delta_2 \tag{2.8}$$

where δ_1 and δ_2 are the phase difference between the parallel and perpendicular components of the wave before and after reflection, respectively. Δ varies from $0\,°$ to $360\,°$. The amplitude of both components may also change upon reflection, and the ratio of the amplitude diminutions is defined as Psi, Ψ:

$$tan\Psi = \left|\frac{r^P}{r^S}\right| \tag{2.9}$$

where r^P and r^S are the Fresnel reflection coefficients (the ratios of the reflected wave amplitude to the incident wave for the parallel and the perpendicular components respectively). Ψ ranges from 0° to 90°.

r^P and r^S are given by the following equations:

$$r^P = \frac{\tilde{N}_2 cos\phi_1 - \tilde{N}_1 cos\phi_2}{\tilde{N}_2 cos\phi_1 + \tilde{N}_1 cos\phi_2} \quad (2.10.1)$$

$$r^S = \frac{\tilde{N}_1 cos\phi_1 - \tilde{N}_2 cos\phi_2}{\tilde{N}_1 cos\phi_1 + \tilde{N}_2 cos\phi_2} \quad (2.10.2)$$

For a single interface where the Fresnel coefficients apply, the reflectance can be written as:

$$\Re^P = |r^P|^2 \quad (2.11.1)$$

$$\Re^S = |r^S|^2 \quad (2.11.2)$$

Analysis of the above equations reveals some interesting discovery as shown in Figure 2.7: r^S is always negative and non-zero; r^p passes through zero and goes from positive to negative; $\Re^S$ is always positive and non-zero; $\Re^P$ goes through a minimum of zero at the same point as r^p is zero. It can be shown mathematically that the angle at which this happens is given by

$$\theta = tan^{-1}(\frac{\tilde{N}_2}{\tilde{N}_1}) \quad (2.12.1)$$

$$sin\theta = cos\phi_2 \quad (2.12.2)$$

This angle is known as the Brewster or polarizing angle when none of the p-polarized light is reflected (all is transmitted), leading to completely s-polarized reflection. At this angle, δ changes discontinuously from π to 0°.

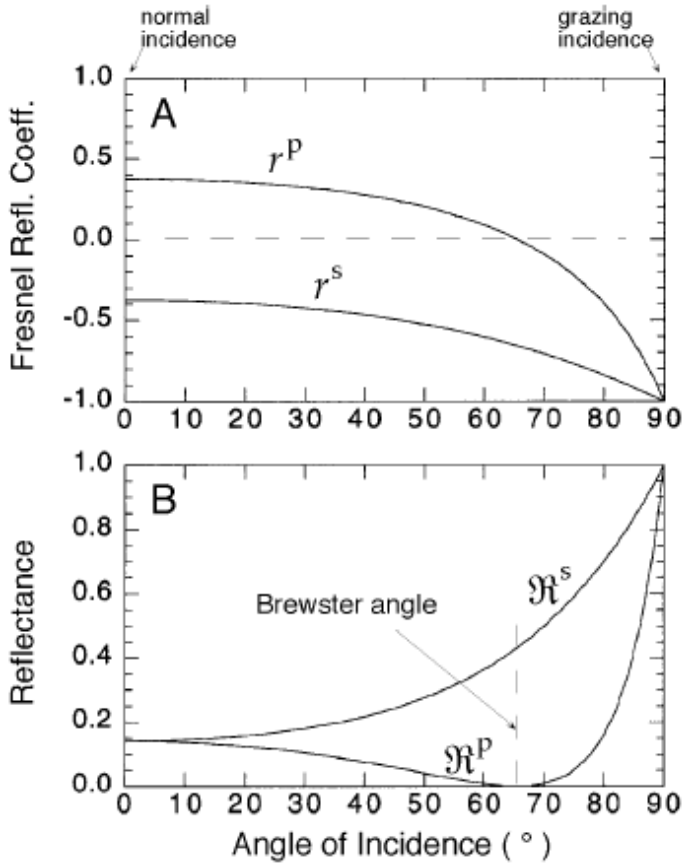

Figure 2.7. The Fresnel coefficients and the associated reflectances for s and p polarized components plotted as a function of the angle of incidence.[2]

The fundamental equation of ellipsometry is

$$\rho = \frac{r^P}{r^S} = \tan \Psi e^{i\Delta} \tag{2.13}$$

where Ψ and Δ are the experimental measured values, ρ is the complex ratio of the total reflection coefficients.

For a thin film on the substrate, r^P and r^S will change, resulting in a change of Ψ and Δ. All these values can be derived from the optical parameters.

Ellipsometry is an indirect method, i.e. in general the measured Ψ and Δ cannot be converted directly into the optical constants of the sample. Normally, a model analysis

must be performed. Direct inversion of Ψ and Δ is only possible in very simple cases of isotropic, homogeneous and infinitely thick films. In all other cases a layer model must be established, which considers the optical constants (refractive index or dielectric function tensor) and thickness parameters of all individual layers of the sample including the correct layer sequence. Using an iterative procedure (least-squares minimization) unknown optical constants and/or thickness parameters are varied, and Ψ and Δ values are calculated using the Fresnel equations. The calculated and values which match the experimental data best provide the optical constants and thickness parameters of the sample.

Spectroscopic ellipsometry, which is used in this thesis, is able to measure Ψ and Δ over a wide range of the optical constants in the model using Cauchy approximation to help eliminate experimental noise and improve the quality of fits. In addition, data should be collected near the Brewster angle to maximize the sensitivity. In the presence of a thin film of a third medium, Ψ does not go to zero completely and the change in δ is less obvious. However, under these conditions the reflectance still goes through a minimum that is not at zero and near the pseudo-Brewster angle. Hence ellipsometry is very sensitive to the thickness of thin film.

2.5 Attenuated Total Reflectance Infrared Spectroscopy (ATR-IR)

Infrared spectroscopy (IR) is the spectroscopy that deals with the infrared region of the electromagnetic spectrum that is light with a longer wavelength and lower frequency than visible light. It covers a range of techniques, mostly based on absorption

spectroscopy. As with all spectroscopic techniques IR is used both to gather information about the structure of a compound and as an analytical tool to assess the purity of a compound.

Infrared refers to that part of the electromagnetic spectrum between the visible and microwave regions. The electromagnetic spectrum refers to the seemingly diverse collection of radiant energy, from cosmic rays to X-rays to visible light to microwaves, each of which can be considered as a wave or particle traveling at the speed of light.

The IR region is divided into three regions: the near, mid, and far IR. The higher-energy near-IR, approximately 14000-4000 cm^{-1} (0.8-2.5 μm wavelength) can excite overtone or harmonic vibrations. The mid-infrared, approximately 4000-400 cm^{-1} (2.5-25 μm) may be used to study the fundamental vibrations and associated rotational-vibrational structure. The far-infrared, approximately 400-10 cm^{-1} (25-1000 μm), lying adjacent to the microwave region, has low energy and may be used for rotational spectroscopy. The mid IR region is of greatest practical use to the organic chemist.

Infrared radiation is absorbed by organic molecules and converted into energy of molecular vibration. In IR spectroscopy, an organic molecule is exposed to infrared radiation. When the radiant energy matches the energy of a specific molecular vibration, absorption occurs. The absorption is due to a particular dipole oscillation generally not affected greatly by other atoms present in the molecule. Thus the absorption occurs at approximately the same frequency for all bonds in different molecules.

There are two types of molecular vibrations, stretching and bending. A molecule can vibrate in many ways, and each way is called a vibrational mode. For molecules with N atoms in them, linear molecules have 3N-5 degrees of vibrational modes, whereas

nonlinear molecules have 3N-6 degrees of vibrational modes (also called vibrational degrees of freedom). Simple diatomic molecules have only one bond and only one vibrational band. If the molecule is symmetrical, e.g. N_2, the band is not observed in the IR spectrum, but only in the Raman spectrum. Asymmetrical diatomic molecules, e.g. CO, absorb in the IR spectrum. In general, the larger the dipole change, the stronger the intensity of the band in an IR spectrum. The complex molecules have many bonds, and vibrations can be conjugated, leading to IR absorptions at characteristic frequencies that may be related to chemical functional groups.

The absorbance of a molecule (A) is determined by the equation of

$$A = \log(\frac{I_0}{I_1}) \tag{2.14}$$

where I_0 and I_1 are the intensities of radiation before and after transmission through the sample.

According to Beer-Lambert equation, the change in absorption from the baseline to the maximum absorption is:

$$A = \epsilon lc \tag{2.15}$$

where ϵ is the molar absorptivity, l is the path length and c is the concentration of the sample. For IR, ϵ and l are constants; hence the absorbance is proportional to the concentration of the sample. By passing a constant wavelength through a sample, analyzing the change in absorption of the sample over times give the possibility of monitoring the rate of chemical reactions.

Surface infrared spectroscopy couples two powerful techniques, infrared spectroscopy and total internal reflection, to study the surface of a sample with a finite

depth into the bulk. The electromagnetic radiation is totally internally reflected through an optically transparent material in contact with the sample. Total internal reflection can occur at the interface of the optically transparent material and the sample only if the index of refraction of the optically transparent material is greater (optically denser) than the index of refraction of the sample (optically rare). Reflectivity of the interface is a measure of the interaction of an electromagnetic filed established within the sample. The spectrum obtained by coupling infrared spectroscopy with internal reflection techniques is characteristic of the sample surface within a finite distance of the interface.

ATR uses a property of total internal reflection resulting in an evanescent wave. Infrared spectra are obtained by putting the sample in contact with an internal reflection element (IRE) (Figure 2.8). IR radiation is focused on the end of the IRE. Light enters the IRE and reflects down the length of the crystal. This reflection forms the evanescent wave which extends into the sample. The penetration depth into the sample is typically between 0.5 and 2 μm, with the exact value being determined by the wavelength of light, the angle of incidence and the indices of refraction for the ATR crystal and the medium being probed. The number of reflections may be varied by varying the angle of incidence. The beam is then collected by a detector as it exits the crystal.[3]

Germanium substrates are particularly interesting ATR crystals because the evanescent field decays over a relatively short distance of about 500 nm imparting good surface sensitivity.

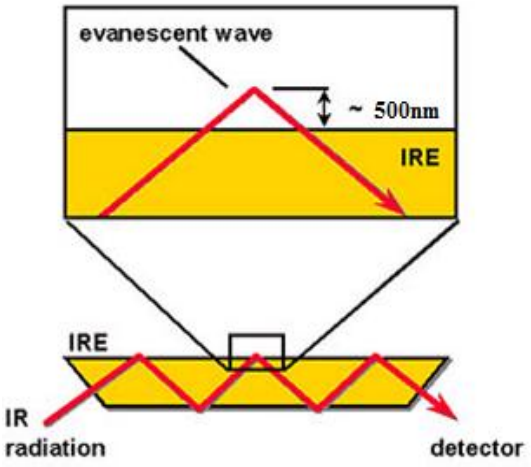

Figure 2.8.Total internal reflection at the interface of an internal reflection element.

The click reaction between azides and alkynes has been selected as a model reaction for this thesis because both the azide and alkyne groups have infrared absorbance bands within the windowpane region of the spectrum near 2100 cm^{-1} where there is no interference from other absorbance bands.

References

(1) Andrade, J. D. *Surface and Interfacial Aspects of Biomedical Polymers*; Plenum Press: New York, **1985**.

(2) Mason, R. B. *Polymer-polymer Adhesion Promotion by Block-Copolymer Addition,* University of Connecticut. **2001**.

(3) Mirabella, F. M. J. *Practical Spectroscopy Series;Internal reflection spectroscopy: Theory and applications*; Marcel Dekker, Inc.: New York, **1993**.

Chapter 3. Azide Functional Monolayers Grafted to a Germanium Surface: Model Substrates for ATR-IR Studies of Interfacial Click Reactions

3.1 Background

Organic Self-Assembled Monolayers (SAMs) have emerged as an effective means for modifying the surfaces of a myriad of different inorganic substrates including metals, semiconductors and insulators. Properly designed SAMs can impart a number of desirable chemical and physical properties that enable their use in numerous applications such as microbiological lubrication,[1,2] biosensors,[3,4] corrosion barriers,[5-7] and lithographic masks,[8-10] to name but a few. SAMs are also used to impart reactive functionality to inorganic substrates, providing sites for subsequent immobilization of a wide variety of sensing molecules such as peptides[11] and nucleotides.[12] Surface-related applications of this nature have fed a growing interest in the heterogeneous chemistry required for sensor fabrication, for example, surface grafting reactions between functional self-assembled monolayers and the aforementioned sensing molecules.[13]

SAMs offer a unique platform for probing the mechanistic details of interfacial reactions in general, a topic of great fundamental and applied interest due to the importance of interfacial reactions in biology and catalysis. Although reactivity at interfaces is a relatively unexplored area, literature data show that factors affecting interfacial reactivity include differences in solvation of interfacial functional groups,

steric hindrance of surface reactants, and local field effects due to forces such as hydrogen bonding.[14]

Attenuated Total Reflection Infrared Spectroscopy (ATR-IR) is a technique that is particularly well suited for sensing applications and that can also be employed for the direct *in situ* characterization of interfacial reactions. ATR-IR involves passing an infrared beam through a trapezoidal ATR plate wherein the beam experiences multiple reflections within the crystal. At each reflection an evanescent field makes a brief excursion outside of the crystal, thereby sampling the infrared spectrum of whatever is in contact with the crystal.[15] If a functional SAM is deposited on the crystal, its reaction with molecules in a contacting solution can therefore be followed by recording the ATR-IR spectrum.[16] Germanium (Ge) substrates are particularly interesting for this application because the evanescent field decays over a relatively short distance of about 500 nm imparting good surface sensitivity.

Sensor applications of ATR-IR therefore require an α, β-heterobifunctional SAM that has a sticky foot on one end that adheres to the Ge crystal and a reactive functional group on the other end for coupling a sensing molecule. While SAMs of this nature are well known for substrates such as silica,[17] silicon,[17] silver,[18] copper[18] and gold,[19,20] the modification of Ge substrates with SAMs has received much less attention, especially relative to silicon substrates.

The chemical bonding of monolayers to silicon substrates generally occurs via the activation of native SiO_2 layers, either by applying an oxidative process to increase the density of Si-OH groups at the surface or by use of a reductive process that passivates the interface by the formation of a Si-H layer.[21-23] Methods for the modification of Ge

substrates are less obvious because unlike SiO_2, GeO_2 is water soluble and Ge itself is less resistant to the oxidation process than is Si. For instance, piranha solution will blacken a Ge surface immediately upon contact. Ge surfaces have been cleaned and activated by immersion in a mixture of H_2O_2 and ethanedioic acid (10%) for 5 min followed by rinsing with MilliQ water.[13]

Heterobifunctional SAMs containing terminal reactive groups provide an excellent route for fabrication of thin film sensors by furnishing reactive sites for coupling a wide range of species to the surface. Reactive functionality capable of Sharpless 'click' reactions[24] is of particular interest as click coupling reactions have high yield and are highly chemoselective, allowing a wide variety of functional analytes to be coupled to surfaces. The copper-catalyzed alkyne-azide 1,3-dipolar cycloaddition reaction (CuAAC) has emerged as the golden standard of click reactions and has been widely used to modify substrates including silica,[17] silicon,[17] gold[19,20] and single-wall carbon nanotubes.[25] While CuAAC chemistry has been described in detail as a means of grafting sensor molecules to surfaces, direct kinetic studies of these interfacial click reactions, although of obvious importance, are rare.

The main purpose of this Chapter is to describe a robust method for creating azide-functional SAMs on Ge ATR-IR crystals. We then show how this platform can be used to quantify the kinetics of an interfacial click reaction with an alkyne-functional reactant. The azide functional monolayers are characterized with AFM, water contact angle analysis, XPS, ellipsometry and ATR-IR, while the kinetics of a model CuAAC reaction with 5-chloro-pentyne are established through time-resolved *in situ* ATR-IR measurements.

3.2 Experimental Section

The overall process used to prepare azide functional Ge crystals for ATR-IR is shown schematically in Scheme 3.1. Three basic steps are involved: cleaning and activation, silanization and azide formation by S_N2 substitution of the terminal bromine atoms. The azide surfaces were then available for reaction with an alkyne-functional reactant, 5-chloro-pentyne in the present case, to form surface grafts through triazole linkages.

3.2.1 Cleaning and Activation

The first step is cleaning and activation. Piranha solutions, used routinely for cleaning Si surfaces, degrade the reflectance properties of Ge surface and blacken the substrate. To avoid this, we have succeeded in using two alternative cleaning methods. In the wet chemical method, the Ge ATR-IR element (or a piece of Ge wafer) was immersed in HNO_3 (38%) for 1 min and rinsed with DI water. The Ge surface was then activated in a mixture of H_2O_2 and ethanedioic acid (in ratio 9:1) for 5 min and abundantly rinsed under DI water. After repeating the process three times, the surface was dried under nitrogen flux. Similar wet chemistry was reported to produce a thick Ge oxide layer with large oxide nuclei that led to a rough surface.[26]

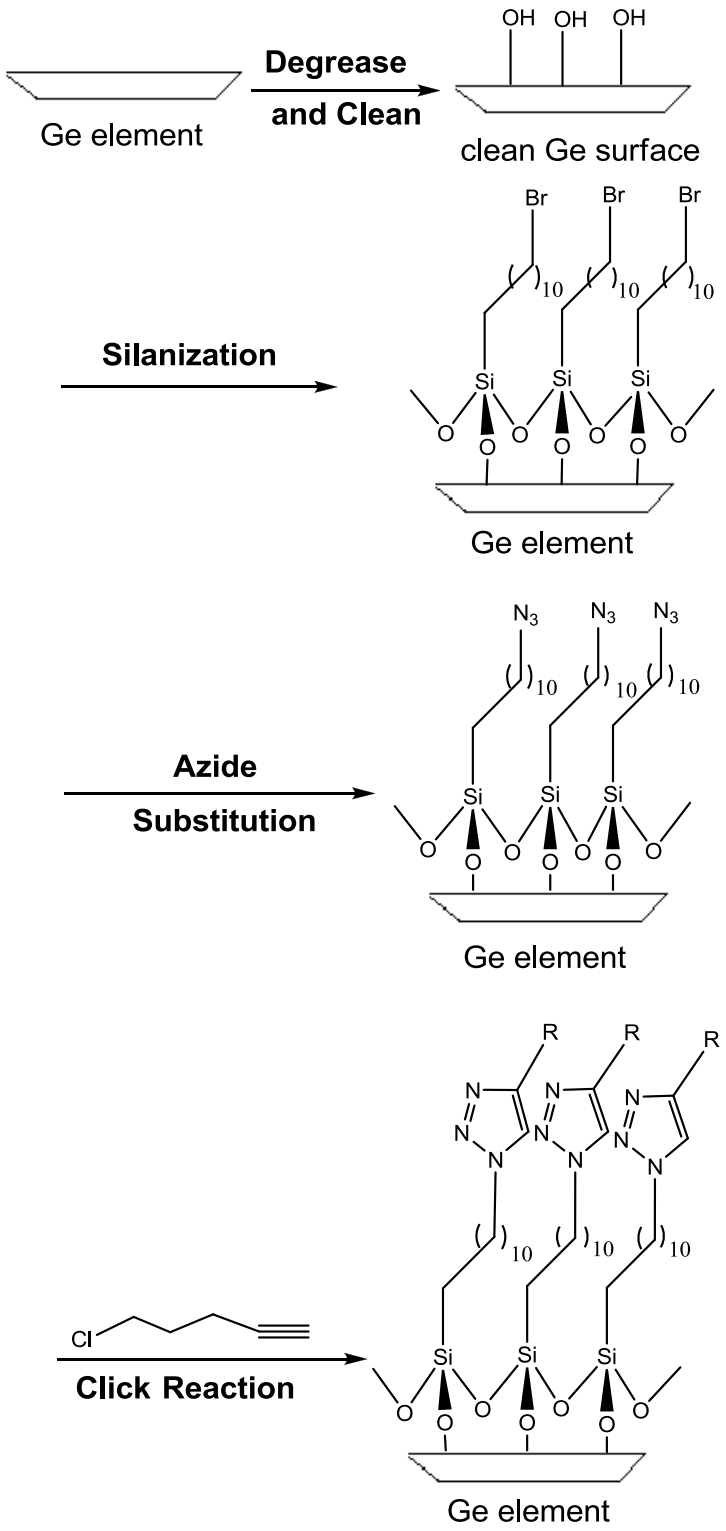

Scheme 3.1. Scheme for preparation of azido-silane monolayers on Ge substrate and subsequent click reaction with functional alkyne, R: -CH_2-CH_2-CH_2-Cl.

For this reason, we also developed a dry chemistry method. The dry chemical method begins first with a wet chemical step for degreasing the Ge surface, that is, sonication in acetone, methanol and DI water for 5 min. After degreasing, the surface was dried with N_2 and exposed to UV-ozone under ambient conditions for 15 min. The UV-ozone treatment provides a relatively gentle means to remove residual hydrocarbons and also promotes the formation of a thin GeO_2 layer on the surface. After UV-ozone treatment, the surface was abundantly rinsed with DI water and dried under nitrogen flux.

3.2.2 Silanization

To improve silanization of the Ge substrate with 11-bromoundecyltrichlorosilane (BUTS), the typical solvent used for silanization of silicon surfaces, toluene, was replaced by the co-solvent system of undecane and carbon tetrachloride, which promotes the formation of surface hydroxyl groups. The activated Ge surface was immersed in a solution of BUTS (0.08% v:v) in a mixture of undecane and carbon tetrachloride (7:3 v:v). The silane was always incorporated at the last moment to avoid prolonged contact with atmospheric humidity which can induce volumetric and surface polymerization of the reagent. The reaction proceeded below 0 ℃ (the transition temperature, T_c,[27-31] which controls the formation of grafted alkyl silane monolayers on hydrophilic substrates) in the freezer for two days. Under these conditions, polymerization of the silane is minimized.

As the Ge substrate was withdrawn from the silane solution, spontaneous dewetting over the entire surface was observed, providing evidence that the treated Ge surface was covered with a dense monolayer of long alkyl chains. Afterwards, the Ge substrate was sonicated in toluene, gently scrubbed with a toluene-soaked tissue to assist

in removal of possible physisorbed multilayers, and rinsed with toluene. Finally, the surface was dried under nitrogen flux.

3.2.3 Azide Substitution

The final step in substrate preparation was azide substitution. The desired azide functionality was imparted on the surface by S_N2 nucleophilic substitution of the terminal bromine groups on the initial SAM. The substitution reaction was carried out by exposing the bromo-terminated surface to a saturated solution of NaN_3 in DMF for 48 h at room temperature, followed by thorough rinsing with DI water. Finally, the surface was dried under nitrogen flux.

3.2.4 Surface Characterization

The progression of surface modifications was characterized by atomic force microscopy (AFM), water contact angle, angle dependent X-ray photoelectron spectroscopy (ADXPS), ATR-IR and ellipsometry measurements.

Contact angle measurements were carried out at room temperature using 8 μL water droplets with a model 100-00 contact angle goniometer (Rame-Hart, Inc.). Values were averages of measurements on more than three different samples at more than three different locations on each sample.

XPS spectra were recorded with a PHI 5500 spectrometer equipped with a hemispherical electron energy analyzer, a multichannel detector, and an Al K-α monochromated X-ray source operated at 15 kV and 23.3 mA. The test chamber pressure

was maintained below 2×10^{-9} Torr during spectral acquisition. A low-energy electron flood gun was used as required to neutralize surface charging. The binding energies (BE) were internally referenced to the aliphatic C1s peak at 284.6 eV. Survey spectra were acquired using an analyzer pass energy of 93.9 eV and a BE resolution of 0.8 eV, while high resolution spectra were acquired with a pass energy of 23.5 eV and a BE resolution of 0.05 eV. The takeoff angle is defined as the angle between the surface and the photoelectron detector. ADXPS was performed by rotating the sample holder to the desired photoelectron takeoff angle. Spectral contributions were resolved using RBD software that fits a series of Gaussian-Lorentzian functions to each chemically shifted photoelectron peak, after subtracting an appropriate background. Bromine loss due to photoelectron damage was minimized by limiting the XPS data collection times to 1h or less.

The thicknesses of SAMs were measured with a Beaglehole Spectroscopic and imaging ellipsometry (Beaglehole Instruments, Wellington, New Zealand) under angle mode (70°) with a fixed wavelength of 632.8 nm. The experimental ellipsometry data were analyzed using Film Wizard software.

Infrared spectra were obtained with a Nicolet 560 FTIR (MCT/A detector, broad range 4000-650 cm^{-1}, liquid N_2 cooled), coupled with an ATR accessory (Horizon™, Harrick Scientific Products Inc.) at a resolution of 4 cm^{-1} with an aperture of 100. The internal reflection element was a 50×10×2 mm trapezoidal Ge crystal with an aperture angle of 45° yielding 13 internal reflections. The Ge crystal was incorporated within a flow through liquid cell.

Noncontact mode AFM measurements using the AutoProbe CP Research Probe head (Veeco Instrument) were performed to study the topography of the SAMs. Silicon cantilevers (dLeversTM) with a spring constant of 2.2 N/m were employed, and the analysis was carried out under air-ambient condition.

3.3 Results and Discussion

3.3.1 AFM

AFM results (see Figure 3.1) demonstrate that the azide SAMs are smooth (RMS roughness is 0.3nm) and featureless, which confirms that the modified substrates are sufficiently smooth to permit surface characterization by ellipsometry, contact angle, and ADXPS analyses.

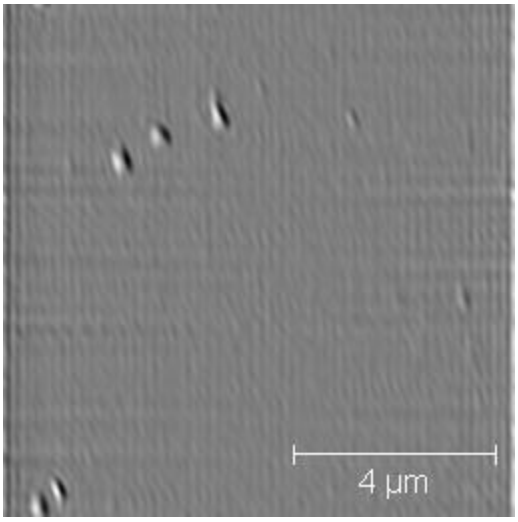

Figure 3.1. A 10 µm×10 µm AFM image of azide monolayer on Ge surface and RMS roughness is 0.3 nm.

3.3.2 Contact Angle Analysis

Water contact angles were measured to characterize the relative hydrophobicity of modified Ge surfaces with respect to bare Ge cleaned by UV-ozone treatment. The results are summarized in Figure 3.1. Contact angles for the bromo- and azide-terminated surfaces agree well with values reported in the literature.

Table 3.1. Water contact angle data for Ge surfaces after modification.

Surface	Contact Angle	Literature Contact Angle
Clean Ge surface	<5 °	<3 °[32]
Br-$(CH_2)_{11}$-Si-	88 °(±3 °)	84 °[33]
N_3-$(CH_2)_{11}$-Si-	80 °(±3 °)	77 °-84 °[34,35]

3.3.3 XPS Results

XPS characterization was applied to monitor changes in the surface chemical composition and to provide electronic structure information at each step in the fabrication process. Figure 3.2 shows the XPS spectrum for the clean Ge surface, the XPS spectrum after silanization with BUTS and the XPS spectrum after azide substitution of Br. Compared with the clean Ge surface, characteristic bromine peaks are observed for BUTS modified substrate at ~72 eV for the Br ($3d^5$) electronic state, and ~184 eV for the Br ($3p^3$) electronic state, confirming successful silanization of the Ge surface with BUTS. The Br $3d^5$ and $3p^3$ peaks disappear after azide substitution as shown in the bottom of Figure 3.2. In addition, a nitrogen signal is detected at ~400 eV. The nitrogen doublet

structure characteristic of the azide can be seen in the high resolution spectrum shown in the inset in the Figure. The smaller peak is seen at 405 eV and the larger peak is seen at 400 eV, consistent with previous results for the azide doublet peak location.[35] Although the ratio of areas of the two peaks is not exactly 1:2 as expected, the difference in areas may be attributed to degradation associated with prolonged scanning.

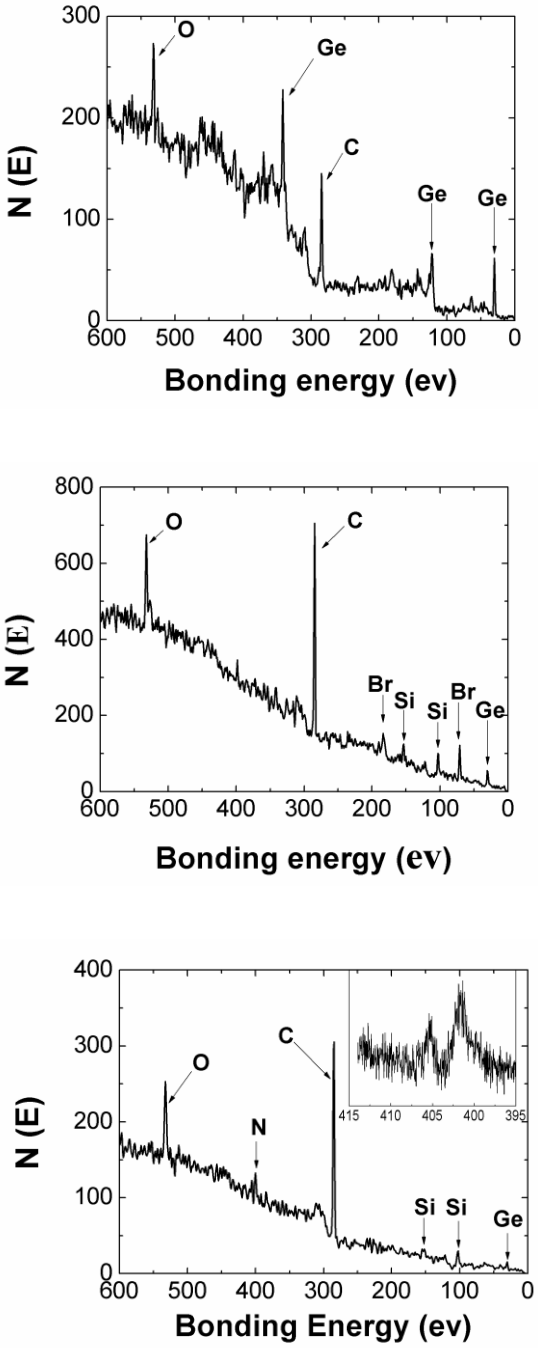

Figure 3.2. XPS spectrum of Ge surface after UV-ozone cleaning (top). XPS spectrum after silanization with BUTS (middle). XPS spectrum after azide substitution of Br (bottom); the insert shows the typical azide doublet peak structure.

3.3.4 IR Results

IR spectra were collected for modified surfaces in order to track the changes brought about by each chemical modification. The spectra for the silanized and azide functional surfaces can be seen in Figure 3.3. The asymmetric CH_2 (2950-2873 cm^{-1}) and symmetric CH_2 (2872-2812 cm^{-1}) associated with the aliphatic portion of the BUTS SAM appear in the spectrum for the silanized surface. The presence of the surface azide is indicated by the adsorption band near 2100 cm^{-1}.

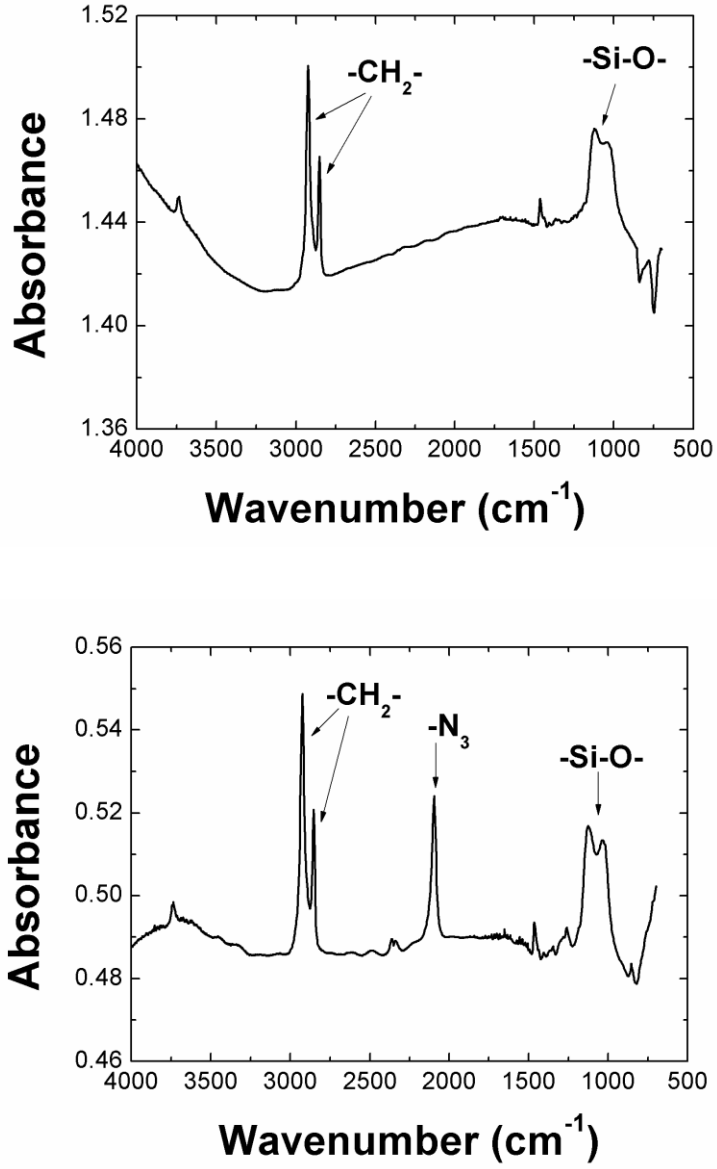

Figure 3.3. ATR-IR spectra for the modified Ge surfaces: after silanization (upper spectrum), after azide substitution (lower spectrum).

3.3.5 Ellipsometry Measurement

The ellipsometric thickness of the azide-terminated layer, determined to be 17.8 ± 1 Å, agrees well with the calculated model thickness of the azide-functional

monolayer, 17.6 Å, the latter calculated for a complete SAM layer with fully extended alkyl chains oriented normal to the substrate (see modeling section below). These data support the formation of a densely packed azide-functional monolayer with little if any multilayer formation.

3.3.6 ADXPS Analysis

3.3.6.1 Molecular Model

The XPS signal for a particular spectral peak is related to the integral of the composition depth profile of the associated atom weighted by the probability of escape for the corresponding ejected photoelectron:[36]

$$I_i(\theta) = \kappa \int_0^{\infty} N_i(x) \exp\left(\frac{-x}{\lambda \sin(\theta)}\right) dx = \kappa \sum_1^N N_i(x_i) \exp\left(\frac{-x_i}{\lambda \sin(\theta)}\right) \quad (3.1)$$

where $I_i(\theta)$ is the density of atom i, θ is the photoelectron takeoff angle, κ is an instrument factor, λ is the photoelectron mean free path (approximately 36 Å[37,38]), and $N_i(x)$ is the concentration of type i atoms at a depth x. The right hand side of the equation shows the discrete form of the equation where x_i is the position of each type i atom in the SAM. In using the discrete form of the equation, one simply adds up the contributions of each atom based upon their positions provided by a molecular model.

The atomic depth distribution was estimated by applying Chem3D to model the SAMs in an all-trans extended conformation oriented normal to the substrate (Figure 3.4). The calculated thickness for this conformation, 17.6 Å, agrees well with the ellipsometric thickness, 17.8±1 Å, determined experimentally. Once the positions of each atom were calculated, the discrete form of equation 3.1 was applied to calculate the XPS signals of

each type of atom in the SAMs. Bromine, carbon (summed over all the carbon atoms[39]) and silicon signals were calculated in this fashion and are reported in Table 3.2, where they are compared to experimentally determined atomic percentages.

Because the nitrogen signals were weak due to the low quantum yield and possible photoelectron-based degradation, modeling of the XPS spectra was limited to the BUTS monolayer. The data collected in Table 3.2. Experimental and model XPS calculations of atomic composition for a BUTS monolayer. Both are calculated for a 30 ° take-off angle.indicates that the atomic composition calculated from the molecular model assuming normal orientation agrees well with the experimental composition data, supporting the hypothesis that the BUTS SAMs are oriented more or less normal to the surface with the silicon atom located on the surface and bromine atom at the air interface. The experimental bromine signal is lower than expected from the calculation, however, we have observed bromine loss for these materials due to photoelectron-based degradation; the loss of fluorine by this mechanism during XPS measurements is well known.[40]

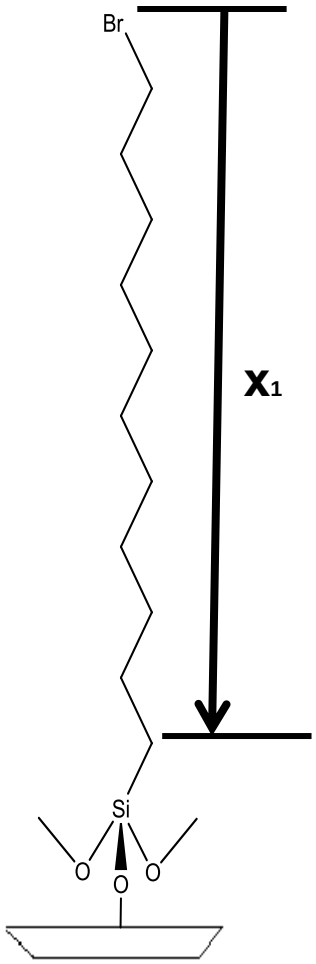

Figure 3.4. Spatial distribution of atoms in the BUTS SAM. x_1 is the depth from the monolayer to the air interface.

Table 3.2. Experimental and model XPS calculations of atomic composition for a BUTS monolayer. Both are calculated for a 30 °take-off angle.

Atom	XPS model (%)	XPS Experiment (%)
Br	11.5	8.0(±1.0)
C	83.6	85.7(±1.1)
Si	4.9	6.3(±0.8)

3.3.6.2 Substrate-Overlayer Model

Angle dependent XPS measurements can be used to estimate a thickness for the SAMs based upon application of the susbstrate-overlayer model described in (3.2):[36]

$$\frac{I_L}{I_S} = \frac{Y_L}{Y_S}\left[\exp\frac{d}{\lambda\sin(\theta)} - 1\right] \quad (3.2)$$

where I_L is the intensity of a signal originating only in the overlayer (N, C, Si) and I_S is the intensity of a signal associated with the substrate (Ge), Y is yield (photoionizaiton cross-section) of each signal and d is the thickness of the monolayer. The thickness may be calculated graphically as Equation 3.2 predicts that the term $\ln(\frac{I_L}{I_S}+1)$ is linearly dependent on $1/\sin\theta$ with a proportionality constant (i.e., slope) of d/λ.

Multiplex scans for each atom were performed at four take-off angles (TOA): 45 °, 35 °, 25 °, 15 °. Plots of $\ln(\frac{I_L}{I_S}+1)$ against $1/\sin\theta$ for all three atoms produced straight lines as shown in Figure 3.5, in good agreement with the prediction of (3.2).

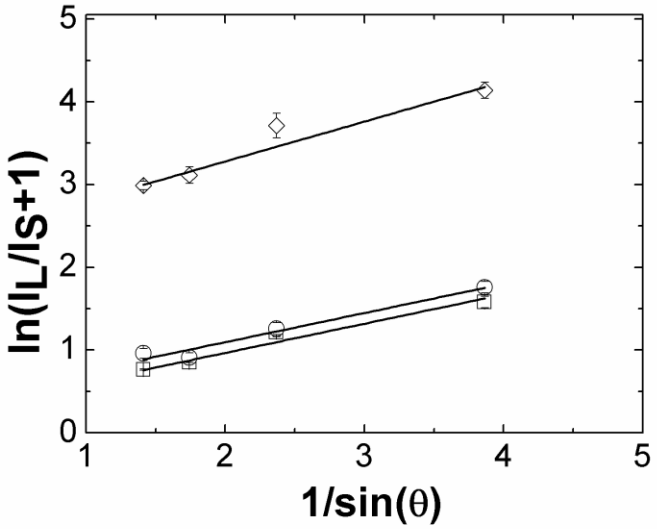

Figure 3.5. Plots of $\ln(I_L/I_S+1)$ vs. $1/\sin(\theta)$: the diamonds are the results for the carbon signals, the circles are based on the nitrogen signals and the squares are the results for the silicon signals.

The calculated thicknesses from the three straight lines from Figure 3.5 are 17.4 Å, 15 Å, and 15 Å, from analysis of the carbon, nitrogen and silicon signals, respectively. The carbon-based value is most reliable because it reflects the signals from many more atoms. The XPS-derived thickness, 17.4 Å agrees well with the ellipsometric thickness, 17.8 Å as well as the molecular model prediction of 17.6 Å.

3.3.7 Surface Density of Azide Functional Monolayer

The surface density of azide-silane layer was calculated based on the equation:[41]

$$\sigma = \frac{N_A d \rho_{dry}}{M_W} \tag{3.3}$$

where d is the ellipsometric layer thickness, ρ_{dry} is the density of the dry silane coupling agent (assuming a well-packed fully-extended monolayer with a ρ_{dry} of 1.0 g/cm^3), M_W is the molecular weight of the silane (N_3-$C_{11}H_{22}$-Si-), and N_A is Avogadro's number. Applying this relation to our data we find an areal density of 3 chains/nm^2 for our silane monolayer, which compares well with a previously reported value of 2.1 chains/nm^2 for the silane agent of 1-[5-methoxy-2-nitro-4-(3-trimethoxysilylpropyloxy)phenyl]ethyl N-succinimidyl carbonate,[41] and indicates that we have prepared a dense, high-quality monolayer.

3.3.8 Click Reaction at Interface

The Ge crystal was placed into a liquid ATR flow cell. A solution of 5-chloro-pentyne (10 µl, 0.095 mmol), $CuSO_4$ $5H_20$ (1 mg, 0.004 mmol) and sodium ascorbate (1.68 mg, 0.008 mmol), dissolved in a co-solvent of DMF (1 ml) and H_2O (10 µl), was injected into the cell whereupon it contacted the azide functionalized Ge surface to initiate the click reaction. The reaction was performed at room temperature in the air for 1 day with spectra recorded every 110 seconds with 100 scans acquired. Background was collected with the bare Ge crystal. Automatic baseline correction methods were applied to all the spectra. The absorbance band for alkyne groups (around 2112 cm^{-1}) overlaps with that for azide groups (see Figure 3.6), necessitating development of a background subtraction procedure through which the decrease in the intensity of the azide absorbance band (around 2100 cm^{-1}) as a function of time could be monitored during the CuAAC reaction. Figure 3.6 shows a typical result for ATR-IR monitoring of the interfacial click reaction.

The azide absorbance band was isolated from the overlap by subtracting a weighted spectrum of a solution of 5-chloro-pentyne on the unmodified Ge surface from the reaction spectrum.[16] The subtraction was performed by adjusting the weighting factor until the contributions of absorbance bands below about 1700 cm^{-1} were completely removed. Examples of the subtraction procedure are shown in Figure 3.7.

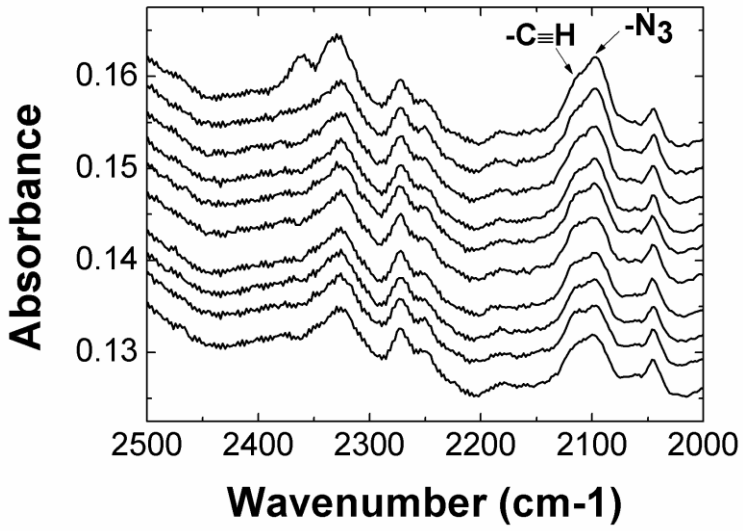

Figure 3.6. ATR-IR spectral changes during the CuAAC reaction of an azide-functional Ge crystal with 5-chloro-pentyne. The topmost spectrum was recorded at the beginning of the reaction and afterwards the series of spectra was recorded every 110 seconds. For illustration purposes, each spectrum was shifted vertically 0.0028 from the previous one.

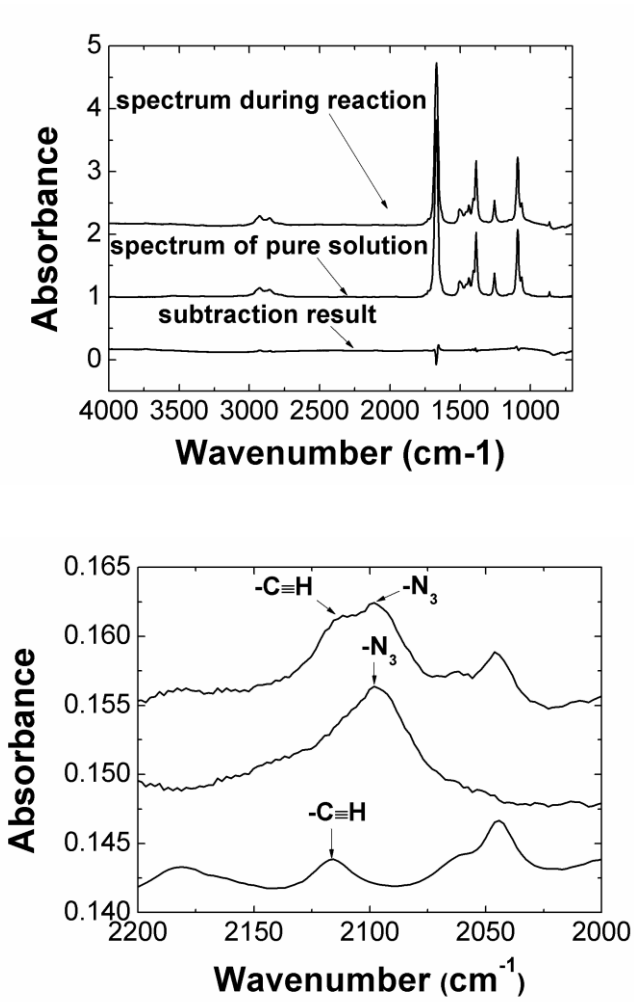

Figure 3.7. The top Figure illustrates the subtraction procedure for the complete ATR-IR spectra.: the spectrum 10 min into the CuAAC reaction (top); the 5-chloro-pentyne solution on unmodified Ge (middle); the spectrum for 10 min of reaction after subtracting the weighted spectrum for the solution of 5-chloro-pentyne (bottom). The bottom Figure illustrates the subtraction procedure for ATR-IR spectra in the azide absorbance region: the spectrum 10 min into the CuAAC reaction (top), the spectrum of a pure solution of 5-chloro-pentyne on the unmodified Ge substrate (bottom) and the spectrum for 10 min of reaction after subtracting the weighted spectrum of the solution of 5-chloro-pentyne (middle) are shown.

The kinetics of the ligand-free copper-catalyzed reaction are independent of the alkyne concentration and second order in metal at catalytic Cu(I) concentration.[42] When excess amounts of Cu(I) are added to the reaction, the rate law for the reaction is zero order in copper, first order in azide, and second order in alkyne.[43] Since we have used an excess of Cu(I) and alkyne groups without ligand in our experiments, the kinetics is expected to show a first order dependence on azide concentration at the beginning of the reaction, as C[alkyne]≫C[triazole] and C[azide]≫C[triazole].[44,45] Based upon a pseudo first order approximation, the time dependence of the azide concentration should follow the expression:

$$1 - y = \exp(-kt) \tag{3.4}$$

where y is the conversion of surface azide to triazole, k is a first-order reaction constant and t is time. When more azide groups are converted to triazole, the kinetics are predicted to transition to a second order dependence on azide concentration, specially when C[alkyne]≫C[triazole] but C[azide]≈C[triazole].[44,45] Based upon a second order kinetics, the time dependence of the azide concentration should follow the expression:

$$\frac{1}{C_0}\left(\frac{1}{1-y} - 1\right) = k't \tag{3.5}$$

where C_0 is the initial concentration of surface azide, y is the conversion of surface azide to triazole, k' is second-order reaction constant and t is time.

To ensure that the surface azides were the limiting reactant, the reaction was repeated with a higher concentration 5-chloro-pentyne solution (20 µl, 0.0190 mmol), with $CuSO_4\,5H_20$ (1 mg, 0.004 mmol) and sodium ascorbate (1.68 mg, 0.008 mmol),

dissolved in a co-solvent of DMF (1 ml) and H_2O (10 µl). Data for the two 5-chloro-pentyne solutions are in good agreement as shown in Figure 3.8.

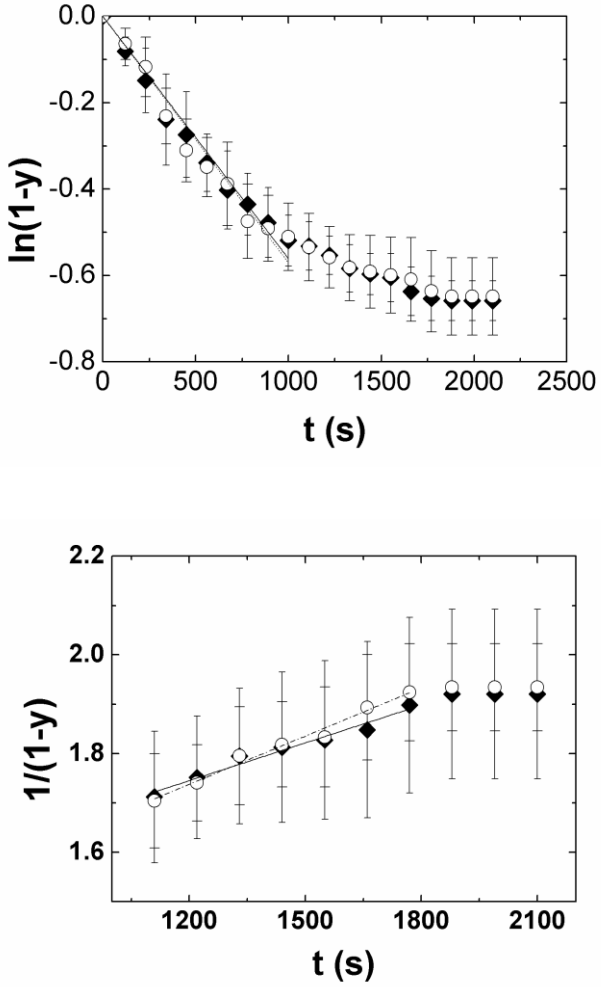

Figure 3.8. First order rate plot (top) and second order rate plot (bottom) for the CuAAC click reaction between 5-chloro-pentyne and an azide functionalized Ge surface: the diamonds are the results from the higher concentration 5-chloro-pentyne solution; the circles are the results from the lower concentration solution; the straight line is the linear fit of results from the higher concentration solution; the dotted line is linear fit of results from lower concentration solution. Errors of data are from repeatability of experiments.

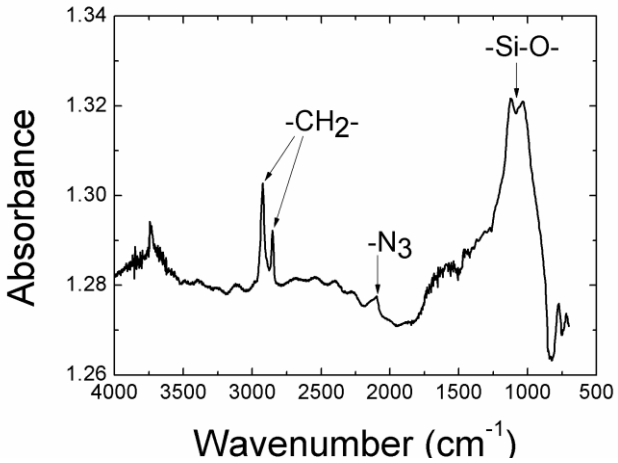

Figure 3.9. ATR-IR spectrum after the CuAAC reaction.

The data follow first order kinetics for the first 1000 seconds with a rate constant of 0.034 ± 0.0003 min^{-1} and second order kinetics up to the point of surface saturation with a rate constant with 0.017 ± 0.002 $min^{-1}/(chains/nm^2)$ and reaching an ultimate conversion of about 50%. The limited ultimate conversion may be a steric effect because the 5-chloro-pentyne reactant is larger than the spacing between surface azide groups. To further examine this possibility, the germanium crystal was removed from the ATR cell after the reaction and was washed with a copious amount of water to remove the excess catalyst, followed by rinsing with toluene to remove any residuals of the reactant solution. The spectrum taken after washing shows a dramatic decrease in intensity of the azide absorbance (Figure 3.9). The ratio of peak areas (azide:CH_2) drops from a value of 0.41 before the reaction to a value of 0.21 after the CuAAC reaction.

If the ultimate conversion is limited by steric effects due to the finite size of the 5-chloro-pentyne reactant, the limiting conversion should provide an estimate of the occupied surface area of a 5-chloro-pentyne molecule. A limiting conversion of 50 % suggests that the size of the 5-chloro-pentyne is about twice the surface area per azide

group. The area occupied by each azide is 0.33nm^2 (i.e., the calculated SAM density is 3 molecules/nm^2) suggesting that each 5-chloro-pentyne molecule occupies about 0.66 nm^2 on the surface. This value is similar to the reported cross-sectional areas[46] of adsorbed pentane (49 Å^2) and hexane (56 Å^2) providing support for the conclusion that the ultimate conversion of the surface reaction is limited by the size of the reactant molecule at the interface. Steric effects have been reported previously to influence both the rate and ultimate yield of reactions on functional SAMs.[47,48]

3.4. Conclusions

High-quality azide functional germanium substrates have been prepared by self-assembly of a 11-bromoundecyltrichlorosilane monolayer from a mixed solvent onto substrates activated by a combination of wet and dry chemical methods, the latter involving a mild UV-ozone oxidation. Azide functionality was introduced by nucleophilic substitution of the terminal bromine upon addition of sodium azide. Thicknesses determined by ellipsometry and X-ray photoelectron spectroscopy were in good agreement with the thickness calculated from a molecular model assuming an extended hydrocarbon chain oriented normal to the surface, indicating that a dense monolayer is formed. The kinetics of a model CuAAC reaction with 5-chloro-pentyne were successfully followed by time resolved *in situ* ATR-IR measurements and demonstrated the initial first order dependence on azide concentration, expected from the reaction mechanism. When the surface concentrations of azide and triazole are similar, an apparent second order dependence on azide concentration is observed, consistent with the theoretical prediction of Oyama *et al*. The azide-functional germanium substrates

described herein are a versatile platform for the fabrication of IR-based sensors or for the characterization of interfacial click reactions that are of growing interest in surface grafting applications.

References

(1) Bhushan, B.; Kulkarni, A. V.; Koinkar, V. N.; Boehm, M.; Odoni, L.; Martelet, C.; Belin, M. *Langmuir* **1995,** *11,* 3189.

(2) Maboudian, R. *Surf. Sci. Rep.* **1998,** *30,* 209.

(3) Rehák, M.; Snejdárková, M.; Otto, M. *Biosens. Bioelectron.* **1994,** *9,* 337.

(4) Rickert, J.; Weiss, T.; Kraas, W.; Jung, G.; Göpel, W. *Biosens. Bioelectron.* **1996,** *11,* 591.

(5) Haneda, R.; Nishihara, H.; Aramaki, K. *J. Electrochem. Soc.* **1997,** *144,* 1215.

(6) Laibinis, P. E.; Whitesides, G. M. *J. Am. Che. Soc.* **1992,** *114,* 9022.

(7) Zamborini, F. P.; Crooks, R. M. *Langmuir* **1998,** *14,* 3279.

(8) Bard, A.; Berggren, K. K.; Wilbur, J. L.; Gillaspy, J. D.; Rolston, S. L.; McClelland, J. J.; Phillips, W. D.; Prentiss, M.; Whitesides, G. M. *J. Vac. Sc. Technol. B* **1997,** *15,* 1805.

(9) Lercel, M. J.; Craighead, H. G. *Appl. Phy. Lett.* **1996,** *68,* 1504.

(10) Pan, M.; Yun, M.; Kozicki, M. N.; Whidden, T. K. *Superlattices Microstruct.* **1996,** *20,* 369.

(11) Rezania, A.; Johnson, R.; Lefkow, A. R.; Healy, K. E. *Langmuir* **1999,** *15,* 6931.

(12) Seo, T. S.; Bai, X. P.; Ruparel, H.; Li, Z. M.; Turro, N. J.; Ju, J. Y. *Proc. Natl. Acad. Sci. U. S. A.* **2004,** *101,* 5488.

(13) Vouć, M.; Goormaghtigh, E.; Homble, F.; Marchand-Brynaert, J.; Conti, J.; Devouge, S.; De Coninck, J. *Langmuir* **2006,** *23,* 949.

(14) Chechik, V.; Crooks, R. M.; Stirling, C. J. M. *Adv. Mater.* **2000,** *12,* 1161.

(15) Mirabella, F. M. Jr. *Practical Spectroscopy Series;Internal reflection spectroscopy: Theory and applications*; Marcel Dekker, Inc.: New York, 1993.

(16) Loring, J. S.; Land, D. P. *Appl. Opt.* **1998**, *37,* 3515.

(17) Lummerstorfer, T.; Hoffmann, H. *J. Phys. Chem. B* **2004,** *108,* 3963.

(18) Laibinis, P. E.; Whitesides, G. M.; Allara, D. L.; Tao, Y. T.; Parikh, A. N.; Nuzzo, R. G. *J. Am. Chem. Soc.* **1991,** *113,* 7152.

(19) Collman, J. P.; Devaraj, N. K.; Chidsey, C. E. D. *Langmuir* **2004,** *20,* 1051.

(20) Zirbs, R.; Kienberger, F.; Hinterdorfer, P.; Binder, W. H. *Langmuir* **2005,** *21,* 8414.

(21) Auner, N.; Weis, J. *Organosilicon Chemistry II, from Molecules to Materials*; VCH: Weinheim, 1996.

(22) Mittal, K. L. *Silanes and other Coupling Agents*; VSP: Utrecht, 1992.

(23) Patai, S. R., Z., *The Chemistry of Organic Silicon Compounds*. John Wiley: Chichester, 1989.

(24) Kolb, H. C.; Finn, M. G.; Sharpless, K. B. *Angew. Chem. Int. Edit.* **2001,** *40,* 2004.

(25) Li, H.; Cheng, F.; Duft, A. M.; Adronov, A. *J. Am. Chem. Soc.* **2005,** *127,* 14518.

(26) Valyocsik, E. W. *J. Electrochem. Soc.* **1967,** *114,* 176.

(27) Brzoska, J. B.; Benazouz, I.; Rondelez, F. *Langmuir* **1994,** *10,* 4367.

(28) Davidovits, J. V.; Pho, V.; Silberzan, P.; Goldmann, M. *Surf. Sci.* **1996,** *352-354,* 369.

(29) Semal, S.; Vouć, M.; de Ruijter, M. J.; Dehuit, J.; De Coninck, J. *J. Phys.Chem. B* **1999,** *103,* 4854.

(30) Silberzan, P.; Léger, L.; Ausserré, D.; Benattar, J. J. *Langmuir* **1991,** *7,* 1647.

(31) Vouć, M.; Semal, S.; De Coninck, J. *Langmuir* **1999,** *15,* 7855.

(32) Lee, Y.; Park, K.; Lim, S. *Appl. Surf. Sci.* **2008,** *255,* 3318.

(33) Faucheux, N.; Zahm, J. M.; Bonnet, N.; Legeay, G.; Nagel, M. D. *Biomaterials* **2004,** *25,* 2501.

(34) Fryxell, G. E.; Rieke, P. C.; Wood, L. L.; Engelhard, M. H.; Williford, R. E.; Graff, G. L.; Campbell, A. A.; Wiacek, R. J.; Lee, L.; Halverson, A. *Langmuir* **1996,** *12,* 5064.

(35) Heise, A.; Stamm, M.; Rauscher, M.; Duschner, H.; Menzel, H. *Thin Solid Films* **1998,** *327-329,* 199.

(36) Andrade, J. D. *Surface and Interfacial Aspects of Biomedical Polymers*; Plenum Press: New York, 1985.

(37) Bergerson, W. F.; Mulder, J. A.; Hsung, R. P.; Zhu, X. Y. *J. Am. Chem. Soc.* **1998,** *121,* 454.

(38) He, J.; Lu, Z.-H.; Mitchell, S. A.; Wayner, D. D. M. *J. Am. Chem. Soc.* **1998,** *120,* 2660.

(39) Lee, K.; Pan, F.; Carroll, G. T.; Turro, N. J.; Koberstein, J. T. *Langmuir* **2004,** *20,* 1812.

(40) Laibinis, P. E.; Graham, R. L.; Biebuyck, H. A.; Whitesides, G. M. *Science* **1991,** *254,* 981.

(41) Nakayama, H.; Nakanishi, J.; Shimizu, T.; Yoshino, Y.; Iwai, H.; Kaneko, S.; Horiike, Y.; Yamaguchi, K. *Colloid Surface B.* **2010,** *76,* 88.

(42) Rodionov, V. O.; Fokin, V. V.; Finn, M. G. *Angew. Chem. Int. Edit.* **2005,** *44,* 2210.

(43) Lewis, W. G.; Magallon, F. G.; Fokin, V. V.; Finn, M. G. *J. Am. Chem. Soc.* **2004,** *126,* 9152.

(44) Fredrickson, G. H.; Milner, S. T. *Macromolecules* **1996**, *29,* 7386.

(45) Oyama, H. T.; Ougizawa, T.; Inoue, T.; Weber, M.; Tamaru, K. *Macromolecules* **2001**, *34,* 7017.

(46) McClellan, A. L.; Harnsberger, H. F. *J. Colloid Interface Sci.* **1967,** *23,* 577.

(47) Houseman, B. T.; Mrksich, M. *Angew. Chem. Int. Edit.* **1999,** *38,* 782.

(48) Templeton, A. C.; Hostetler, M. J.; Kraft, C. T.; Murray, R. W. *J. Am. Chem. Soc.* **1998,** *120,* 1906.

Chapter 4. Controlling the 'click' Functionality on Solid Surfaces

4.1 Controlling Alkyne Functional Groups on the Surface

4.1.1 Background

Self-assembled monolayers (SAMs) have become the material of choice to provide reactive functionality on inorganic surfaces. Functional SAMs comprise short heterobifunctional molecules with a sticky foot on one end, selected to bond to the inorganic substrate, and a reactive functional group of interest on the other end. The two functional groups are joined by a spacer, typically a short chain hydrocarbon, to impart important in-plane interactions that drive the self-assembly process. During self-assembly, the sticky feet migrate to the inorganic surface thus orienting the reactive functional groups to the air interface. Functional SAMs have been formed on flat substrates as well as nanoparticles and serve as a versatile platform through which a wide variety of organic molecules have been covalently tethered to inorganic surfaces. The ability to tether organic molecules to inorganic surfaces has in turn enabled a wide range of applications ranging from directed cell growth[1] to chemical separations[2] to DNA sequencing,[3] and has enabled the fabrication of a myriad of important devices such as biosensors,[4,5] transistors,[6] drug delivery vehicles,[7] and extraction devices.[8]

Because manipulation of the areal density of the surface tethered molecules is of critical importance to many of these applications, the control of areal density of functional groups in SAMs has become a topic of considerable interest. The most popular

method for controlling surface areal density of reactive functional groups has been the use of mixed monolayers comprising a fraction of the functional heterobifunctional molecule and a fraction of a chemically similar monofunctional molecule that lacks the reactive functional group. In the case of flat gold substrates, the areal density of reactive functional groups has been controlled by changing the ratio of monofunctional and heterobifunctional thiols in the mixed monolayer.[7-10] Mixed thiol SAMs have also been used to functionalize lead sulfide[11] and silver[9] and mixed silane SAMs have been used to functionalize the surfaces of mica,[12] silica,[13,14] alumina,[6] and quartz.[4]

While mixed monolayer SAMs have been employed extensively to control surface areal density of reactive functional groups on inorganic substrates, even the most seemingly compatible pair of monofunctional and heterobifunctional molecules can segregate upon self-assembly leading to phase separation of the two components.[15] Indeed, several studies have shown complete phase separation in mixed SAMs.[14,16] Mixed SAMs based on disulfides and unsymmetrical sulfides[17] have been developed to minimize phase separation, however, it has sometimes proven difficult to detect phase separation in mixed SAMs.

A variety of spectroscopic methods have been employed to characterize the homogeneity of mixed SAMs formed on flat substrates, including microscopy,[18] infrared spectroscopy,[7] and nuclear magnetic resonance.[19] The success of these methods depends on the existence of some spectroscopic label that distinguishes the two molecules comprising the mixed SAM. Contact angle analysis has been applied to examine compositional uniformity at the surface, but this is an indirect method that reflects a variety of surface properties beyond surface composition and is limited to select

moieties.[20] The manifestation of phase separation can also be detected by optical microscopy if appropriate dyes are available that can bond to the reactive functional groups in the mixed SAM. The resolution of microscopic techniques is limited to micron length scales associated with the wavelength of light used as well as the size of the reactive dye, which can be considerable for typical visible and fluorescent dye molecules.

Preferential surface adsorption is a second phenomenon that can compromise the applicability of mixed monolayers. In this case, the composition of the monolayer is not the same as the composition of the solution used for deposition, necessitating the construction of calibration curves (i.e., adsorption isotherms) to achieve quantitative functionalization of surfaces. Preferential surface adsorption of one compound in mixed silane monolayers on silica was attributed to differences in absorption rates and solvent effects.[14] Infrared spectroscopy (IR) was used to document preferential surface adsorption in mixed thiol monolayers formed on gold substrates. The relative concentration of the two thiols determined by IR showed a nonlinear dependence on the concentration of the deposition solution. Preferential adsorption in the latter case was attributed to differential salvation effects.[21]

In recent years, the copper catalyzed alkyne-azide click reaction has emerged as a gold standard for surface modification applications due to its remarkable chemoselectivity, the ease with which surfaces can be functionalized with alkyne or azide groups and the high conversion of this click reaction. A variety of flat and nanoparticle substrates have subsequently been functionalized with azide and alkyne groups by our own [22-27] and other research groups.[28-34] However, only a few of these investigations have employed mixed monolayers to control the areal density of surface functional

groups,[3,6,9,10,17,35] and none of these studies have established that the SAMs were homogeneous.

In this Chapter, we study in detail the use of SAMs formed from mixtures of alkyne-silanes and alkane-silanes to control the areal density of reactive alkyne groups on the surface of flat germanium substrates and silicon wafers. We describe a new analytical tool that we have developed to characterize the mixed SAMs: an infrared spectroscopy (IR) technique to detect preferential surface adsorption. The IR method is based on the use of attenuated total reflectance infrared spectroscopy (ATR-IR) to monitor click reactions between azide compounds with infrared "labels" and alkyne-functional SAMs deposited on germanium ATR plates. Combined with results from a thermogravimetric analysis (TGA) technique on nanoparticles (conducted by Yanir Maidenberg and not described in the thesis), we find that these mixed silane monolayers show neither phase separation nor preferential surface. Monolayers prepared from mixtures of alkyne-silanes and alkane-silanes therefore provide a versatile platform for controlling alkyne 'click' functionality on a variety of materials ranging from flat substrates to nanoparticles.

4.1.2 Experimental Section

4.1.2.1 Silanization of Silica Wafers

Silicon wafers were cut into 1cm squares, washed progressively with toluene, acetone, and water and subsequently placed in a UV-ozone cleaning system for 30 minutes to remove residual surfactants. Cleaned and dried wafers were placed in a 20mL scintillation vial and flushed with nitrogen. Finally, a solution of O-(propargyloxy)-N-

triethoxysilylpropyl-carbamate (OTPC) (10μL) and triethoxysilypropylethyl-carbamate (TPC) (10μL) dissolved in 20mL anhydrous toluene was added to the vial and the wafer was left to react for 1.5 hours at 80 ℃. The wafer was then washed extensively with toluene to remove physisorbed silanes. Afterwards, the thickness of mixed silane monolayers was measured by ellipsometry .

4.1.2.2 Imaging the Mixed SAMs Morphology by Reaction with Fluorescent Dye (tetramethylrhodamine-5-carbonyl azide: TMRCA)

Three silicon wafers functionalized with 50% OTPC mixed SAMs (prepared in 4.1.2.1) reacted with 20mL solution of TMRCA (0.2%wt), catalyst CuBr in DMF in a 50mL Erlenmeyer flask in order to image the spatial distribution of surface alkyne groups. The flask was shielded from light and the solution was held under nitrogen for 24 hours after which the dye-functionalized surface was washed with copious amounts of DMF and water. The success of the reaction was confirmed by an increase in thickness measured by ellipsometry. The fluorescent activity of the dye was analyzed using 2-photon microscopy (Leica TCS SP5 Wetzlar, Germany). The correlation function between regions of dye labeling was calculated from the microscope image using ImageJ software in order to examine the randomness of the spatial distribution of surface-tethered fluorescent dye.

4.1.2.3 Cleaning and Activation of Ge Surface

The methods used for cleaning and silanization of the germanium (Ge) substrates (i.e., crystals for attenuated total reflectance infrared spectroscopy) were reported previously.[24] The Ge surface was degreased by sonicating in acetone, methanol and DI water for 5 min. And then the surface was dried with N_2 and exposed to UV-ozone under ambient conditions for 15 min. Finally the surface was abundantly rinsed with DI water and dried under nitrogen flux.

4.1.2.4 Silanization of Ge Surface

The activated Ge surface was immersed in a solution of a desired ratio of OTPC/TPC (1:0, 1:1, 3:1, 1:3, v:v) (total 20 μl) in anhydrous toluene (20 ml) in a glass vial and covered with aluminum foil to exclude light. The reaction mixture was left to react overnight at 80 ℃ under nitrogen protection. Afterwards, the Ge substrate was sonicated in toluene, gently scrubbed with a toluene-soaked tissue to assist in removal of possible physisorbed multilayers, and rinsed with toluene. Finally, the surface was dried under nitrogen flux.

4.1.2.5 Synthesis of Azidoacetonitrile

A suspension of bromoacetonitrile (5.3g) in water (9mL) was prepared and stirred vigorously. Sodium azide (5.2g) was added and the reaction was heated to 85 ℃ for 2.5 hours during which the suspension turned black. After the mixture was cooled to room temperature it was added to 5mL ethyl acetate and the organic layer was separated. 5mL

ethyl acetate was added to the remaining aqueous layer and shaken. The organic layer was once more separated into the same vial as the first extraction. The combined extract was vacuum dried at room temperature to remove the ethyl acetate giving 4mL of azidoacetonitrile. The compound was characterized by infrared spectroscopy. This procedure was slightly modified from another described elsewhere.[36]

Molecular modeling of azidoacetonitrile was carried out using SPARTAN 10 (Wavefunction, Inc.). After energy minimization, the molecule appeared to be cylindrical in shape and the projected area of its reactive face was about 0.2 nm^2.

4.1.2.6 Click Reaction of Silanized Ge Crystal with Azidoacetonitrile

As shown in Figure 4.1.1, the silanized Ge surface was immersed in a solution of azidoacetonitrile (100 µl), $CuSO_4\,5H_20$ (20 mg, 0.08 mmol) and sodium ascorbate (33.6 mg, 0.16 mmol), dissolved in a co-solvent of DMF (20 ml) and H_2O (200 µl) overnight. Afterwards, the Ge surface was washed with a copious amount of water to remove the excess catalyst, followed by rinsing with toluene to remove any residuals of the reactant solution, and was finally dried under nitrogen flux.

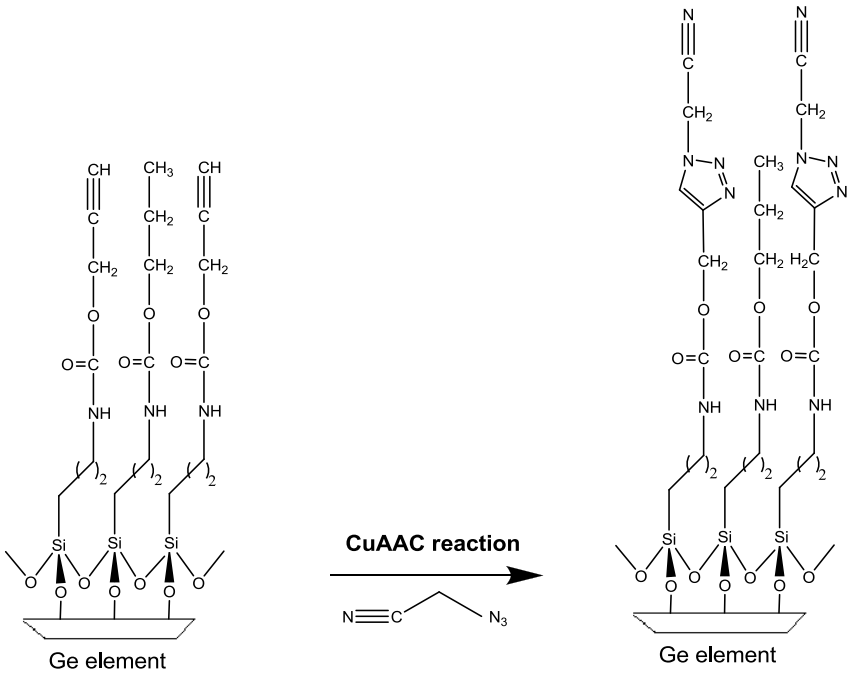

Figure 4.1.1. Scheme for the modification of Ge surface.

4.1.2.7 Surface Characterization

Infrared spectra for Ge surface were obtained with a Nicolet 560 FTIR (MCT/A detector, broad range 4000-650 cm^{-1}, liquid N_2 cooled), coupled with an ATR accessory (Horizon™, Harrick Scientific Products Inc.) at a resolution of 4 cm^{-1} with an aperture of 100. The internal reflection element was a 50x10x2 mm trapezoidal Ge crystal with an aperture angle of 45 ° yielding 13 internal reflections. After each step of experiments, the modified Ge surface was characterized by ATR-IR. Such process was repeated three times to quantify the desired modification.

Noncontact mode AFM measurements using the AutoProbe CP Research Probe head (Veeco Instrument) were performed to study the topography of the mixed SAMs.

Silicon cantilevers (dLeversTM) with a spring constant of 2.2 N/m were employed and the analysis was carried out under air-ambient condition.

4.1.3 Results and Discussion

4.1.3.1 AFM

Atomic force microscopy (AFM) results (see Figure 4.1.2) demonstrate that the mixed SAMs on Ge are smooth (RMS roughness is less than 0.6nm) and featureless, which confirms that the modified substrates are sufficiently smooth to permit surface characterization by ellipsometry, angle-dependent x-ray photoelectron spectroscopy (ADXPS) analyses.

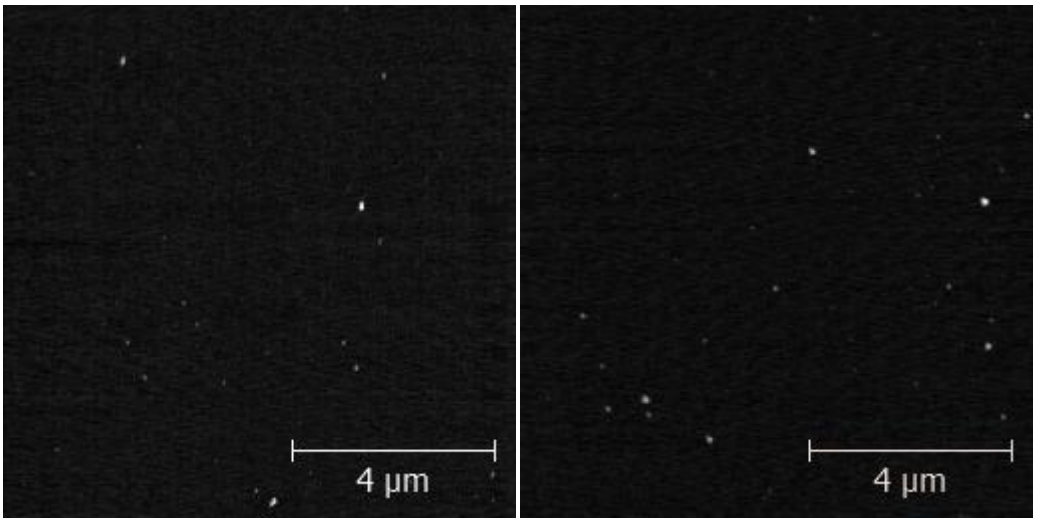

Figure 4.1.2. 10 µm×10 µm AFM images of Ge substrates for 50% alkyne functionality (left) and 100% alkyne functionality (right).

4.1.3.2 Ellipsometry and ADXPS results

As shown in Table 4.1.1, the XPS-derived thickness,[27] agrees well with the ellipsometric thickness for different kinds of mixed SAMs.

Table 4.1.1. Thicknesses of mixed SAMs on Ge surface.

Percentage alkyne on Ge surface (%)	Ellipsometric thickness (nm)	ADXPS thickness (nm)
0	1.15 ±0.10	1.17
25	1.17 ±0.10	1.18
50	1.17 ±0.10	1.18
75	1.16 ±0.10	1.17
100	1.20 ±0.10	1.20

4.1.3.3 ATR-IR Results

A new infrared spectroscopy technique was developed to test for preferential surface adsorption in the mixed monolayers comprising alkyne-silanes and alkane-silanes. The basis of the method is titration of surface alkyne groups by reaction with an azide-functional molecule containing an infrared-active label. In the absence of preferential surface adsorption, the absorbance of the infrared label, determined by attenuated total reflectance spectroscopy (ATR-IR) measurements for SAMs formed on germanium ATR plates, will be linearly dependent on the fraction of alkyne-silanes in the solution used for silane deposition, provided that all alkyne groups are accessible for reaction. Satisfying

the later caveat requires that the footprint of the azide-label molecule be smaller than the area per silane molecule so as to avoid steric hindrance. The number of molecules per unit area in a SAM is determined from the relation.

$$\sigma = \frac{N_A \, d \, \rho}{M} \tag{4.1.1}$$

where d is the layer thickness, ρ is the density of the molecule with molecular weight of silane, and N_A is Avogadro's number. In the case of the alkyne-silane monolayer, ellipsometry measurements yield d=1.2 nm and its density is 1.0 g/cm^3, leading to an areal density of 3 silanes per nm^2, or an area of 0.33 nm^2 per silane molecule. Azidoacetonitrile (AzAN) is an appropriate azide molecule with a projected area smaller than this value as well as an infrared-active nitrile group. The nitrile group has strong absorption bands in the windowpane region of the IR spectrum at 2100 cm^{-1} and 2250 cm^{-1} and the projected area of AzAN determined by molecular modeling is about 0.2 nm^2. The nitrile absorbance will scale linearly with the concentration of alkyne in the deposition solution if there is no preferential surface adsorption.

The ATR-IR spectra for a mixed monolayer before and after reaction with AzAN are shown in Figure 4.1.3. The expanded region of interest spectra shown at right in the figure illustrate that the alkyne band disappears and the nitrile bands appear after reaction with AzAN. Complete disappearance of the alkyne band confirms that the projected area of the AzAN is small enough to allow for the click reaction to go to completion with no residual alkyne remaining.

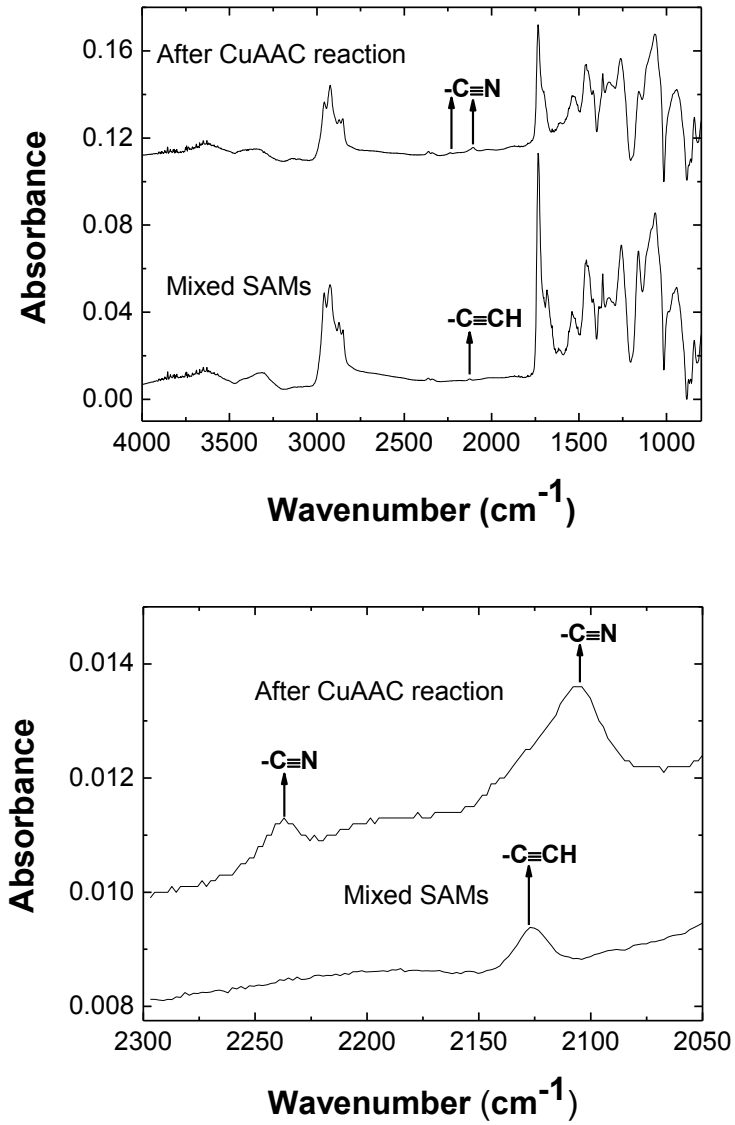

Figure 4.1.3. ATR-IR spectra for mixed SAMs formed on germanium substrates before (lower spectra) and after (upper spectra) reaction with azidoacetonitrile. The arrows on the spectra indicate the locations of the alkyne and nitrile absorbance bands.

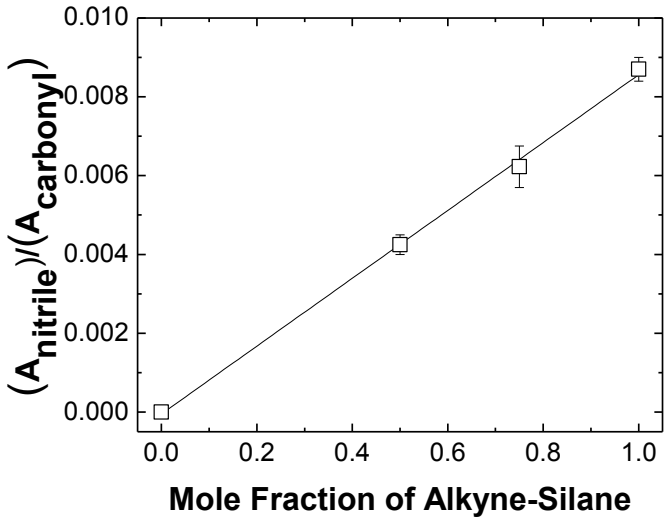

Figure 4.1.4. Normalized nitrile absorbance as a function of the fraction of alkyne-silane in the mixed monolayer. The absorbance is normalized by the absorbance of the carbonyl group, an internal standard, residing within the silane SAM.

Assuming that Beer's law applies, the absorbance of the nitrile band can be taken as indicative of the areal density of surface alkyne groups. For quantitative analysis, the absorbance of the nitrile band is normalized to the absorbance of an internal standard, the carbonyl band emanating from the underlying SAM. The normalized nitrile absorbance is linearly dependent on the fraction of alkyne-silane, as shown in Figure 4.1.4, indicating that there is no preferential adsorption in the mixed silane SAM on germanium.

4.1.3.4 Fluorescence Microscopy

The micron scale homogeneity of the mixed monolayers was next examined by applying the fluorescent dye labeling technique described in Figure 4.1.5. Mixed monolayers formed on silicon wafers were reacted with an azide functional fluorescent

dye, TMRCA. The thickness of the 50%-alkyne mixed monolayer grafted to a Si wafer surface was determined by ellipsometry to be 1.10±07nm. After the tethering of the dye, the thickness increased to 22.4±3.3nm. If the alkyne silanes are randomly distributed, as depicted in the lower part of the Figure 4.1.5, fluorescent dyes tethered to surface alkyne groups will also be randomly distributed. If phase separation is manifest in the mixed SAM, however, as depicted in the upper part of the Figure 4.1.5, the spatial distribution of surface-tethered dyes will reflect the phase separated morphology of the alkyne silanes in the SAM.

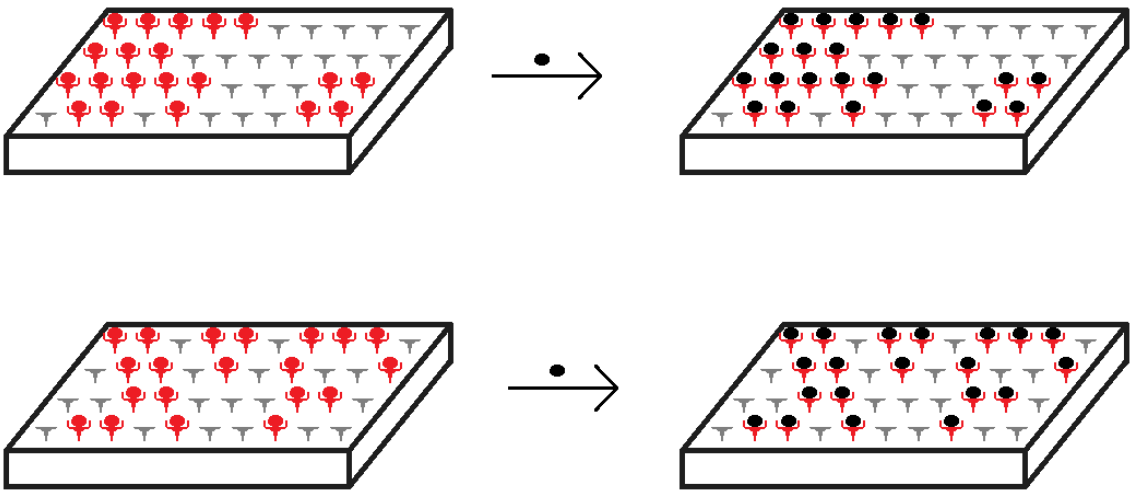

Figure 4.1.5. Possible morphologies for mixed monolayers of alkyne-terminated and alkane-terminated silanes. A reactive azide-functionalized fluorescent dye is coupled to the alkyne silanes to image the spatial distribution of alkyne groups in the monolayer. Upper figure: alkyne-silanes phase separate at the surface. Lower figure: alkyne-silanes in the mixed monolayer are randomly distributed.

Figure 4.1.6 shows the fluorescent microscopy image of a mixed monolayer comprising 50% alkyne-silane formed on a silicon wafer where the distribution of surface

alkyne groups has been imaged by reaction with TMRCA. The reason that half of the image does not appear white even though half of the surface is covered with alkyne silanes, is that in many regions the two different silanes are well mixed at distances below the resolution of the microscope. Evidence for phase separation is not apparent in the micrograph; however, the spatial distribution of dye was characterized by correlation function analysis to provide a more quantitative assessment as shown in Figure 4.1.6.

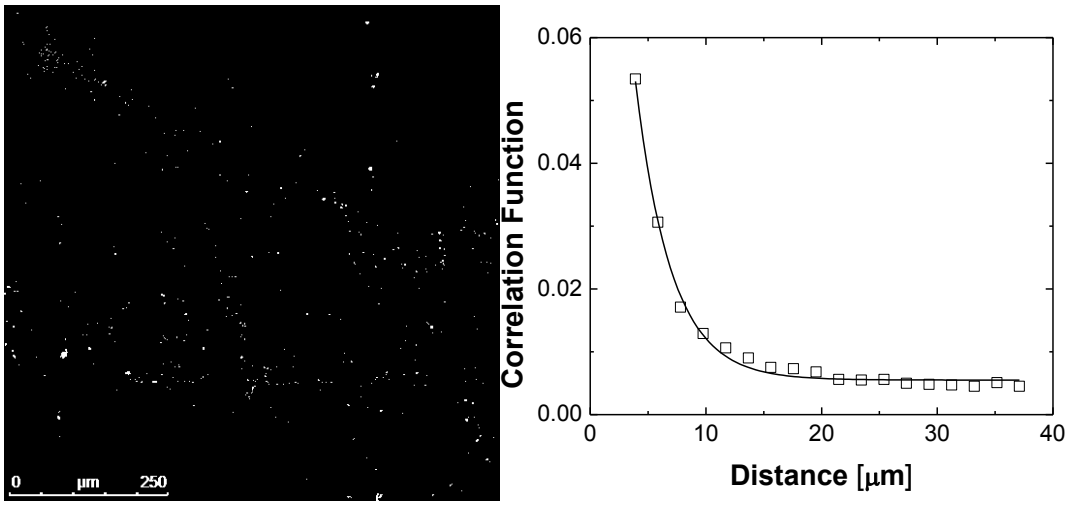

Figure 4.1.6. Two-photon fluorescence microscopy image (left) of the surface of a silicon wafer functionalized with a 50%:50% mixture of alkyne-silane and alkane-silane. The location of surface alkyne groups has been imaged by reaction with an azide-functionalized fluorescent dye. The graph at right shows the autocorrelation function determined from the image and a fit to the exponential functional expected for a random distribution of alkyne-silanes.

The correlation function corresponds well to an exponential function indicating that the dye molecules, as well as the underlying alkyne-silane molecules, are randomly distributed across the surface.[37] This analysis allows us to conclude that, within the micron scale resolution of the fluorescence microscopy technique, the surface-tethered

dye molecules and the underlying alkyne-silanes do not phase separate from the alkane-silanes when applied to the surface of a silicon wafer.

4.1.4 Conclusions

We reported a method for quantitative control of the surface areal density of alkyne reactive groups on hard substrates. The method is based on mixed SAMs containing a portion of the functional alkyne silane and a fraction of a chemically similar monofunctional alkane silane that lacks the reactive functional group. A new analytical tool, ATR-IR, is developed to characterize the functionality on the surface by investigating click reactions between azide compounds with infrared labeled nitrile groups and alkyne-functional SAMs deposited on germanium ATR plates. And no preferential absorption of either compound was discovered on the surface. Combined with fluorescence microscopy result by reacting mixed SAMs with an azide functional fluorescent dye, it is concluded that the functional and non-functional groups roughly distributes randomly by correlation function analysis on a flat surface.

References

(1) Furuya, S.; Makino, A.; Hirabayashi, Y. *Brain Res. Protoc.* **1998**, *3*, 192.

(2) Wirth, M. J.; Fairbank, R. W. P.; Fatunmbi, H. O. *Science* **1997**, *275*, 44.

(3) Zheng, M.; Huang, X. Y. *J. Am. Chem. Soc.* **2004**, *126*, 12047.

(4) Deng, T.; Li, J. S.; Huan, S. Y.; Yang, H. F.; Wang, H.; Shen, G. L.; Yu, R. Q. *Biosens. Bioelectron.* **2006**, *21*, 1545.

(5) Rickert, J.; Gopel, W.; Beck, W.; Jung, G.; Heiduschka, P. *Biosens. Bioelectron.* **1996**, *11*, 757.

(6) Bjorklund, N.; Pettersson, F. S.; Tobjork, D.; Osterbacka, R. *Synth. Met.* **2011**, *161*, 743.

(7) Bertilsson, L.; Liedberg, B. *Langmuir* **1993**, *9*, 141.

(8) Vanderpuije, B. N. Y.; Han, G.; Rotello, V. M.; Vachet, R. W. *Anal. Chem.* **2006**, *78*, 5491.

(9) Laibinis, P. E.; Fox, M. A.; Folkers, J. P.; Whitesides, G. M. *Langmuir* **1991**, *7*, 3167.

(10) Subramanian, A.; Irudayaraj, J.; Ryan, T. *Sens. Actuator B-Chem.* **2006**, *114*, 192.

(11) Yang, J. P.; Fendler, J. H. *J. Phys. Chem.* **1995**, *99*, 5505.

(12) Yoon, R. H.; Ravishankar, S. A. *J. Colloid Interface Sci.* **1996**, *179*, 391.

(13) Offord, D. A.; Griffin, J. H. *Langmuir* **1993**, *9*, 3015.

(14) Tong, Y. J.; Tyrode, E.; Osawa, M.; Yoshida, N.; Watanabe, T.; Nakajima, A.; Ye, S. *Langmuir* **2011**, *27*, 5420.

(15) Stranick, S. J.; Parikh, A. N.; Tao, Y. T.; Allara, D. L.; Weiss, P. S. *J. Phys. Chem.* **1994**, *98*, 7636.

(16) Heise, A.; Stamm, M.; Rauscher, M.; Duschner, H.; Menzel, H. *Thin Solid Films* **1998**, *327*, 199.

(17) Noh, J.; Hara, M. *Langmuir* **2000**, *16*, 2045.

(18) Jackson, A. M.; Hu, Y.; Silva, P. J.; Stellacci, F. *J. Am. Chem. Soc.* **2006**, *128*, 11135.

(19) Fatunmbi, H. O.; Bruch, M. D.; Wirth, M. J. *Anal. Chem.* **1993**, *65*, 2048.

(20) Silberzan, P.; Leger, L.; Ausserre, D.; Benattar, J. J. *Langmuir* **1991**, *7*, 1647.

(21) Hudalla, G. A.; Murphy, W. L. *Langmuir* **2009**, *25*, 5737.

(22) Dach, B. I.; Rengifo, H. R.; Turro, N. J.; Koberstein, J. T. *Macromolecules* **2010**, *43*, 6549.

(23) Rengifo, H. R.; Chen, L.; Grigoras, C.; Ju, J. Y.; Koberstein, J. T. *Langmuir* **2008**, *24*, 7450.

(24) Rengifo, H. R.; Grigoras, C.; Dach, B. I.; Li, X.; Turro, N. J.; Lee, H. J.; Wu, W. L.; Koberstein, J. T. *Macromolecules* **2012**, *45*, 3866.

(25) White, M. A.; Johnson, J. A.; Koberstein, J. T.; Turro, N. J. *J. Am. Chem. Soc.* **2007**, *129*, 4504.

(26) White, M. A.; Maliakal, A.; Turro, N. J.; Koberstein, J. *Macromol. Rapid Commun.* **2008**, *29*, 1544.

(27) Zhang, S.; Koberstem, J. T. *Langmuir* **2012**, *28*, 486.

(28) Brennan, J. L.; Hatzakis, N. S.; Tshikhudo, T. R.; Dirvianskyte, N.; Razumas, V.; Patkar, S.; Vind, J.; Svendsen, A.; Nolte, R. J. M.; Rowan, A. E.; Brust, M. *Bioconjugate Chem.* **2006**, *17*, 1373.

(29) Feng, L. B.; Wang, Y. L.; Wang, N.; Ma, Y. X. *Polym. Bull.* **2009**, *63*, 313.

(30) Kar, M.; Vijayakumar, P. S.; Prasad, B. L. V.; Sen Gupta, S. *Langmuir* **2010**, *26*, 5772.

(31) Lummerstorfer, T.; Hoffmann, H. *J. Phys. Chem. B* **2004**, *108*, 3963.

(32) Prakash, S.; Long, T. M.; Selby, J. C.; Moore, J. S.; Shannon, M. A. *Anal. Chem.* **2007**, *79*, 1661.

(33) Timofte, R. S.; Titman, J. J.; Shao, L. M.; Stephens, J. C.; Woodward, S. *Tetrahedron* **2005**, *61*, 51.

(34) Wang, Y. P.; Chen, J. C.; Xiang, J. M.; Li, H. J.; Shen, Y. Q.; Gao, X. G.; Liang, Y. *React. Funct. Polym.* **2009**, *69*, 393.

(35) Bain, C. D. W., G.M. *J. Am. Chem. Soc.* **1988**, *110*, 6560.

(36) Vereshchagin, L. I.; Kizhnyaev, V. N.; Verkhozina, O. N.; Proidakov, A. G.; Smirnov, A. I. *Russ. J. Organ. Chem.* **2004**, *40*, 1156.

(37) Debye, P.; Anderson, H. R.; Brumberger, H. *J. Appl. Phys.* **1957**, *28*, 679.

4.2 Controlling Azide Functional Groups on Solid Surfaces

4.2.1 Background

Some researchers have prepared mixed SAMs containing a fraction of a functionalized molecule (with Br end group) and a fraction of a non-functionalized molecule (with methyl end group) on flat surfaces by immersing surfaces into a solution containing different ratio of the two compounds, such as thiols on gold surface[1] and silanes on silicon surface.[2] While this has traditionally been the most common method to fabricate mixed monolayers, Stranick *et al*.[3] have shown that even the most compatible pair of monolayers segregates into two domains on the surface to a varying degree. Indeed, Heise *et al*. discovered the Br terminated silane is preferentially adsorbed from the solution.[2] Several other studies[3,4] have shown complete domain separation when two monolayers were mixed and much effort must be invested in ascertaining true mixing, especially when functionalizing nanoparticle surface. In our work, an alkyne end-functional labeled fluorescent dye was reacted to mixed SAMs comprising of azide functional group and methyl non-functional group (ratio 1:1) deposited on silicon wafers prepared in the same procedure described in Chapter 4.1, and aggregation of dye was observed indicating phase separation of mixed monolayers, as shown in Figure 4.2.1, where the white part is the tethered dye on the silicon surface.

Other methods of fabricating mixed SAMs on surfaces are rare but include use of disulfides and unsymmetrical sulfides,[5] which encounter the same difficulty in evaluating the uniformity of the surface. Others have used microprinting on flat surfaces.[6,7]

Here we describe a new method that circumvents the concerns of true monolayer mixing. Bromine-terminated silanes are used to completely cover the surfaces of flat Ge, which can be partially converted to azide functionality through kinetic control of the S_N2 substitution reaction with sodium azide. The kinetics of interfacial reaction between bromine end-functional SAMs and sodium azide was monitored by attenuated total reflectance infrared spectroscopy (ATR-IR), incorporated within a flow through liquid cell, which has successfully quantified the kinetics of an interfacial click reaction between azide SAMs and an alkyne-functional reactant by our previous work.[8] The azide substitution reaction demonstrated kinetics of a first order dependence after the first 2 minutes, and exhibited a total conversion within 150 minutes, contrary to previously reported results showing complete conversion in 48-60 hours.[2,9] The reaction can easily be quenched by flushing the system with DI water at a desired time to achieve partial conversion of the azide end groups. Our method provides for a universal method for the fabrication of truly-mixed monolayers that has not been previously reported. The significance of the work is thus two-fold: first, it shows that a complete conversion of bromine to azide occurs much faster than previously expected. This drastically shortens synthesis time of ‘click’ functionalized surfaces from days to a few hours. Secondly, and more importantly, the work signifies a method by which surface composition can be tailored on any oxide surface regardless of its identity and curvature and provides for a universal method for the fabrication of truly-mixed monolayers comprising azide and Br, wherein both groups can be easily transformed to other preferable functional groups.

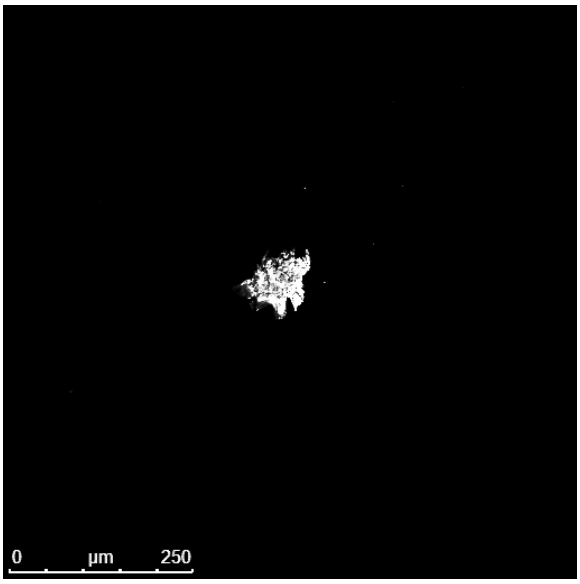

Figure 4.2.1. 2-Photon microscopy image of silicon surface modified by an alkyne fluorescence reacting with mixed SAMs of a 50%/50% (volume ratio) mixture of azide-terminated silane and methyl-terminated silane, showing aggregation of azide-terminated silanes.

4.2.2 Experimental Section

The overall process used to control the areal density of azide groups grafted to Ge crystals for ATR-IR is shown schematically in Figure 4.2.2. Three basic steps are involved: cleaning and activation, silanization and kinetic manipulation of the areal density of azide groups.

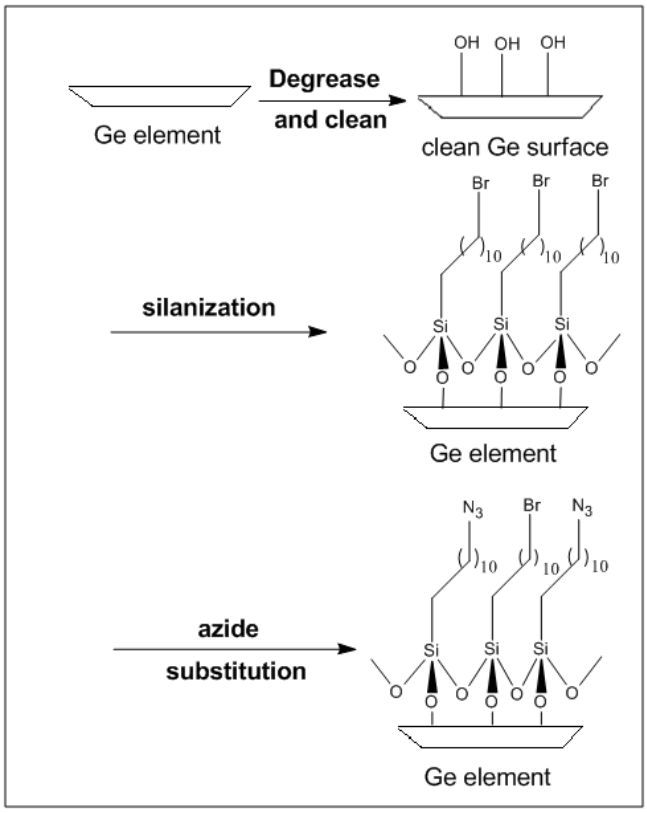

Figure 4.2.2. Scheme for surface modification by partial conversion of S_N2 substitution.

4.2.2.1 Cleaning and Activation

The Ge surface was degreased by sonicating in acetone, methanol and DI water for 5 min. Then the surface was dried with N_2 and exposed to UV-ozone under ambient conditions for 15 min. Finally the surface was abundantly rinsed with DI water and dried under nitrogen flux.

4.2.2.2 Silanization

The activated Ge surface was immersed in a solution of BUTS (0.08% v:v) in a mixture of undecane and carbon tetrachloride (7:3 v:v). Afterwards, the Ge substrate was sonicated in toluene, gently scrubbed with a toluene-soaked tissue to assist in removal of possible physisorbed multilayers, and rinsed with toluene. Finally, the surface was dried under nitrogen flux.

4.2.2.3 ATR-IR Measurement of Azide Substitution

The silanized Ge crystal was placed into a liquid ATR flow cell. A saturated solution of sodium azide in DMF (1mL) was injected into the cell whereupon it contacted the silanized Ge surface to initiate the azide substitution reaction. The reaction was performed at room temperature in the air for 1 day with spectra recorded every 2 minute with 100 scans acquired. Background was collected with the bare Ge crystal. Automatic baseline correction methods were applied to all the spectra. The reaction was stopped by flushing the surface with a lot of DI water for three times and dried under nitrogen flux. Coverage of azide end groups was calculated upon the spectra.

4.2.2.4 Surface Characterization

The progression of surface modifications on Ge surface has been well characterized by our previous work in Chapter 3.

Infrared spectra for Ge surface were obtained with a Nicolet 560 FTIR (MCT/A detector, broad range 4000-650 cm^{-1}, liquid N_2 cooled), coupled with an ATR accessory

(Horizon™, Harrick Scientific Products Inc.) at a resolution of 4 cm^{-1} with an aperture of 100. The internal reflection element was a 50×10×2 mm trapezoidal Ge crystal with an aperture angle of 45 ° yielding 13 internal reflections. The Ge crystal was incorporated within a flow through liquid cell.

The thicknesses of SAMs on Ge surface were measured with a Beaglehole Spectroscopic and imaging ellipsometry (Beaglehole Instruments, Wellington, New Zealand) under angle mode (70 °) with a fixed wavelength of 632.8 nm. The experimental ellipsometry data were analyzed using Film Wizard software.

4.2.3 Results and Discussion

The areal density of bromine silane fully covered Ge surface was calculated by equation:

$$\sigma = \frac{N_A d \rho_{dry}}{M_W} \quad (4.2.1)$$

where d is the ellipsometric layer thickness (1.6 nm), ρ_{dry} is the density of the dry silane coupling agent (assuming a well-packed fully-extended monolayer with a ρ_{dry} of 1.0 g/cm^3), M_W is the molecular weight of the silane (Br-$C_{11}H_{22}$-Si-), and N_A is Avogadro's number. Applying this relation to our data we find an areal density of 3 chains/nm^2 for the bromine-silane monolayer.

4.2.3.1 ATR-IR Results

All the spectra during the azide substitution reaction were treated by subtraction of the spectrum of DMF solvent by adjusting the weighting factor until the contributions of absorbance bands below about 1700 cm^{-1} were completely removed, successfully demonstrated in Chapter 3. The areal density of the azide peak was integrated and converted to conversion compared with the peak area of full conversion. The relation between areal density of azide groups and time is given in Figure 4.2.3.

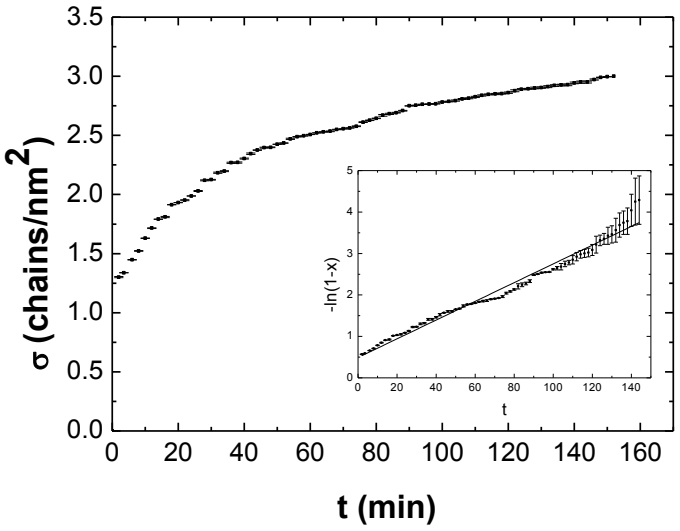

Figure 4.2.3. Kinetics curve of S_N2 substitution of bromine to azide on Ge surface, where σ is the areal density of azide silane on the surface in chains/nm^2, x is the conversion of Br to azide, t is reaction time in minutes.

Most researches show the azide substitution reaction would take 48hours. By monitoring the kinetics of this reaction, we found that it only takes 2.5 h for the reaction to reach completion. In the first 2 minutes, the reaction rate is quite fast with an almost 40% conversion. After this period, the reaction slows down with a first-order dependence

on the surface Br concentration (as shown in the insert of Figure 4.2.3) up to an ultimate conversion of about 100%, and the reaction constant is 0.0226 ± 0.0004 min^{-1}.

In order to construct a mixed monolayer containing the azide functional groups, a method was developed to control the conversion of bromine on the surface. By introducing a solvent (water) that would rinse the reactant (sodium azide) off the surface, we may terminate the reaction at any given time leading to a partially converted surface containing both Br and azide groups. The silanized Ge samples were exposed to a saturated solution of sodium azide in DMF (20 mL), withdrawn from the solution after 1,2,10 and 150 minutes. The surfaces were quickly rinsed with a copious amount of DI water to remove the residual sodium azide, sonicated with toluene and dried under nitrogen flux. Infrared spectra were obtained on the azide modified surfaces with different areal densities, as shown in Figure 4.2.4.

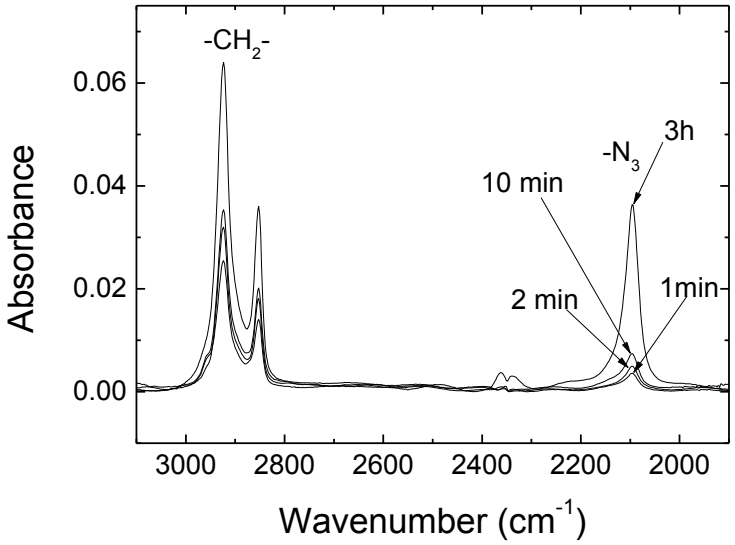

Figure 4.2.4. Infrared Spectra of mixed SAMs comprising various ratios of azide end groups and Br end groups at different quenched reaction time.

The ratio of peak areas of absorbance of CH_2 to N_3 shows a constant increase as a function of reaction time as evidenced in Figure 4.2.4. Table 4.2.1 indicates the surface azide functionality can be tailored by terminating the reaction at a specific time, in good agreement with the results predicted from the kinetics curve in Figure 4.2.3.

Table 4.2.1. Spectra results compared with kinetics curve.

Stopped time (minutes)	CH_2 absorbance peak area	N_3 absorbance peak area	Ratio of peak areas of N_3 to CH_2	Conversion from spectra results	Conversion from kinetics curve
1	1.7547	0.1641	0.094	22.8%	N.A.
2	1.5265	0.2242	0.147	35.6%	43.4%
10	1.3455	0.3035	0.225	54.5%	54.3%
150	3.2841	1.3560	0.413	100%	100%

The ellipsometric thicknesses of mixed SAMs at various conversions, listed in Table 4.2.1, are found to lie within the range of 1.6 ± 0.1 nm to 1.7 ± 0.1 nm, showing uniformity in the mixed SAMs.

4.2.3.2 Fluorescence Microscopy

The micron scale homogeneity of the mixed monolayers was examined by applying the fluorescent dye labeling technique described in Chapter 4.1. The 50% azide

mixed monolayer formed on Ge wafer was reacted with an alkyne end-functional fluorescent dye. The fluorescent microscopy image is presented in Figure 4.2.5, where the green part is the tethered dye on the Ge surface. The reason that half of the image does not appear green even though half of the surface is covered with azide silanes, is that in many regions the two different groups (Br and azide) are well mixed at distances below the resolution of the microscope. Compared with Figure 4.2.1, evidence for the absence of phase aggregation is more obvious, and a more detailed quantitative evaluation of the spatial distribution of dye was provided by correlation function analysis.

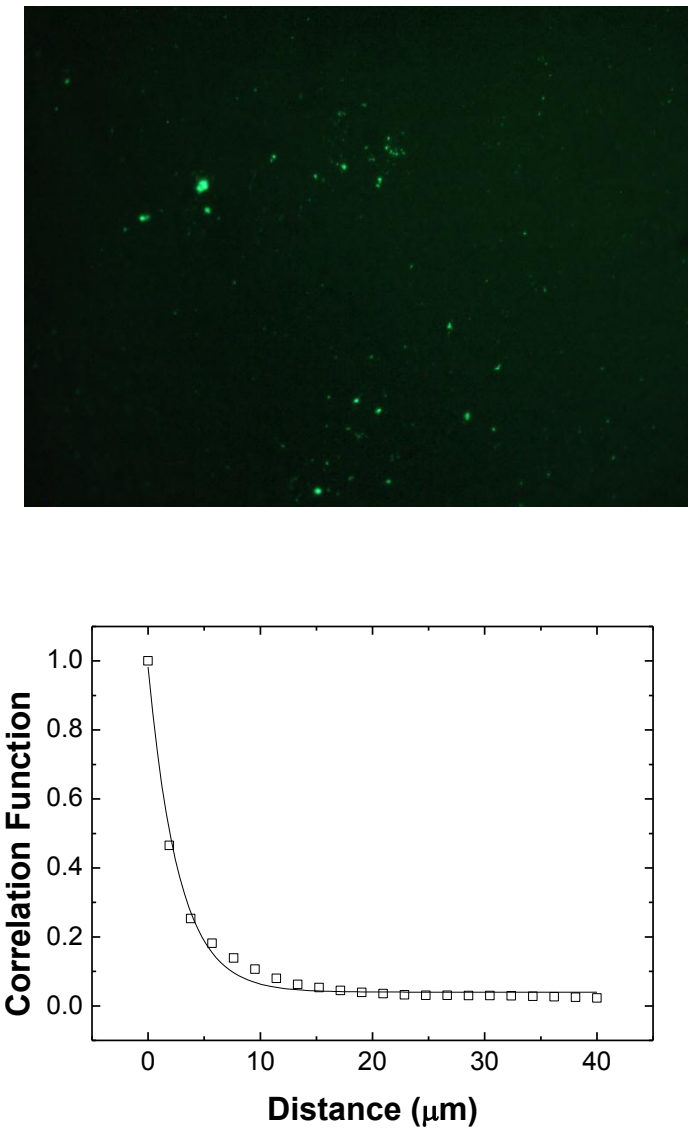

Figure 4.2.5. Upper is fluorescence image of Ge surface modified by alkyne end-functional dye when the S_N2 reaction was stopped at 10 min, showing no aggregation compared with Figure 4.2.1. Lower is the autocorrelation function determined from the image and a fit to the exponential functional expected for a random distribution of azide-silanes.

The autocorrelation function of the image determined by analysis with ImageJ software is presented in the lower figure of Figure 4.2.5. The correlation function fits

well to an exponential function,[10] indicating that the dye molecule is indeed randomly distributed across the surface. This analysis allows us to conclude that, within the micron scale resolution of the fluorescence microscopy technique, the surface-tethered dye molecules and thereby the underlying azide monolayer does not phase separate from the Br monolayer.

4.2.4 Conclusions

We have shown that mixed SAMs with desired azide functionality could be prepared through kinetic control of the azide substitution reaction directly. Time-resolved ATR measurements indicate a first-order dependence on Br concentration after the first 2 minutes until the full conversion. The ease of the method provides a platform to study the kinetics of functional polymers reacting to mixed azide monolayers in Chapter 5.

References

(1) Collman, J. P.; Devaraj, N. K.; Eberspacher, T. P. A.; Chidsey, C. E. D. *Langmuir* **2006**, *22*, 2457.

(2) Heise, A.; Stamm, M.; Rauscher, M.; Duschner, H.; Menzel, H. *Thin Solid Films* **1998**, *327*, 199.

(3) Stranick, S. J.; Parikh, A. N.; Tao, Y. T.; Allara, D. L.; Weiss, P. S. *J. Phys. Chem.* **1994**, *98*, 7636.

(4) Tong, Y. J.; Tyrode, E.; Osawa, M.; Yoshida, N.; Watanabe, T.; Nakajima, A.; Ye, S. *Langmuir* **2011**, *27*, 5420.

(5) Offord, D. A.; Griffin, J. H. *Langmuir* **1993**, *9*, 3015.

(6) Tan, J. L.; Tien, J.; Chen, C. S. *Langmuir* **2002**, *18*, 519.

(7) Tien, J.; Terfort, A.; Whitesides, G. M. *Langmuir* **1997**, *13*, 5349.

(8) Zhang, S.; Koberstem, J. T. *Langmuir* **2012**, *28*, 486.

(9) Fryxell, G. E.; Rieke, P. C.; Wood, L. L.; Engelhard, M. H.; Williford, R. E.; Graff, G. L.; Campbell, A. A.; Wiacek, R. J.; Lee, L.; Halverson, A. *Langmuir* **1996**, *12*, 5064.

(10) Debye, P.; Anderson, H. R.; Brumberger, H. *J. Appl. Phys.* **1957**, *28*, 679.

Chapter 5. Click Reaction Kinetics of Alkyne End-functional Polymers Reacting to Azide Functionalized Solid Substrate

5.1 Background

The reaction of a functional polymer at an interface is an essential aspect of many diverse industrial processes and applications. In polymer surface modification, synthetic end-function polymers tethered to surfaces can service to provide facile control of surface properties ranging from wettability and adhesion to friction and biocompatibility.[1-3] Also surface tethered polymers can be used to stabilize colloidal particles and to minimize protein adsorption.[4,5] Innovative biomedical applications such as targeted magnetic hyperthermia,[6] targeted drug delivery,[7] genotyping,[8] and the emerging field of glycomics (i.e., carbohydrate microarrays)[9] all involve the covalent attachment of some biological macromolecule of interest (such as DNA, carbohydrates and proteins) onto the surface of substrates such as silicon wafers, nanoparticles and even micelles. These examples of polymer interfacial reactions demonstrate the significance of learning more about the chemistry at the interface.

Chemisorbed or covalently bound polymer layers have many advantages as compared to physisorbed polymer layers. First, a polymer physisorped layer normally involves absorption of block copolymer onto a substrate, where one block interacts strongly with the surface and the other block forms a polymer brush. The disadvantages associated with physisorption include thermal and solvolytic instabilities due to the non-covalent nature of the grafting, poor control over polymer chains density and complexity

in synthesis of suitable block copolymers. Chemisorbed polymer shells, however, provide a perfect way to fully cover the surface with a permanent, stable layer that is not vulnerable to desorption or displacement. Second, by properly tailoring the substrate and polymers, one may design smart surfaces with desired surface characteristics. This may be done, for example, by modifying the polymer chain length or architecture and can also be achieved by choice of solvent as well as substrate.

Polymers can be grafted onto surfaces by either "grafting from" or "grafting to" techniques.[1] The grafting-from approach involves the immobilization of initiators onto the substrate followed by *in situ* surface initiated polymerization used to generate the tethered polymer brush. This technique often leads to imprecise control of the molecular weight of the brush and uncontrolled polydispersity. To overcome this problem, the grafting-to approach can be used and has become the most attractive way to prepare polymer brush. Polymer chains with desired lengths are first synthesized and purified and are then allowed to react with the surface. Also, mixed brushes containing different types of chains in controlled ratios also can be constructed by means of the grafting-to approach.[10] Finally, the grafting-to approach can be conducted under ambient conditions, whereas many versions of the grafting-from approach require demanding moisture-free or oxygen-free conditions.

Polymer interfacial reactions are far more complex the reactions involving small analogue reactants due to a number of variables that could affect the molecular structure and behavior of polymers at interfaces. Morawetz *et al.*[11] illustrated the intrinsic complexity of reactions involving polymeric reactants as a result of steric and thermodynamic effects. The importance of interfacial reactions and their complicated

fundamental behavior provides strong a motivation for further studies on the kinetics of polymer interfacial reaction. Most theoretical[12,13] and simulation[14,15] studies focus on prediction of the kinetics of polymer interfacial reaction. Most experimental studies of grafted polymer layers have concentrated on the characteristics and behavior of dense polymer brushes.[16-22] However, kinetic experimental studies of the grafting-to process, however, are not well-discussed in the literatures.[23-28] According to theoretical predictions and simulation results, the kinetics follows two regimes. In the first regime, the reaction of grafting the polymer chains to the bare, solid surface is relatively rapid and controlled by the center-of-mass diffusion of the polymer chains through the solvent to the surface. This results in a low grafting density of the polymers which translates to mushroom configurations of the polymers. The mushrooms are able to form since the distance between adjacent polymer chains is much larger than the size of a free, undeformed chain in solution. In addition, the reaction corresponds to a rate that is proportional to $t^{0.5}$ in a quiescent system, where diffusion and convection happen at the same time. Therefore the first regime ends when the $t^{0.5}$ typical behavior terminates. When the grafted polymer chains begin to overlap, the second regime, or penetration regime, begins. Because the incoming polymer chains have to penetrate bound polymer layers to reach the surface, an energy barrier is created. The continuous increase in the barrier for penetration as the reaction progresses is predicted to cause the reaction rate to decline with the natural logarithm of time. Eventually, the energy gained by forming a chemical bond is offset by the entropic cost of crowding another chain into the interphase and the reaction ceases, a condition referred to as saturation.

Penn *et al.*[10,28-32] showed experimental measurements of reaction kinetics for end-functional polymers in solution reacting with a functional substrate, using an indirect GPC-based analysis of the depletion of reactants from the solution. However they were not able to provide sufficient data of measurements within this short first regime to fully characterize its time dependence. Also, the reaction between the primary amine end functional groups of polystyrene and epoxide functional groups grafted to the surface of silica substrate lasted a week, making the sampling difficult to monitor and thereby discontinuous. Furthermore, Penn discovered a third regime wherein the reaction rate was found to accelerate up to the point of saturation, an effect which is not fully understood. Hence direct kinetic studies of such reaction are necessary and important.

Attenuated total reflection infrared spectroscopy (ATR-IR) is a technique that is particularly well suited for the direct *in situ* characterization of interfacial reactions. ATR-IR involves passing an infrared beam through a trapezoidal ATR plate wherein the beam experiences multiple reflections within the crystal. At each reflection an evanescent field makes a brief excursion outside of the crystal, thereby sampling the infrared spectrum of whatever is in contact with the crystal.[33] If a functional SAM is deposited on the crystal, its reaction with polymer chains in a contacting solution can therefore be followed by recording the ATR-IR spectrum.[34] Germanium (Ge) substrates are particularly interesting for this application because the evanescent field decays over a relatively short distance of about 500 nm imparting good surface sensitivity.

In this study, the click reaction between azides and alkynes was selected as a model reaction for the grafting-to process because click reactions proceed rapidly to very high conversion under mild condition with no side reactions or byproducts and the

resulting aromatic triazole is extremely stable.[35] In addition, click reactions are highly chemoselective, that is, orthogonal to almost all other chemistries. More importantly for the infrared technique is the appearance of the absorbance bands of alkyne and azide groups within the windowpane region of the spectrum near 2100 cm^{-1}, where there is no interference from other absorbance bands, and because click functional monolayers of this nature can be readily prepared on a variety of substrates. Also a successful quantification of the kinetics of an interfacial click reaction between azide end functionalized SAMs and an alkyne-functional reactant was demonstrated by our previous work in Chapter 3.[36]

In this Chapter, we have developed and shown a successful method for studying the click reaction kinetics of alkyne end-functional polystyrene (PS) and poly n-butyl acrylate (PnBA) reacting to SAMs with desired areal density of azide end-functional groups. Time-resolved ATR-IR measurements were used to quantify the kinetics of such reaction, coupled with ellipsometric results. Different configurations of grafted polymer layers were also characterized by AFM.

5.2 Experimental Section

5.2.1 Synthesis of Polymers (alkyne-PnBA-Br and alkyne-PS-Br)

A mixture of initiator Propargyl 2'-bromoisobutyrate, N, N, N', N', N'-pentamethyldiethylenetriamie ligand (PMDETA), monomer n-butyl acrylate (nBA) or styrene, and solvent (DMF) were loaded in a Schlenk flask. After freeze-pump-thaw three times, catalyst CuBr was added and quickly dissolved. The flask was placed in oil bath at

70 ℃ to the desired reaction time. After the reaction, the catalyst was removed by passing through activated neutral alumina column. The polymers were obtained by concentrating the reaction mixture in vacuum to constant mass. In this fashion, three polymer molecular weights of PnBA and two polymer molecular weights of PS were synthesized. Samples were dissolved in $CDCl_3$, and the conversion was measured by H^1-NMR. Samples were dissolved in THF and were injected into a Shimazu LC-10AT gel permeation chromatography system (GPC), equipped with a refractive index detector to measure the number-average and weight-average molecular weights relative to PS standards. Molecular weights were corrected for hydrodynamic volume effects by application of a universal calibration using Mark-Houwink-Sakurada parameters.[37-39] (PS: K=1.41 and a=0.716; PnBA: K=1.22 and a=0.700, both are in THF) and the following formula:

$$log\ (M) = \frac{1}{1+a}\log\left(\frac{K_{Ref}}{K}\right) + \frac{1+a_{Ref}}{a}\log(M_{Ref}) \quad (5.1)$$

The number-average molecular weights of PnBA were calculated according to the equation:[40]

$$\log(M_{PnBA}) = 1.01\log(M_{PS}) - 0.02 \quad (5.2)$$

The values of M_n, PDI and M_w of PnBA are summarized in Table 5.1.

Table 5.1. Values of M_n, M_w and polydispersity (PDI) for PnBA.

M_n from GPC	Adjusted M_n after universal calibration	PDI (M_w/M_n)	Adjusted M_w
2700	2790	1.10	3069
5700	5935	1.08	6410
10000	10471	1.06	11099

5.2.2 Substrate Preparation

The overall modification of Ge surface includes several processes: cleaning and activation, silanization, controlled azide substitution, and 'click' reaction with polymers (PnBA and PS), as shown in Scheme 5.1.

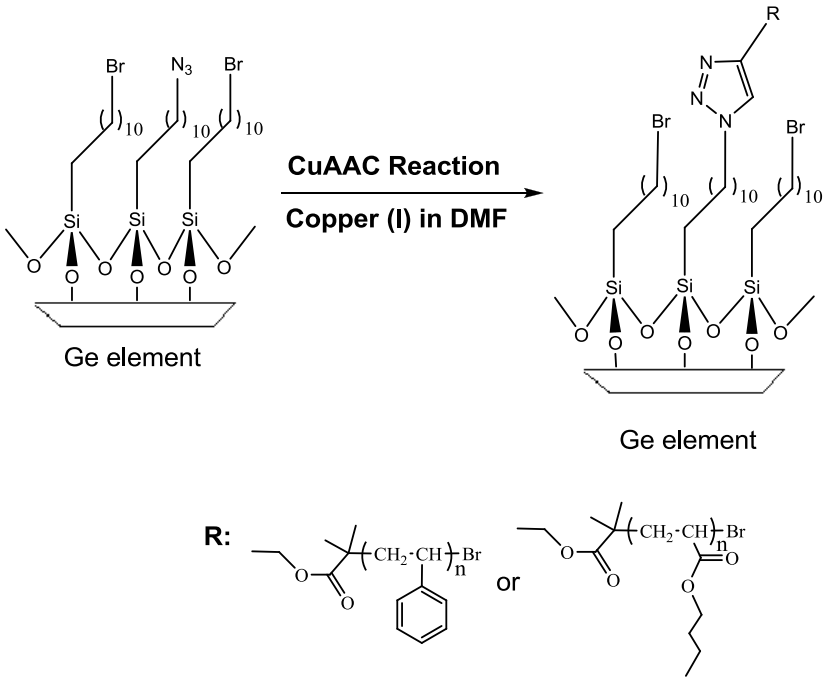

Scheme 5.1. ‘Click’ modification of Ge surface.

The Ge surface was degreased by sonicating in acetone, methanol and DI water for 5 min. Then the surface was dried with N_2 and exposed to UV-ozone under ambient conditions for 15 min. Finally the surface was abundantly rinsed with DI water and dried under nitrogen flux.

The activated Ge surface was immersed in a solution of BUTS (0.08% v:v) in a mixture of undecane and carbon tetrachloride (7:3 v:v). Afterwards, the Ge substrate was sonicated in toluene, gently scrubbed with a toluene-soaked tissue to assist in removal of possible physisorbed multilayers, and rinsed with toluene. Finally, the surface was dried under nitrogen flux.

The silanized Ge surface was exposed to a saturated solution of sodium azide in DMF for 2 minutes to reach a desired conversion of 33%. And the reaction was quenched

by thoroughly rinsing with an excess of DI water, and the Ge crystal was sonicated with toluene and finally dried under nitrogen flux. According to the previous calculation in Chapter 4.2, the areal density of azide on surfaces is 1 chain/nm^2, selected for a specific purpose. As the projected area of reactive face of polymers to the interface is much bigger than that of azide groups on the surface, the conversion of click reaction would be pretty low if the surface is fully covered with azide groups leading to possible difficulty of monitoring a small change in the peak area of absorbance band of surface azides. It is obvious that the lower the areal density of azide groups on the surface, the higher conversion the reaction, the more accurate quantification of the change in azide absorbance. However, at the same time, the azide absorbance should be high enough to be observed in the infrared spectra during the click reaction.

5.2.3 ATR-IR Measurements of Click Reaction Kinetics on Surface

The modified Ge crystal with azide end groups was placed into a liquid ATR flow cell. A solution of PtBA (40 mg, M_w 2700), $CuSO_4$ $5H_20$ (1 mg, 0.004 mmol) and sodium ascorbate (3.36 mg, 0.016 mmol), dissolved in a co-solvent of DMF (1 ml) and H_2O (10 µl), was injected into the cell whereupon it contacted the azide functionalized Ge surface to initiate the click reaction. The reaction was performed at room temperature in the air for 2 days with spectra recorded every 2 minutes with 100 scans acquired. Background was collected with the bare Ge crystal. Automatic baseline correction methods were applied to all the spectra. All the above process was repeated three times for all the polymers with various molecular weights.

5.2.4 Surface Characterization

Infrared spectra were obtained with a Nicolet 560 FTIR (MCT/A detector, broad range 4000-650 cm^{-1}, liquid N2 cooled), coupled with an ATR accessory at a resolution of 4 cm^{-1} with an aperture of 100. The internal reflection element was a $50 \times 10 \times 2$ mm trapezoidal Ge crystal with an aperture angle of $45°$ yielding 13 internal reflections. The Ge crystal was incorporated within a flow through liquid cell.

The thicknesses of polymer thin films were measured with a Beaglehole spectroscopic and imaging ellipsometer (Beaglehole Instruments, Wellington, New Zealand) under angle mode (70°) with a fixed wavelength of 632.8 nm. The final thickness data were averaged over multiple measurements (greater than three) taken at different locations on different sample. The measured ellipsometric data were analyzed using Film Wizard software. The samples were prepared as a function of time. The azide modified Ge wafers were exposed to the polymer solution with catalyst under the same condition for ATR-IR measurements. The substrate was withdrawn from the solution every 10 minutes for the first 30 minutes, followed by increments of 20, 30, and 60 minutes thereafter. After each withdrawal, the substrate was washed with DI water to quench the reaction, followed by sonication with toluene so as to remove the possible physisorbed polymer chains. The substrate was finally dried under nitrogen flux.

Noncontact mode AFM measurements using the AutoProbe CP Research Probe head (Veeco Instrument) were performed to study the topography of polymer films. Silicon cantilevers (dLeversTM) with a spring constant of 2.2 N/m were employed and the analysis was carried out under air-ambient condition.

5.3 Results and Discussion

Interfacial reactions can be monitored by covalently attaching a functional group onto the surface of the substrate. Click reaction has been chosen as a model functionalization and as such, the substrate is first modified with azide groups. This has been accomplished for Ge crystal (wafers) by tethering mixed SAMs containing a known amount of azide to give 1 chain/nm^2. The thickness of the SAM was determined by angle dependent x-ray photoelectron spectroscopy analysis to be 1.6 ± 0.2 nm, while that measurement by ellipsometry gave a similar value at 1.6 ± 0.1 nm. From the structure of the silane with full conversion of azide substitution, the thickness is expected to be about 1.7 nm, in close agreement with the experimental result.

5.3.1 ATR-IR Results

An infrared spectrum of the functionalized Ge substrate is presented in the upper part of Figure 5.1. The ratio of the absorbance areas of the azide groups to that of the methylene groups was calculated to be 0.14, which is 0.34 lower than the ratio of 0.41 for a surface fully covered with azide groups of areal density of 3 chains/nm^2. Based on this, it has been determined that the areal density of azide groups in the mixed SAMs is 1chain/nm^2. After the azide modified surface reacts with alkyne end-functional PnBA (M_w=3069), successful surface modification is illustrated by a decrease in the ratio of azide absorbance to that of CH_2, and a growth in a carbonyl absorbance at 1682 cm^{-1} and 1733 cm^{-1}, and CH_3 absorption at 2960 cm^{-1}, as shown in the lower part of Figure 5.1.

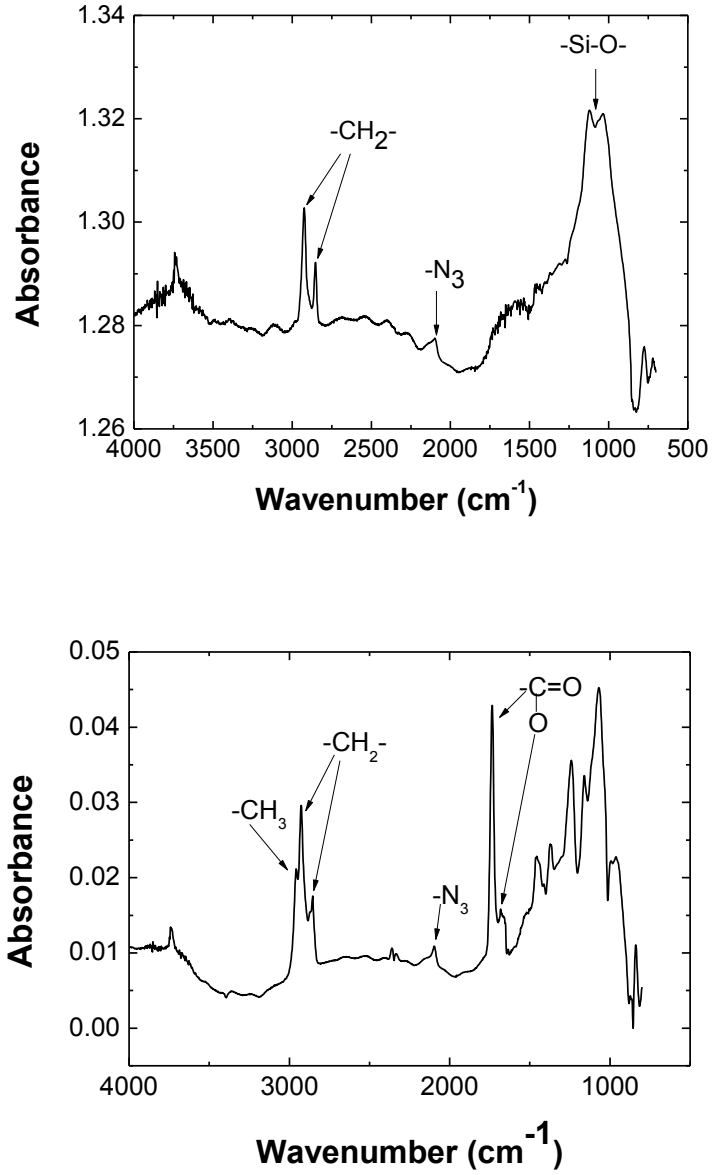

Figure 5.1. ATR-IR spectra before CuAAC reaction (upper spectrum) and after CuAAC reaction (lower spectrum).

After the injection of a polymer solution with catalyst, the spectra was collected every 2 minutes to record the change in the absorbance of surface azide groups and subsequently the grafting density of tethered polymer chains was calculated based on the conversion of surface azide. Automatic baseline correction methods were applied to all

the spectra. The absorbance band for the alkyne groups (around 2112 cm^{-1}) overlaps with that for azide groups (see Figure 5.2). A background subtraction procedure was developed in Chapter 3 through which the decrease in the intensity of the azide absorbance band (around 2100 cm^{-1}) as a function of time could be monitored during the CuAAC reaction. Figure 5.2 shows a typical result for ATR-IR monitoring of the interfacial click reaction.

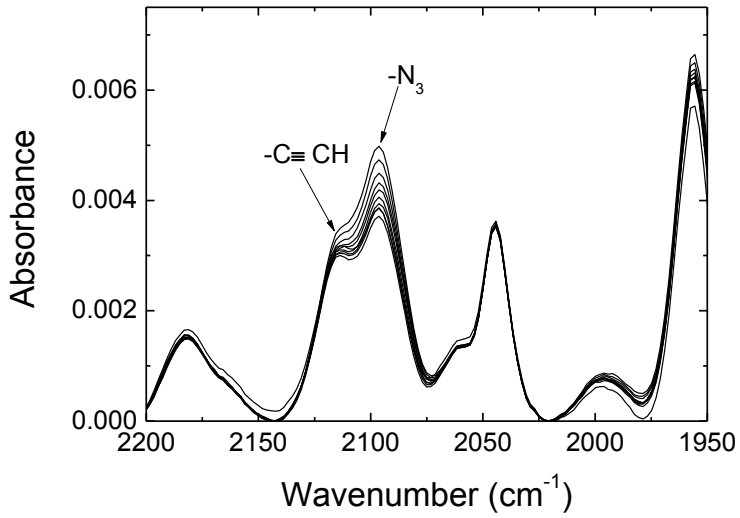

Figure 5.2. ATR-IR spectral changes during the CuAAC reaction of mixed azide SAMs and PnBA (M_w=3069). The topmost spectrum was recorded at the beginning of the reaction and afterwards the series of spectra was recorded 2 minutes.

As described in Chapter 3, the azide absorbance band was isolated from the overlap by subtracting a weighted spectrum of a solution of PnBA on the unmodified Ge surface from the reaction spectrum. The subtraction was performed by adjusting the weighting factor until the contributions of absorbance bands below about 1700 cm^{-1} were completely removed. Polymers were dissolved in DMF, which is a good solvent for

PnBA and PS, so that the segmental absorption of polymer chains would be absent. Since we use an excess of polymer compared with surface azide, the kinetics of interfacial reaction is expected to be limited by the tethered polymer chains on the surface. The reactions were conducted from dilute solution (40 mg/cm^3) of long duration (two days).

A typical kinetics curve for the reaction of alkyne-terminated PnBA (M_w=3069) reacting with an azide functionalized Ge surface is shown in Figure 5.3. The reaction is initially rapid and slows down considerably before reaching an ultimate saturation with grafting density of 0.5 chains/nm^2. The initial zero point in the plot was determined from infrared spectra obtained by the control experiment of exposing the azide modified Ge crystal surface to a polymer solution without catalyst under the same concentration condition. Data was collected beyond the time of the saturation to verify that saturation is reached and standard errors of data come from the repeatability of experiment.

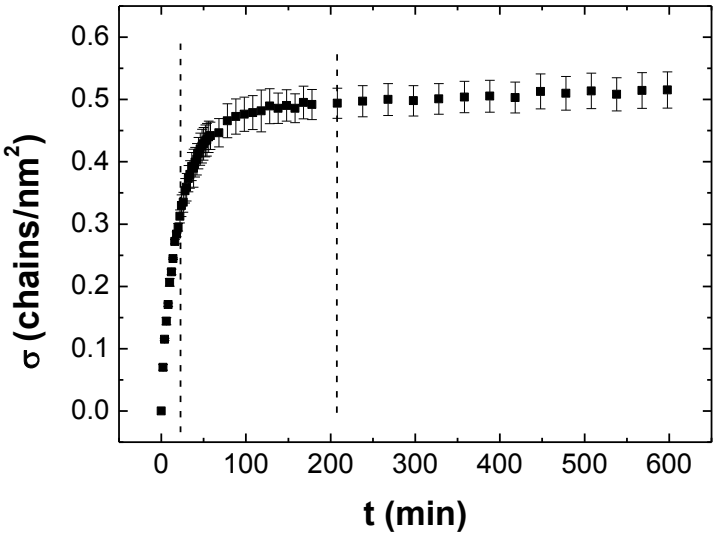

Figure 5.3. A plot of grafting density of PnBA chains (chains/nm^2) v.s. time (minutes): thin vertical lines roughly separate several different regions based on the reaction rate.

To get a more detailed understanding of the kinetics curve, a plot of attachment density of polymer chains v.s. $t^{0.5}$ is demonstrated in Figure 5.4. Fitting statistics were manipulated to gain a linear relationship between σ and $t^{0.5}$: the first four data of (x, y) were plotted to be a linear line and some weighting factors (adjusted R^2 and slope rate) were analyzed, and more and more data points were incorporated into the linear dependence until big variances in the values of adjusted R^2 and slope rate occurred. Theory predicts at the first regime, the reaction is predicted to be center-of-mass diffusion controlled with a $t^{0.5}$ dependence for a quiescent system. Diffusion of the functional end of the chain to an active site on the surface is fast by comparison. As seen in Figure 5.4, regression of the data up to 18 minutes gives a $t^{0.5}$ dependence in excellent agreement with the theoretical prediction. At a transition point $\sigma_{1,}$ the attached polymer chains are expected to be on the verge of overlapping, but still in the relaxed configuration and they are depicted as hemispherical coils, called mushrooms.

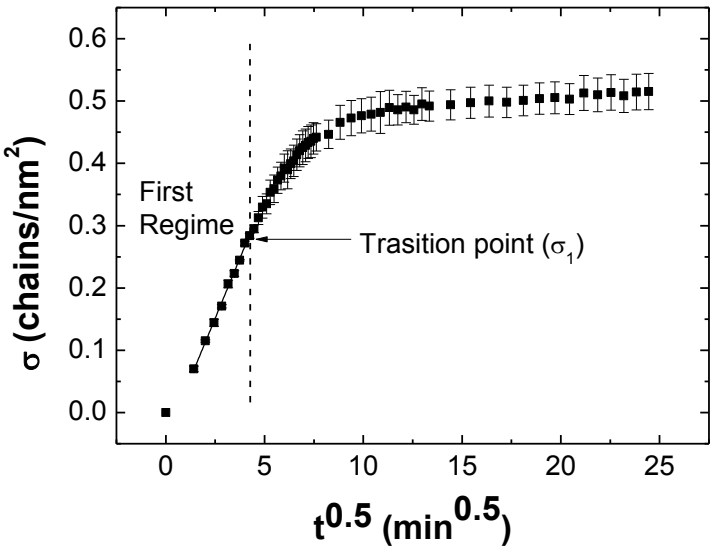

Figure 5.4. A plot of grafting density of PnBA chains v.s. $t^{0.5}$: thin vertical lines separates the first regime from left-over data.

At longer time in the sterically hindered regime, the kinetics is predicted to depend on the logarithm of time. As shown in Figure 5.5, the second regime corresponds well with the theoretical prediction, in that the reaction rate declines with the natural logarithm of time because of the progressive increase in the barrier for penetration as the reaction proceeds. Figures 5.5 also presents a most interesting feature by far, the appearance of another two transition regimes of kinetics prior to saturation instead of the two regimes predicted by theory. After the second regime, the reaction rate reduces moderately and then increases relatively up to the ultimate saturation characterized by two transition points. Such polymer behavior at an interface is not fully understood, and a possible explanation is that the strong repulsion force between the densely-packed polymer layers forces them to extend vertically and contract laterally at the same time, leading to some room for just a few incoming polymer chains and thereby accelerating

the tethering process slightly before reaching saturation. At saturation, it should be noticed that the attachment density of the grafted layer is nearly 0.5 chain/nm^2, less than the 1chain/nm^2 areal density of azide active sites. That means that the density of functional groups on the surface was more than sufficient to accommodate the surface grafting density reached by the tethered chains. While compared with the dense polymer brushes made by surface initiated grafting-to approach,[41] the polymer layers formed here are considered to be moderately dense.

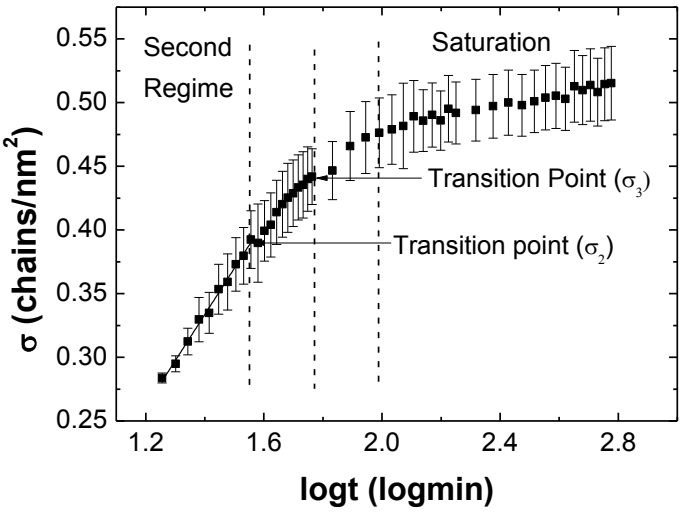

Figure 5.5. A plot of grafting density of PnBA vs. logt: thin vertical lines separate different regimes.

The same kinetic behavior was observed for PnBA and PS with different molecular weights, as listed in Figure 5.6-Figure 5.9. All of them exhibit four-regimes of kinetic behavior with three characteristic transition points. The most interesting phenomena after the first two regimes were more prominent for PnBA (M_w=11099) and PS (M_w=9500), mainly because higher molecular weights have lower grafting density and

more flexible polymer chains. The more space the existing polymer layers provide for the incoming polymer chains, the easier is the further tethering process.

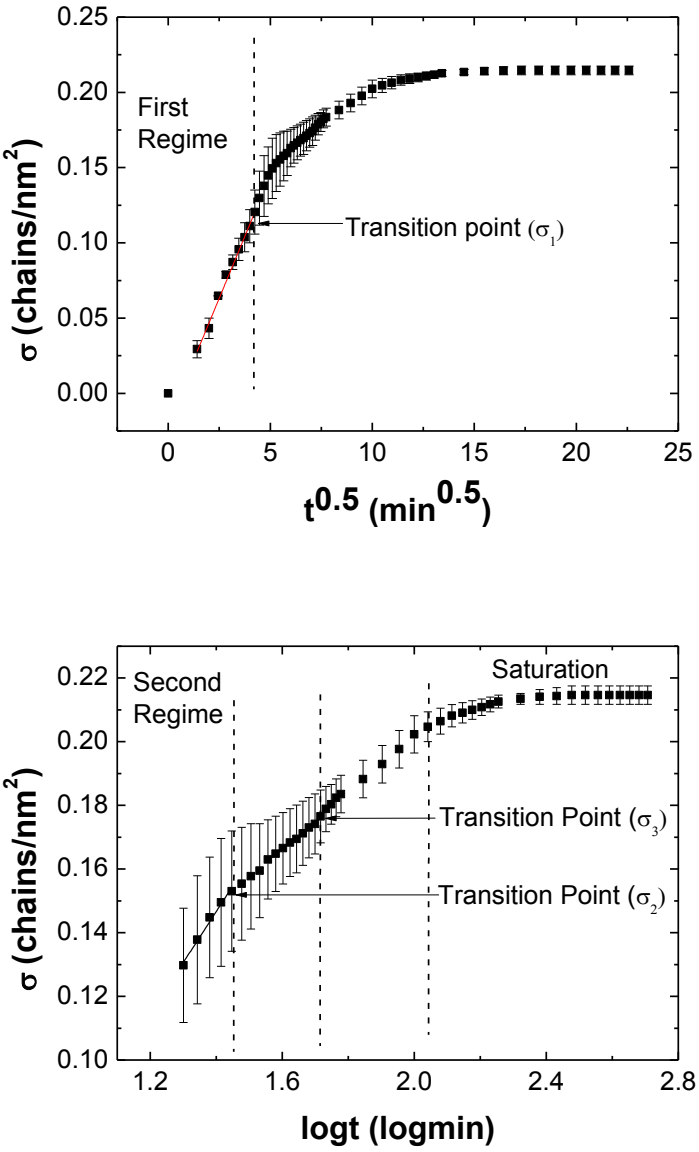

Figure 5.6. Kinetics curve for the reaction of alkyne-terminated PnBA (M_w=6410) reacting to azide groups on Ge crystal.

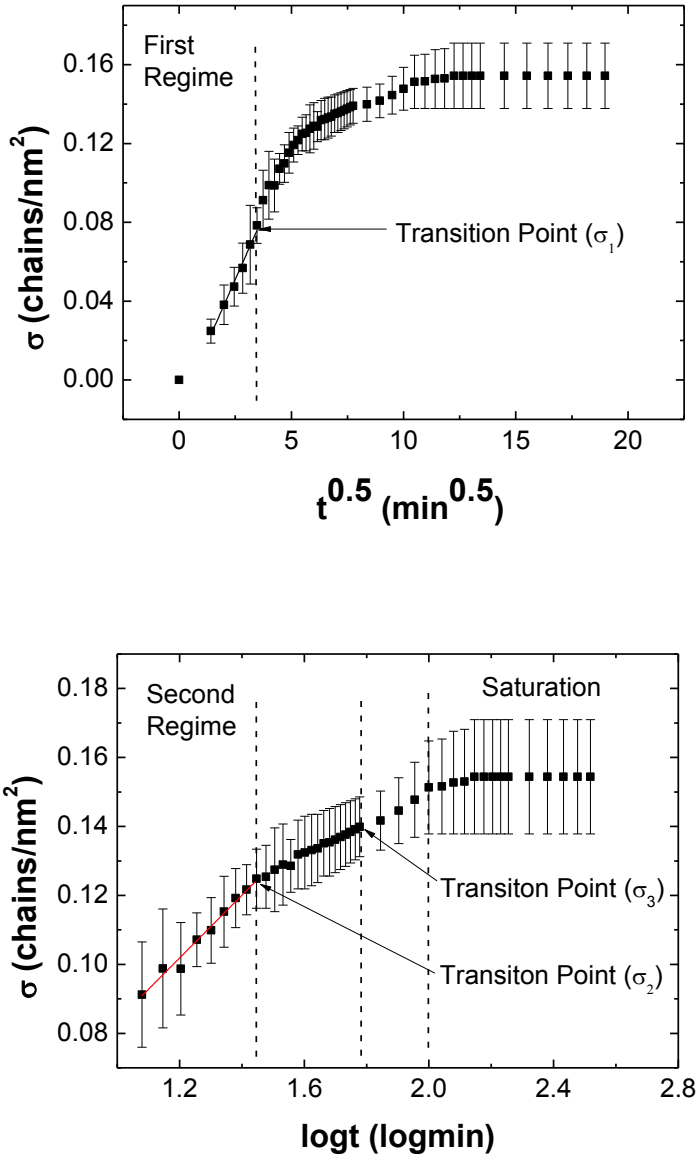

Figure 5.7. Kinetics curve for the reaction of alkyne-terminated PnBA (M_w=11099) reacting to azide groups on Ge crystal.

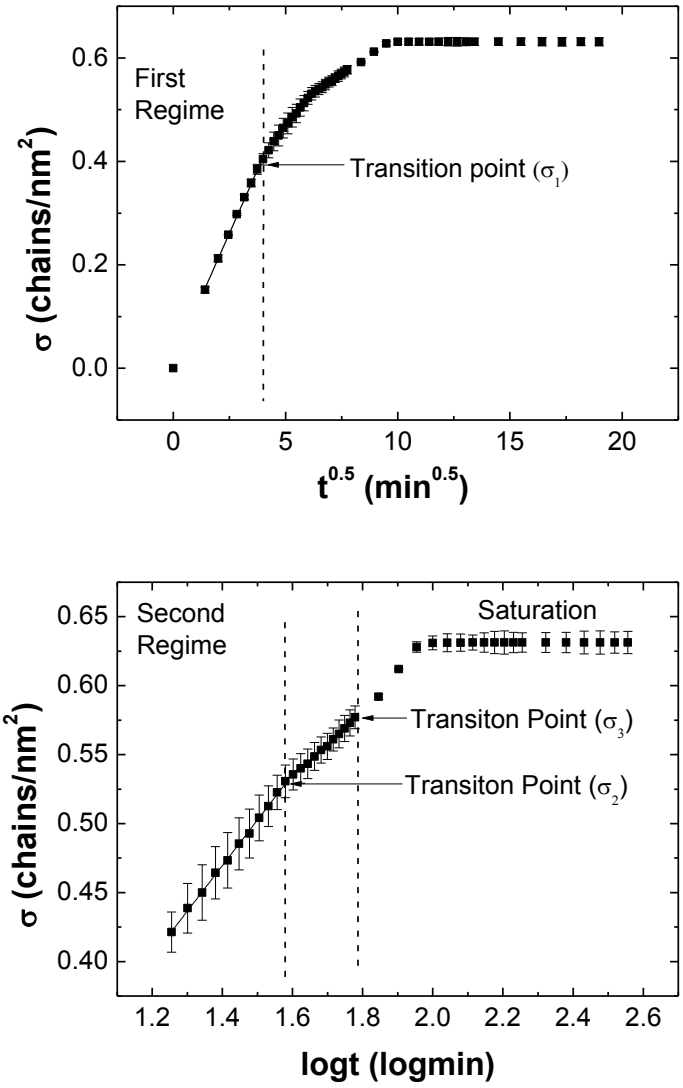

Figure 5.8. Kinetics curve for the reaction of alkyne-terminated PS (M_w=2400) reacting to azide groups on Ge crystal.

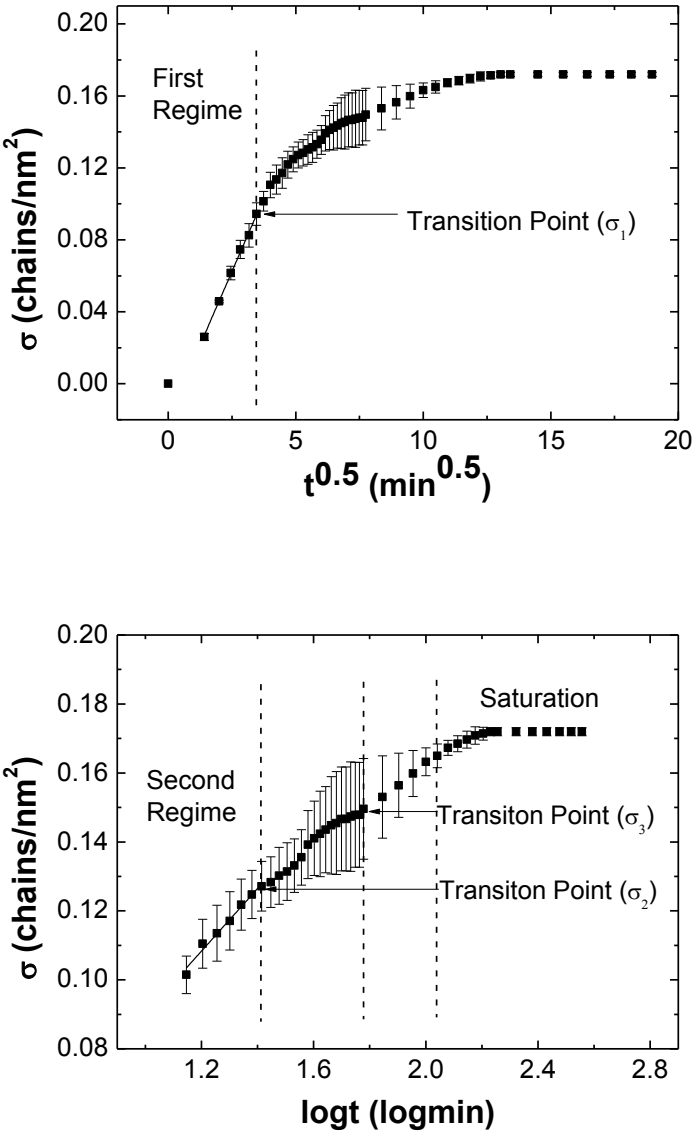

Figure 5.9. Kinetics curve for the reaction of alkyne-terminated PS (M_w=9500) reacting to azide groups on Ge crystal.

To quantitatively explain the intrinsic relationship between the three transition points, we define a threshold, σ^*, as the grafting density of polymer layers when they just begin to touch each other and essentially behave as isolated chains in solution., indicating the end of the first regime and completion of a mushroom layer on the surface. The

attached polymer layer can be described by the blob model,[42,43] in which the excluded volume interaction become negligible outside a certain region, called a "blob", around chain. A single "blob" is formed at σ^*, which is approximately equal to $1/R_g^2$ in two dimensions, similar to c^* of polymer solution in three dimensions, where R_g is the radius of gyration of polymer chains in solution.

The radius of gyration (R_g) of polymer in good solvent DMF can be calculated by the equation: [44]

$$R_g = \frac{N^{0.6}}{\sqrt{6}} a \tag{5.3}$$

where N is the degree of polymerization, a is statistical segment length which is taken to be 0.6 nm for PS and 0.7 nm for PnBA.[45] All values of R_g and σ^* are listed in Table 5.2

Table 5.2. Characteristic values of polymer chains in dilute solution and at the surface.

Polymers	M_w	R_g (nm)	σ^* (chains/nm^2)
PnBA	3069	1.9	0.28
	6410	3.0	0.11
	11099	4.1	0.06
PS	2400	1.6	0.39
	9500	3.6	0.08

At the completion of the first regime, $\sigma_1$is expected to be equal to σ^*, and that is what is found in every case regardless of polymer nature and molecular weight, as

presented in Table 5.3. And the reduced surface density Σ_1 ranges from 3.1 to 4.0, close to previous experimental results.[46] Therefore we can conclude that the first regime in the experimental results corresponds well to the theoretical prediction and a loosely-packed and relaxed mushroom layer is formed at the surface. In addition, when the other two transition data were compared with σ^*, their ratios are similar except for the polymer with high molecular weight. From the theoretical study,[13] the monomer volume fraction of attached chain is parabolic and dependent on the polymer molecular weight. A high value of M_w leads to a widely-distributed parabolic plot. As a result, it is difficult to determine σ^* and the comparison of transition points with σ^* can show large deviations. Nevertheless, why abrupt shifts of the reaction rate happen at σ_2 and σ_3 is not fully understood. From the values of $\Sigma_{saturation}$, we can conclude the reaction does not reach the highly-stretched regime.[46]

Table 5.3. Comparison of transition points with σ^*.

Polymers	M_w	σ_1/σ^*	Σ_1	σ_2/σ^*	σ_3/σ^*	$\Sigma_{saturation}$
PnBA	3069	1.0	3.1	1.4	1.6	6.0
	6410	1.1	3.4	1.4	1.6	6.0
	11099	1.3	4.0	2.0	2.3	7.9
PS	2400	1.0	3.1	1.4	1.5	5.1
	9500	1.1	3.4	1.6	1.9	6.6

As for the effect of experimental variables on the kinetic behavior, some general observations can be made. Firstly, Christian *et al.* predicted that below σ^*, there is

essentially no activation barrier and the first regime is controlled by chain diffusion in the solution:[13]

$$\sigma(t) \sim \left(\frac{Dt}{a^2}\right)^{\frac{1}{2}} \left(\frac{\phi_0}{N}\right) \tag{5.4}$$

where σ(t) is grafting rate, D is the chain diffusion coefficient, ϕ_0 is the volume fraction of polymer monomers in solution. Equation 5.4 indicates polymer with high molecular weight diffuses more slowly than polymer with lower molecular weight. As fully expected, elevation of molecular weight, with monomer concentration held constant, resulted in a decrease in the slope rates of the first regime from 0.077, 0.033 to 0.025 for PnBA and from 0.098 to 0.033 for PS, in good agreement with prediction from equation 5.4. Since ϕ_0 is same for all the polymers regardless of molecular weight and polymer nature, the diffusion rate (defined as $\sigma(t)/t^{0.5}$) should be proportional to $D^{0.5}/M_w$.

Theory predicts D is proportional to $M^{-0.6}$ and previous experimental result indicates D is proportional to $M^{-0.55}$.[47] So the diffusion rate should be proportional to $M_w^{-1.3}$ (by theory) or $M_w^{-1.275}$ (by experiment). A negative log-log relationship between diffusion rate and molecular weight is found (Figure 5.10) with a proportionality of -1.0±0.11, close to theoretical predication and previous experimental result.

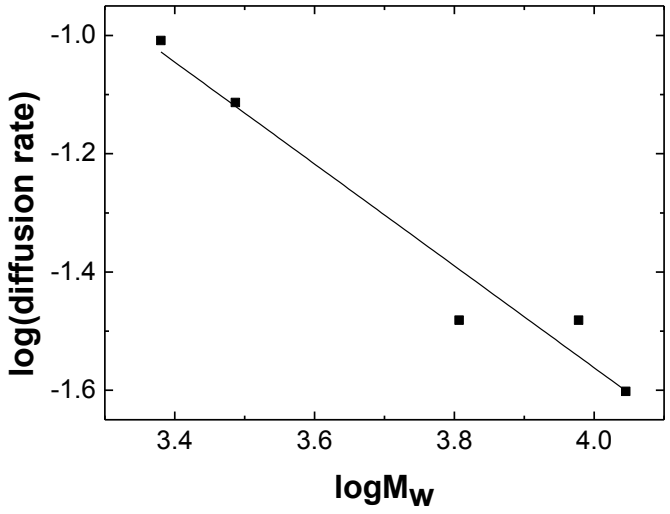

Figure 5.10. Log-log plots of slope rates at first regime vs. molecular weights for click reaction of polymers reacting to azide mixed SAMs.

Secondly, Christian *et al*. also predicted the second regime is controlled by the penetration of the free polymer chains into the grafted polymer layer,[13]

$$s^{1/3} e^{\gamma N \sigma_{eq} s^{2/3}} \cong \frac{2}{3} N \sigma_{eq} T \qquad (5.5)$$

where s (σ/σ_{eq}) and T(t/τ) are reduced variables, τ is a short characteristic time, τ and γ are constants. From equation 5.5, we can conclude penetration rate (defined as $\sigma(t)/\log t$) is inversely proportional to M_w. In the second regime, the linear relationships between grafting density and logt give slope values of 0.36, 0.16 and 0.09 for PnBA, 0.33 and 0.90 for PS, listed from low M_w to high M_w, indicating the energy barrier to penetrate is smaller for polymer with lower molecular weight. Experimental log-log plots of penetration rates vs. molecular weights produced straight lines are shown in Figure 5.11. The calculated dependence from the two straight lines is -1.0 and -0.94, from analysis of PnBA and PS respectively. The values are close to theoretical prediction.

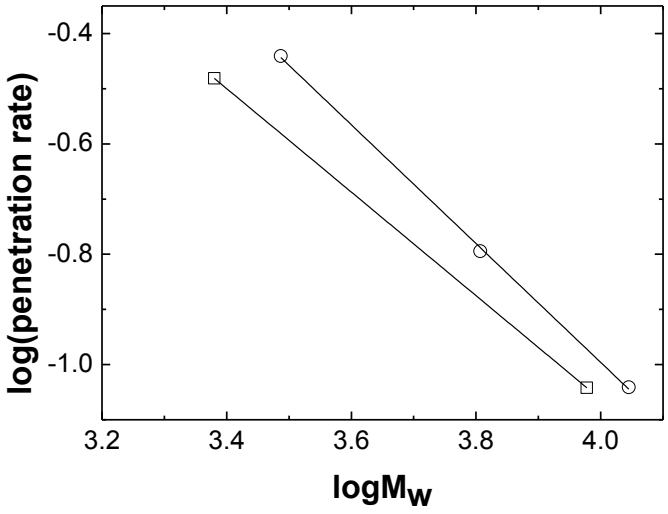

Figure 5.11. Log-log plots of slope rates at second regime vs. molecular weights for click reaction of polymers reacting to azide mixed SAMs. The circles are based on results from PnBA and the squares are based on results from PS.

5.3.2 Ellipsometry Results

The ellipsometric thicknesses of adjacent polymer layers are shown as a function of reaction time in 5.12. For each polymer, the thicknesses of the covalently bound layer initially achieve a high extent after the first 10 minutes. Then they grow continuously until 30 minutes, slow down up to 50 minutes, followed by a relatively rapid increment from 50 to 100 minutes. For all cases the saturation values are reached at 220 minutes under the described conditions. The time dependence of kinetic behavior demonstrated here is consistent with the transition moments obtained from the previous experimental analysis of ATR-IR results.[48,49]

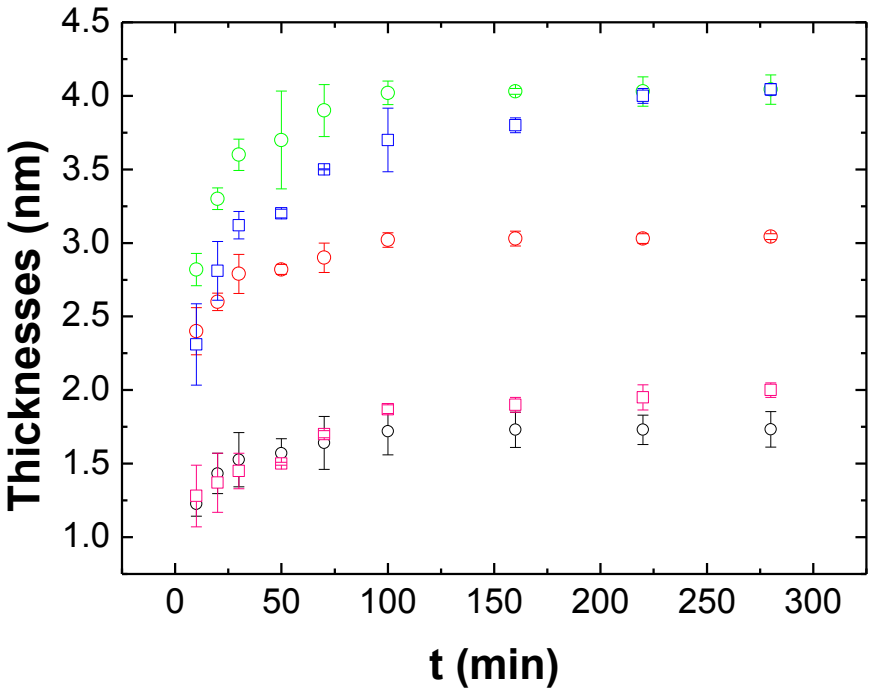

Figure 5.12. Influence of the reaction time on the thickness of attachment of PnBA and PS. The black circles represent results of PnBA (M_w=3069), the red circles represent results of PnBA (M_w=6410), the green circles represent results of PnBA (M_w=11099), the pink squares represent results of PS (M_w=2400), and the blue squares represent results of PS (M_w=9500).

The grafting density of a densely-packed polymer brush can be calculated from ellipsometric results:

$$\sigma_{saturation} = \frac{\rho d_{sautration} N_A}{M_w} \quad (5.6)$$

where $d_{saturation}$ is the thickness of polymer layer at saturation in dry state, ρ is the density of polymer at room temperature (PnBA: 1.2 g/cm^3, PS: 1.0 g/cm^3), N_A is Avogadro constant. By comparing $\sigma_{saturation}$ with ATR-IR results, we can predict the

configuration of polymer layers (Table 5.4). For polymer with the low M_w, the polymer layer is densely-packed, as it acts more like a rigid rod. However, elevation of M_w leads to the difficulty of forming a densely-packed polymer brush due to an increase in polymer flexibility.

Table 5.4. Comparison of grafting density of polymer layer at saturation from ellipsometric calculation and ATR-IR results.

Polymers	M_w	$\sigma_{saturation}$ from ellipsometry (chains/nm^2)	$\sigma_{saturation}$ from ATR-IR (chains/nm^2)	Configuration
PnBA	3069	0.40	0.52	densely-packed
	6410	0.34	0.21	Moderately-packed
	11099	0.26	0.15	Moderately-packed
PS	2400	0.53	0.63	densely-packed
	9500	0.27	0.17	Moderately-packed

5.3.3 AFM

The roughness of different configurations was characterized by AFM and the topography of “mushroom” layers are rougher (RMs: 3 nm) than that of “brush” layers (RMs: 1 nm) in Figure 5.13.

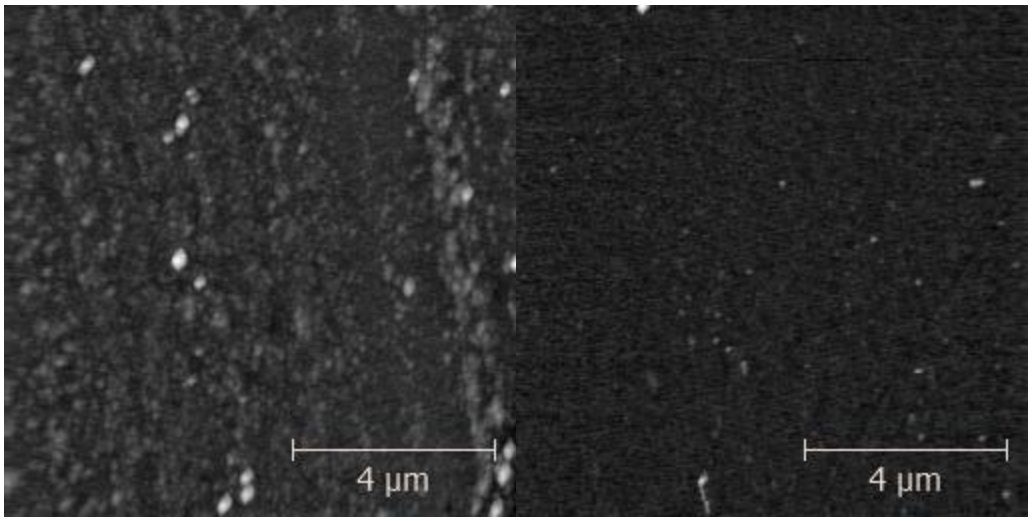

Figure 5.13. Topography of grafted PS chains on surface (M_w 9500): left is "mushroom" and right is "brush".

5.4 Conclusions

In this Chapter we propose a new ATR-IR method to directly monitor the kinetics between high-quality azide functional monolayers modified on Germanium crystal surface and alkyne end-functional polymers, such as poly (n-butyl acrylate) (PnBA) and polystyrene(PS), via a copper-catalyzed 1,3-dipolar cycloaddition reaction. The time-resolved ATR-IR measurements exhibit four-regimes of kinetic behavior. As predicted from theory, in the first regime, the rate is rapid and controlled by Brownian diffusion of polymer through the solvent, scaling with the square root of time. And the first regime terminates with a grafting density of polymer layers equal to a defined σ^*. In the second regime, the rate slows considerately because of the energy barrier when the polymer chains have to penetrate a covalently bound polymer brush to arrive at the surface, and the rate is proportional to logarithm of time. There are another two regimes before

saturation, where the reaction rate slows down slightly and then accelerates briefly with two characteristic transition points. A possible explanation for this behavior is that the tethered polymer layer contracts laterally during the transition from “mushroom” to “brush” and thereby provides additional space for a few incoming polymer chains. Compared with PnBA of similar molecular weight, PS has a higher grafting density of polymer chains at saturation because of its smaller radius of gyration. The ellipsometric results demonstrate an increase in the thickness of the polymer layer as the reaction continues and a constant thickness of polymer brush after the reaction reaches saturation. Also the kinetic behavior observed in the thicknesses data of tethered polymer layers corresponds well to results acquired by ATR-IR measurements. A number of factors that influence the kinetics of the polymer interfacial reaction are investigated including polymer nature and molecular weight. Atomic force microscopy reveals that the topography of “mushroom” layers is rougher than that of “brush” layers. Through investigating the kinetics and factors that govern the polymer interfacial reactions, one can design smart surfaces and subsequently control the interfacial properties they bring about based on specific needs. For instance, a mushroom layer is preferable to a brush layer for the interfacial adhesion. And the second regime, where grafting takes place very slowly, provides an opportunity to make mixed layers by switching to another polymer solution.

References

(1) Advicula, R. C. B., W.; Caster, K.; Ruhe, J., Eds. *Polymer Brushes*; Wiley: New Jersey, 2004.

(2) Luzinov, I.; Minko, S.; Tsukruk, V. V. *Prog. Polym. Sci.* **2004**, *29*, 635.

(3) Wainwright, S. A.; Vosburgh, F.; Hebrank, J. H. *Science* **1978**, *202*, 747.

(4) Alberts, B. B., D.; Lewis, J.; Raff, M.; Roberts, K.; Watson, J. D. *Molecular Biology of Cell*; Garland Publishing, Inc., New York & London, 1994.

(5) Ridgway, S. H.; Carder, D. A. *IEEE Eng. Med. Biol. Mag.* **1993**, *12*, 83.

(6) Hergt, R.; Hiergeist, R.; Hilger, I.; Kaiser, W. A.; Lapatnikov, Y.; Margel, S.; Richter, U. *J. Magn. Magn. Mater.* **2004**, *270*, 345.

(7) Horton, J. M.; Bao, C. H.; Bai, Z. F.; Lodge, T. P.; Zhao, B. *Langmuir* **2011**, *27*, 13324.

(8) Wang, D. G.; Fan, J. B.; Siao, C. J.; Berno, A.; Young, P.; Sapolsky, R.; Ghandour, G.; Perkins, N.; Winchester, E.; Spencer, J.; Kruglyak, L.; Stein, L.; Hsie, L.; Topaloglou, T.; Hubbell, E.; Robinson, E.; Mittmann, M.; Morris, M. S.; Shen, N. P.; Kilburn, D.; Rioux, J.; Nusbaum, C.; Rozen, S.; Hudson, T. J.; Lipshutz, R.; Chee, M.; Lander, E. S. *Science* **1998**, *280*, 1077.

(9) Wang, D. N.; Liu, S. Y.; Trummer, B. J.; Deng, C.; Wang, A. L. *Nat. Biotechnol.* **2002**, *20*, 275.

(10) Huang, H.; Penn, L. S.; Quirk, R. P.; Cheong, T. H. *Macromolecules* **2004**, *37*, 5807.

(11) Morawetz, H. *Accounts Chem. Res.* **1970**, *3*, 354.

(12) Hasegawa, R.; Doi, M. *Macromolecules* **1997**, *30*, 5490.

(13) Ligoure, C.; Leibler, L. *Journal De Physique* **1990**, *51*, 1313.

(14) Kopf, A.; Baschnagel, J.; Wittmer, J.; Binder, K. *Macromolecules* **1996**, *29*, 1433.

(15) Smith, G. D.; Zhang, Y.; Yin, F.; Bedrov, D.; Dadmun, M. D.; Huang, Z. Y. *Langmuir* **2006**, *22*, 664.

(16) Mansfield, T. L.; Iyengar, D. R.; Beaucage, G.; McCarthy, T. J.; Stein, R. S.; Composto, R. J. *Macromolecules* **1995**, *28*, 492.

(17) Jones, R. A. L.; Norton, L. J.; Shull, K. R.; Kramer, E. J.; Felcher, G. P.; Karim, A.; Fetters, L. J. *Macromolecules* **1992**, *25*, 2359.

(18) Budkowski, A.; Steiner, U.; Klein, J.; Fetters, L. J. *Europhys. Lett.* **1992**, *20*, 499.

(19) Auroy, P.; Auvray, L.; Leger, L. *Phys. Rev. Lett.* **1991**, *66*, 719.

(20) Dhinojwala, A.; Granick, S. *Macromolecules* **1997**, *30*, 1079.

(21) Kumacheva, E.; Klein, J.; Pincus, P.; Fetters, L. J. *Macromolecules* **1993**, *26*, 6477.

(22) Cosgrove, T.; Phipps, J. S.; Richardson, R. M.; Hair, M. L.; Guzonas, D. A. *Macromolecules* **1993**, *26*, 4363.

(23) Budkowski, A.; Losch, A.; Klein, J. *Isr. J. Chem.* **1995**, *35*, 55.

(24) Ding, J. F.; Tao, J.; Guo, A.; Stewart, S.; Hu, N. X.; Birss, V. I.; Liu, G. J. *Macromolecules* **1996**, *29*, 5398.

(25) Dorgan, J. R.; Stamm, M.; Toprakcioglu, C.; Jerome, R.; Fetters, L. J. *Macromolecules* **1993**, *26*, 5321.

(26) Huguenard, C.; Varoqui, R.; Pefferkorn, E. *Macromolecules* **1991**, *24*, 2226.

(27) Motschmann, H.; Stamm, M.; Toprakcioglu, C. *Macromolecules* **1991**, *24*, 3681.

(28) Penn, L. S.; Hunter, T. F.; Lee, Y.; Quirk, R. P. *Macromolecules* **2000**, *33*, 1105.

(29) Huang, H.; Penn, L. S.; Quirk, R. P.; Cheong, T. H. *Macromolecules* **2004**, *37*, 516.

(30) Huang, H. Q.; Penn, L. S. *Macromolecules* **2005**, *38*, 4837.

(31) Huang, H. Q.; Rankin, S. E.; Penn, L. S.; Quirk, R. P.; Cheong, T. H. *Langmuir* **2004**, *20*, 5770.

(32) Penn, L. S.; Huang, H.; Sindkhedkar, M. D.; Rankin, S. E.; Chittenden, K.; Quirk, R. P.; Mathers, R. T.; Lee, Y. *Macromolecules* **2002**, *35*, 7054.

(33) Mirabella, F. M. J. *Practical Spectroscopy Series;Internal reflection spectroscopy: Theory and applications*; Marcel Dekker, Inc.: new york, 1993.

(34) Loring, J. S.; Land, D. P. *Appl. Opt.* **1998**, *37*, 3515.

(35) Krivopalov, V. P.; Shkurko, O. P. *Uspekhi Khimii* **2005**, *74*, 369.

(36) Zhang, S.; Koberstem, J. T. *Langmuir* **2012**, *28*, 486.

(37) Zhang, H. Q.; Van Der Linde, R. *J. Polym. Sci. Pol. Chem.* **2002**, *40*, 3549.

(38) Chernikova, E.; Morozov, A.; Leonova, E.; Garina, E.; Golubev, V.; Bui, C. O.; Charleux, B. *Macromolecules* **2004**, *37*, 6329.

(39) Hutchinson, R. A.; Beuermann, S.; Paquet, D. A.; McMinn, J. H. *Macromolecules* **1997**, *30*, 3490.

(40) Yi, Y.; Fan, X. H.; Wan, X. H.; Li, L.; Zhao, N.; Chen, X. F.; Xu, J.; Zhou, Q. F. *Macromolecules* **2004**, *37*, 7610.

(41) Quirk, R. P.; Mathers, R. T. *Polym. Bull.* **2001**, *45*, 471.

(42) Degennes, P. G. *Journal De Physique* **1976**, *37*, 1445.

(43) SJ., A. *J. Phys. (Paris)* **1977**, *38*, 977.

(44) Flory, P. J. *Statistical Mechanics of Chain Molecules*; John Wiley & Sons: New York, 1969.

(45) Brandrup, J. I., H. E.; Grulke, A. E.; Abe, A.; Bloch, R. D. *Polymer Handbook (4th Edition)*; John Wiley & Sons, 2005.

(46) Kent, M. S. *Macromol. Rapid Commun.* **2000**, *21*, 243.

(47) Adam, M.; Delsanti, M. *Macromolecules* **1977**, *10*, 1229.

(48) Mansky, P.; Liu, Y.; Huang, E.; Russell, T. P.; Hawker, C. J. *Science* **1997**, *275*, 1458.

(49) Prucker, O.; Naumann, C. A.; Ruhe, J.; Knoll, W.; Frank, C. W. *J. Am. Chem. Soc.* **1999**, *121*, 8766.

Chapter 6. Conclusions and Future Work

6.1 Conclusions

In this work different challenges were addressed to study the click reaction kinetics of functional compounds (small molecules and polymers) reacting to SAMs on the solid substrate. These high quality azide-functional substrates are prepared by a low temperature reaction of 11-bromoundecyltrichlorosilane with clean and activated Ge surfaces, followed by nucleophilic substitution of the terminal bromine by the addition of sodium azide. A new and universal analysis tool, ATR-IR, is developed to monitor kinetics of click reaction between alkyne end functional reactants and azide-functional substrates. For the small molecular (5-chloro-pentyne), time-resolved ATR-IR measurements indicate that the interfacial click reaction is initially first-order dependent on azide concentration as expected from the reaction mechanism, and then transitions to apparent second order dependence up to the saturation. The reaction achieves an ultimate conversion of 50% consistent with the limit expected due to steric hindrance of the 5-chloro-pentyne reactant at the surface.

Two approaches are developed to control the ‘click’ functionality on flat surfaces. Firstly, mixed monolayers comprising a fraction of the functional alkyne silanes and a fraction of chemically similar nonfunctional alkane silanes are used to manipulate the areal density of alkyne groups on the surface. Secondly, a new kinetic method is established to fabricate truly-mixed azide monolayers that have not been previously reported. The surface azide composition can be tailored by terminating the azide substitution reaction at a specific time.

The ATR-IR method is also used to directly monitor the kinetics between high-quality azide functional monolayers modified on Ge surface and alkyne end-functional poly (n-butyl acrylate) (PnBA) and polystyrene (PS), via a copper-catalyzed 1,3-dipolar cycloaddition reaction. Four-regimes of kinetic behavior was discovered: the first initial one (short time) is governed by the Brownian diffusion of the through the solvent and the reaction rate is very fast, this regime stops rather quickly when the grafting density of polymer layers is equal to σ^*; the second region slows down because of the increasing energy barrier when chains must penetrate a relatively dense brush layer; another two regimes before saturation occur with two characteristic transition points. A number of factors that influence the kinetics of polymer interfacial reaction are investigated including polymer nature and molecular weight. Some general phenomena are summarized to show consistent observation for different polymers with varied molecular weights.

6.2 Future Work

The ability of functional polymers to react to an interface is dependent on factors such as interfacial thermodynamics, solvent quality, polymer nature, polymer size, location of reactive functional groups and surface curvature. The practical importance of interfacial reactions and their complex fundamental behavior provides strong motivation for future research. Polymer nature and size has been discussed in this thesis. Other factors can be the subject of future investigations. The ATR-IR technique illustrated here can be developed and used for biosensor application. Using a similar procedure to modify the surface functionality of nanocomposites is also a subject of great interest. Further research may include work to monitor kinetics on nanoparticle surfaces using a similar technique FTIR equipped with a flow liquid cell.

The kinetics of polymer brush formation on hard substrates can be also studied in the melt state by applying a temperature dependent ATR-IR cell and replacing Germanium crystal with Zinc Selenide (ZnSe) crystal. ZnSe has a maximum useful temperature of 300 ℃, which is higher than that of Ge (125 ℃) and is suitable for studying polymer behavior at melt state.

Polymer brushes that form loops at the surface (i.e., telechelic polymers with both ends tethered to the surface) can provide improvements in properties such as adhesion and resistance to protein absorption. Hence the research of kinetics of such reaction should be continued.